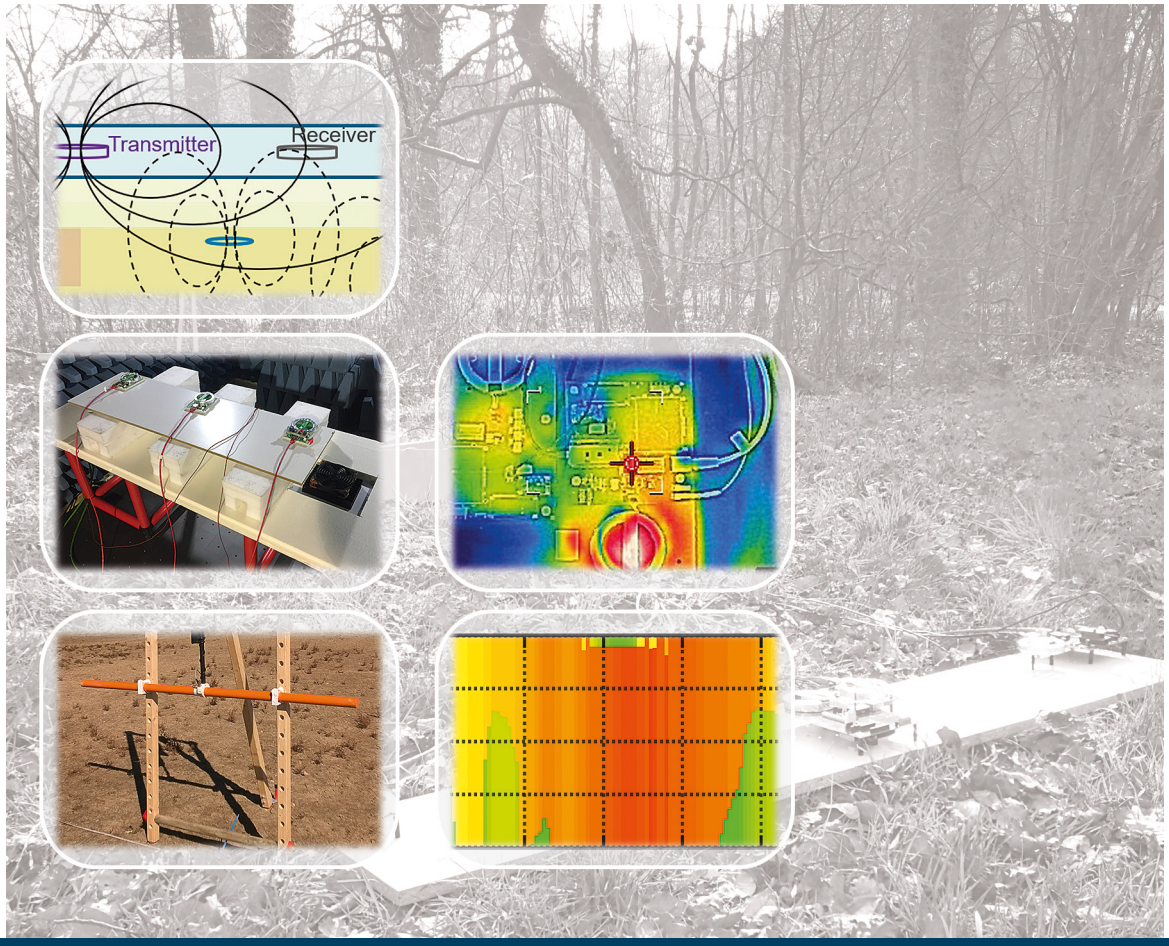

Development of Electromagnetic Induction Measurement and Inversion Methods for Soil Electrical Conductivity Investigations

Xihe Tan

Information
Band / Volume 62
ISBN 978-3-95806-490-4

Mitglied der Helmholtz-Gemeinschaft

JÜLICH
Forschungszentrum

Schriften des Forschungszentrums Jülich
Reihe Information / Information Band / Volume 62

Forschungszentrum Jülich GmbH
Zentralinstitut für Engineering, Elektronik und Analytik (ZEA)
Systeme der Elektronik (ZEA-2)

Development of Electromagnetic Induction Measurement and Inversion Methods for Soil Electrical Conductivity Investigations

Xihe Tan

Schriften des Forschungszentrums Jülich
Reihe Information / Information Band / Volume 62

ISSN 1866-1777 ISBN 978-3-95806-490-4

Bibliografische Information der Deutschen Nationalbibliothek.
Die Deutsche Nationalbibliothek verzeichnet diese Publikation in der
Deutschen Nationalbibliografie; detaillierte Bibliografische Daten
sind im Internet über http://dnb.d-nb.de abrufbar.

Herausgeber und Vertrieb:	Forschungszentrum Jülich GmbH Zentralbibliothek, Verlag 52425 Jülich Tel.: +49 2461 61-5368 Fax: +49 2461 61-6103 zb-publikation@fz-juelich.de www.fz-juelich.de/zb
Umschlaggestaltung:	Grafische Medien, Forschungszentrum Jülich GmbH
Druck:	Grafische Medien, Forschungszentrum Jülich GmbH
Copyright:	Forschungszentrum Jülich 2020

Schriften des Forschungszentrums Jülich
Reihe Information / Information, Band / Volume 62

D 82 (Diss. RWTH Aachen University, 2020)

ISSN 1866-1777
ISBN 978-3-95806-490-4

Vollständig frei verfügbar über das Publikationsportal des Forschungszentrums Jülich (JuSER)
unter www.fz-juelich.de/zb/openaccess.

This is an Open Access publication distributed under the terms of the Creative Commons Attribution License 4.0,
which permits unrestricted use, distribution, and reproduction in any medium, provided the original work is properly cited.

Abstract

Electromagnetic induction (EMI) is a promising contact-free technique for non-invasive near-surface geophysical investigations. Frequency-domain rigid-boom EMI systems with fixed distances between transmitter (Tx) and receivers (Rx) have been increasingly used for characterizing the upper meters (up to depths of approximately 1.5 times the maximum coil separation) of the subsurface. Such EMI systems enable the estimation of subsurface electrical conductivity distributions by inverting the apparent electrical conductivity (ECa) values measured from multiple different Tx-Rx configurations. However, calibration issues due to the thermal effects of the internal electronics as well as external electromagnetic influences hinder a reliable quantitative EMI data analysis.

For a custom-made EMI system, a transfer function analyzer (TFA) circuit is developed to monitor thermal drift effects of the electrical parameters of the receiver circuit. In addition, ambient temperature sensors (ATS) were included into the setup. Here, three correction methods were compared based on data from ATS, TFA, and a combination of both TFA and ATS. The presented work tested these three methods in three different experimental studies where the transmitter unit temperature is kept constant while the receiver unit is heated and cooled (1) manually, (2) by cloudy ambient conditions and (3) by partly sunny weather conditions. The results demonstrate that the TFA in the receiver circuit provides suitable data for correcting the phase drift originated within the receiver coil but not for correcting the drift caused by electrical components in the read-out circuit. The latter drifts need to be corrected using ATS data. Consequently, the combination of TFA and ATS data returned the best correction results achieving a worst-case accuracy of 2.3 mS/m compared to 10.2 mS/m (ATS-only) and 24.9 mS/m (TFA-only). The experimental results indicate that the drift of the transmitter unit is not negligible and needs to be corrected by a similar TFA circuit that should be investigated in future studies.

In addition to the thermal effects, the external electromagnetic influences also shift the measured ECa data which are caused by the presence of the operator, cables or metallic objects included in the field setup. The presented work introduces a novel multi-elevation

calibration and inversion (MECI) approach to correct for these external influences. Because the temperature drift correction for the transmitter has not been implemented in the custom-made EMI system, this MECI approach was performed using commercial systems. Instead of using soil sample data or additional non-EMI instruments to calibrate the ECa values, the MECI method uses the EMI data obtained from multiple elevations at a calibration location such that possible biases of other measurement methods are avoided. This MECI simultaneously solves for multiplicative and additive calibration parameters for each Tx-Rx configuration as well as estimates an inverted 1D soil model of the corresponding calibration position using the shuffled complex evolution (SCE) method. The MECI algorithm is validated by synthetic simulations with six elevations between zero and one meter returning multiplicative and additive correction factors that enable the calibration of the ECa data and the quantitative inversion of multi-layer soil models for a noise-free dataset. Adding 0.1 mS/m artificial noise to the ECa values, the calibration returns ECa values with a mean misfit of about 10% resulting in adequate inverted soil models for up to two layers.

The preliminary experimental verification for a hand-held EMI setup was performed on a test transect with electrical conductivities from about 5 to 30 mS/m. Erroneous soil models were obtained by inverting the uncalibrated transect data, whereas the MECI calibrated inversion results were confirmed by reference inversion results obtained from the electrical resistivity based measurement method. Similar calibration parameters for five independent calibration positions with low standard deviation (0.37 mS/m) were obtained indicating the stability of the MECI method. In addition to the hand-held EMI setup used in the preliminary verification, further MECI investigations for sled-based EMI setups designed for large-scale field measurements were tested. Different calibration factors were obtained in comparison with the hand-held EMI setup indicating that each measurement setup needs to be calibrated individually. In comparison with the electrical resistivity based reference results, calibrated ECa obtained from a homogeneous calibration location returned an average misfit below 2 mS/m for the sled-based EMI indicating a promising capability of MECI for practical large scale EMI applications.

Combining both results from the TFA-ATS temperature drift correction for our custom-made EMI system and the investigations of the MECI for commercial EMI instruments indicate the potential to build an improved custom-made EMI system that provides quantitative ECa values for soil conductivity inversion.

Zusammenfassung

Elektromagnetische Induktion (EMI) ist eine vielversprechende kontaktlose Messmethode für nicht-invasive geophysikalische Untersuchungen des Bodens. Zur Charakterisierung der oberen Meter des Untergrundes (bis zu Tiefen von etwa dem 1,5-fachen des maximalen Spulenabstandes) werden zunehmend starre EMI-Systeme mit zeitharmonischer Anregung und festen Abständen zwischen Sender (Tx) und Empfängern (Rx) verwendet. Solche EMI-Systeme ermöglichen die Abschätzung der Verteilung der elektrischen Leitfähigkeit unter der Oberfläche, indem die scheinbaren elektrischen Leitfähigkeitswerte (ECa), die mittels mehrerer verschiedener Tx-Rx Konfigurationen gemessen werden, invertiert werden. Kalibrierungsprobleme aufgrund von thermischen Effekten in der internen Elektronik sowie externe elektromagnetische Einflüsse behindern jedoch eine zuverlässige quantitative EMI-Datenanalyse.

Für ein selbst entwickeltes EMI-System wird ein „Transfer-Function-Analyser“ (TFA) entwickelt, der die thermischen Drifteffekte der elektrischen Parameter der Empfängerschaltung überwacht. Des weiteren wurden „Ambient-Temperature-Sensors“ (ATS) in das Setup einbezogen. In der vorliegenden Arbeit wurden drei Korrekturmethoden verglichen, die auf Daten von den ATS, des TFA und einer Kombiniation von TFA und ATS basieren. Diese drei Methoden wurden in drei verschiedenen experimentellen Studien getestet, bei denen die Temperatur des Senders konstant gehalten wird, während der Empfänger (1) durch manuelle Steuerung, (2) von bewölkten Umgebungsbedingungen, oder (3) von teilweise sonnigen Wetterbedingungen beheizt oder gekühlt wird. Die Ergebnisse zeigen, dass der TFA in der Empfängerschaltung geeignete Daten liefert, um die Phasendrift innerhalb der Empfängerspule zu korrigieren, nicht jedoch für die Korrektur der Drift, die durch elektrische Komponenten in der Ausleseschaltung verursacht wird. Letztere Drift muss mit ATS-Daten korrigiert werden. Die Kombination von TFA- und ATS-Daten hat somit die besten Korrekturergebnisse mit einer „Worst-Case“-Genauigkeit von 2,3 mS/m im Vergleich zu 10,2 mS/m (nur ATS) und 24,9 mS/m (nur TFA) ergeben. Die experimentellen Ergebnisse zeigen, dass die Drift der Sendeeinheit nicht vernachlässigbar ist, und durch eine ähnliche TFA-Schaltung

korrigiert werden muss, die in zukünftigen Studien untersucht werden sollte.

Neben den thermischen Effekten verfälschen externe elektromagnetische Einflüsse die gemessenen ECa-Werte, wie beispielsweise der Bediener, Kabel oder metallische Objekte innerhalb des Einflussbereichs des Messsystems. Daher führt die hier vorliegende Dissertation eine neuartige „Multi-elevation-Calibration and Inversion“ (MECI) ein, um diese externen Einflüsse zu korrigieren. Da die Driftkorrektur für den Sender nicht im selbst entwickelten EMI-System implementiert wurde, wurde diese MECI-Methode mit den kommerziellen Systeme getestet. Anstatt Bodenproben oder zusätzliche „Nicht-EMI“-Instrumente zur Kalibrierung der ECa-Werte zu verwenden, verwendet die MECI-Methode EMI-Daten, die an mehreren Messhöhen an einem Kalibrierungsort gewonnen werden, so dass mögliche Verfälschungen durch die Verwendung anderer Messmethoden vermieden werden. Die MECI bestimmt gleichzeitig multiplikative und additive Kalibrierungsparameter für jede Tx-Rx Konfiguration und ein 1D-Bodenmodell für den entsprechenden Kalibrierungsort mithilfe der „Shuffled Complex Evolution“-Methode. Der MECI Algorithmus wird durch Simulationen mit synthetischen, rauschfreien Datensätzen von sechs Messhöhen zwischen null und einem Meter validiert. Durch die Zugabe von 0,1 mS/m künstlichem Rauschen zu den ECa-Werte gibt die Kalibrierung eine mittlere Abweichung von etwa 10% zurück. Diese Kalibrierung ermöglicht die Inversion von Bodenmodellen mit bis zu zwei Schichten.

Die vorläufige experimentelle Verifizierung wurde mit einem tragbaren EMI-Setup auf einem Transsekt mit elektrischen Leitfähigkeiten von ca. 5 bis 30 mS/m durchgeführt. Ohne Kalibrierung konnten mit dem Setup keine realistischen Bodenmodelle aus den Transsekt-Daten gewonnen werden, während die MECI-kalibrierten Inversionsergebnisse durch Referenz-Ergebnisse bestätigt wurden, die aus der elektrischen Widerstandsmethode gewonnen wurden. Die Kalibrierungsparameter von fünf unabhängigen Kalibrierorten zeigen eine geringe Standardabweichung (0,37 mS/m), die die Stabilität der MECI-Methode anzeigt. Neben dem tragbaren EMI-Setup, das in der Verifikation verwendet wurde, wurden weitere MECI-Untersuchungen für ein Schlitten-Setup durchgeführt, das für großflächige Feldmessungen konzipiert ist. Die so gewonnenen Kalibrierungsfaktoren unterscheiden sich von denen des tragbaren EMI-Setup, was darauf hindeutet, dass jedes Messsystem einzeln kalibriert werden muss. Die kalibrierten ECa-Werte, die an einem homogenen Kalibrierort gewonnen wurden, zeigen für das Schlitten-EMI-Setup im Vergleich zu den Referenzergebnissen eine durchschnittliche Abweichung von unter 2 mS/m. Diese Ergebnisse deuten auf vielversprechende und kostengünstige Einsatzmöglichkeit der MECI für EMI-Kampagnen mit dem Ziel der Erfassung von quantitativen Leitfähigkeiten hin.

Die TFA-ATS-Temperaturdrift-Korrektur für das selbst entwickeltes EMI-System und die Ergebnisse der MECI für kommerzielle EMI-Instrumente zeigen das Potenzial, ein verbessertes EMI-System zu entwickeln, das quantitative ECa-Werte für die Inversion der Bodenleitfähigkeit liefert.

Publications

Parts of this doctoral thesis have been published, or will be used for future publications. The following list gives an overview of the written publications during my doctoral studies.

Tan, X., A. Mester, C. von Hebel, E. Zimmermann, H. Vereecken, S. van Waasen, and J. van der Kruk, 2019, Simultaneous calibration and inversion algorithm for multi-configuration electromagnetic induction data acquired at multiple elevations. *Geophysics* 84, pp. 1-14, doi: 10.1190/geo2018-0264.1.

Tan, X., A. Mester, E. Zimmermann, J. van der Kruk, W. Glaas, M. Dick, and M. Ramm, 2018, Induktive Messvorrichtung mit Kalibriereinrichtung und Verfahren, *German patent application*, DE 102018220532.9.

Tan, X., A. Mester, E. Zimmermann, and J. van der Kruk, 2015, Kalibrierungsverfahren für elektromagnetische Induktionsmesssysteme und Vorrichtung, *German patent application*, DE102016008841.9 / WO2018014891A1

van der Kruk, J., C. von Hebel, C. Brogi, M. S. Kaufmann, X. Tan, L. Weihermüller, J. A. Huisman, H. Vereecken, and A. Mester, 2018, Calibration, inversion, and applications of multiconfiguration electromagnetic induction for agricultural top- and subsoil characterization, *SEG Technical Program Expanded Abstracts*, pp. 2546-2550, doi: 10.1190/segam2018-2965257.1.

Tan, X., A. Mester, E. Zimmermann, H. Vereecken, S. van Waasen, and J. van der Kruk, Temperature drift correction for a rigid-boom electromagnetic induction geophysical instrument using an embedded transfer function analyzer circuit, *In preparation.*

Contents

1. Introduction[1]

1.1 Background

Near-surface is the outermost part of the earth's crust, and therefore plays a significant role in the entire biosphere (Butler, 2005). Among the near-surface, the vadose zone, also known as the unsaturated zone, extending from the land surface to the groundwater table (Holden and Fierer, 2005), has the closest interactions with human activities such as agriculture, mining, construction, and waste disposal (Nimmo, 2009). Consequently, it is important to understand the fundamental hydrological processes within the vadose zone.

As a key factor for investigating hydrological processes, the electrical conductivity which is closely related to the water content is often used to investigate the subsurface material characteristics such as soil texture, organic matter, soil moisture, salinity, and depth variability (Adamchuk et al., 2004) for a wide range of applications including geophysical exploration (Samouëlian et al., 2005; Robinson et al., 2008), environmental protection (Fitterman and Deszcz-Pan, 1998; Reynolds, 2011; Pellerin and Wannamaker, 2005), mineral exploration (Won et al., 2003), and agricultural management (Corwin and Lesch, 2005).

Various electrical and magnetic geophysical methods have been developed to measure the electrical conductivity, and can be mainly distributed into two categories which are contact-based and contact-free techniques, respectively (Vereecken et al., 2008). The contact-based category includes soil sampling (Manfreda and Rodríguez-Iturbe, 2006), time domain reflectometry (TDR, Robinson et al., 2003; Wraith et al., 2005; Weihermueller et al., 2013), electrical resistivity tomography (ERT, Samouëlian et al., 2005; Vanderborght et al., 2013),

[1] partly adapted from Tan et al. (2019).

and spectral induced polarization (SIP, Zimmermann et al., 2008a; Zimmermann et al., 2008b; Huisman et al., 2016) that show merit in precise measurements mostly used in point scales. However, these conventional electrode-based methods require galvanic coupling to the ground and are limited in measuring speed. Rolling electrode systems (e.g., Guillemoteau et al., 2017) are faster but cannot be used very well where the ground is frozen, very wet, or dried out completely.

The non-contact category is often referred to as electromagnetic (EM) techniques, which show great potential for continuous and non-invasive subsurface investigations for large-scale field mapping. EM systems include ground penetrating radar (GPR, Huisman et al., 2003; Weihermüller et al., 2007; Klotzsche et al., 2010; Klotzsche et al., 2013), microwave remote sensing (Wagner et al., 2007), and ground based and airborne EM (Metternicht and Zinck, 2003) using transient (TEM) as well as frequency domain (FDEM) techniques. (Robinson et al., 2008). The systems differ in the depth of investigation (DOI) from which they receive the majority of their response signals (Spies, 1989; Spies and Frischknecht, 1991). TEM is more suitable for depths greater than 10 m (Spies, 1989) due to the turn-off ramp of the transmitter (Schamper et al., 2014), whereas FDEM shows its merit in the characterization of the upper meters of the subsurface.

1.2 Electromagnetic Induction

Frequency-domain electromagnetic induction (EMI) rigid-boom systems (Frischknecht et al., 1991) carrying (multiple) coils in one portable unit with fixed coil separations and with frequencies between 1 and 50 kHz are increasingly used for high resolution as well as non-destructive investigations of the shallow subsurface including soil and plant interaction (Rudolph et al., 2015; Altdorff et al., 2016; von Hebel et al., 2018; Brogi et al., 2019), soil texture and salinity characterization (Triantafilis et al., 2000; Corwin and Lesch, 2003; Lesch et al., 2005; Abdu et al., 2008; Stockmann et al., 2017), clay and water content mapping (Reedy and Scanlon, 2003; Triantafilis and Lesch, 2005; Altdorff et al., 2017; Brogi et al., 2019), organic matter evaluation (Doolittle and Brevik, 2014), and time-lapse water depletion (Robinson et al., 2009). Due to the faster measurement speed and the support from GPS systems for georeferencing the data, areas up to 90 ha can be investigated (Triantafilis et al.,

2001; De Smedt et al., 2013; Vereecken et al., 2014; Rudolph et al., 2015; Brogi et al., 2019), and catchments up to 1000 ha can be measured (Frederiksen et al., 2017).

Using multi-configuration EMI systems that return apparent electrical conductivity (ECa) data obtained from different but overlapping subsurface volumes enables the estimation of the electrical conductivity changes with depth using inversion techniques (Santos et al., 2010; von Hebel et al., 2014). This has been achieved with a suitable choice of system configurations (von Hebel et al., 2014; Jadoon et al., 2015; Guillemoteau et al., 2016), using multiple instruments (Mester et al., 2011; Huang et al., 2017; von Hebel et al., 2018), or measurement elevations (Hendrickx et al., 2002; Sasaki et al., 2008; Triantafilis and Santos, 2010). The key factor for a reliable inversion is to obtain quantitative EMI data for multiple EMI configurations.

1.3 Quantitative EMI Data

Due to internal and external electromagnetic influences, quantitative ECa values, with deviations below 2 mS/m when measuring the subsurface with the electrical conductivity between 1 to 50 mS/m, are difficult to achieve. As a consequence, most EMI systems are used for qualitative analyses such as subsurface pattern imaging (Abdu et al., 2008) and time-lapse investigations (Lück et al., 2009).

For specific systems and especially for those with coil separations smaller than 2 m, significant errors of several to dozens of milli-siemens per meter have been observed when comparing with reference data obtained from soil samples (Moghadas et al., 2012), or electrical resistivity tomography (ERT) measurements (Lavoué et al., 2010; Mester et al., 2011; von Hebel et al., 2014). This is probably due to the fact that the magnitude of the electromagnetic response coming from the soil is smaller for small coil separations such that any disturbance has a relatively large influence. Two types of erroneous deviations are discussed in the following: temperature or time dependent drifts and constant shifts.

1.3.1 Temperature or Time Dependent Drifts

The first type of deviations is a temperature-dependent drift due to system warm-up effects, and ambient temperature changes (Robinson et al., 2004). This type of the drift shows to be unpredictable and variable over time during the measurements. To further investigate these drifts as well as their origins, Abdu et al. (2007) tested EMI instruments under changing temperature conditions. Instruments show deviations of up to 40% of the measured data. Performing the measurement on a cooler day or protecting the instrument from direct sunlight is recommended by Abdu et al. (2007) to minimize the temperature effects. Based on the self-developed EMI system, Mester et al. (2014) pointed out that the drifts mainly come from the thermal effects of the electrical elements. To correct these drifts, the responses and parameters of the circuit need to be monitored.

Robinson et al. (2004) demonstrated that differential heating of the EMI instrument, i.e., the temperature differences between the transmitter and receiver of the instrument, is one cause of the measurement drifts. This study recommended to shade the instrument, keep the operating temperature below forty degrees and perform a two-hour instrument warm-up to improve the measurement accuracy. Sudduth et al. (2001) investigated the accuracy issues of the EMI measurement data, and indicated that the ambient temperature has influenced the measurements. However, the results show that the measurement drift caused by the ambient temperature cannot be corrected because of the non-linear relationship between the drift and the changes of the ambient temperature.

1.3.2 Constant Shifts

The second type of deviations is systematic shifts in the measurement values that are due to external influences such as the presence of the operator (Nüsch et al., 2010), zero-leveling procedures (Sudduth et al., 2001), cables close to the system (Gebbers et al., 2009), and/or the field setup e.g., sled, GPS, etc. For the more recently available EMI systems, a factory calibration is performed, which is valid for factory-defined setups and settings. However, once the measurement setup is customized for different measurement purposes, this factory calibration is no longer sufficient to obtain quantitative ECa values.

As a consequence, several investigations have been carried out to calibrate EMI data and obtain quantitative ECa values. A conventional calibration approach established empirical relations between EMI data and "ground truth" values measured with the four-electrode probe (Corwin and Rhoades, 1982) or using undisturbed soil cores (Moghadas et al., 2012). For single-frequency single-separation EMI systems, Thiesson et al. (2014) introduced a calibration method that compares the instrument responses at multiple elevations with data from layered analytical models based on vertical electrical sounding (VES) measurements as well as a calibration method that is based on the response to non-magnetic spheres.

For multi-frequency single-separation EMI systems, a linear regression based calibration procedure was implemented using predicted EMI data from electrical resistivity tomography (ERT) measurements to calculate multiplicative and additive factors (Lavoué et al., 2010; Mester et al., 2011). Using this method, von Hebel et al. (2014) corrected data measured with a single-frequency multi-configuration EMI system and observed shifts of up to about 19 mS/m. Minsley et al. (2012) introduced a calibration method combining the approach of Lavoué et al. (2010) and an airborne calibration approach of Deszcz-Pan et al. (1998) to correct for systematic errors caused by incorrect instrument calibration or improper data leveling, together with filtering strategies for random errors, which are induced by cultural or instrumental EM noise. Hunkeler et al. (2015) obtained the calibration coefficient by implementing a bucking coil in the forward models of the platelet-free calibration sites with known sea-ice thickness. Minsley et al. (2014) determined calibration parameters together with an inverted subsurface model for an airborne EM system. This approach uses both in-phase and out-of-phase responses of the magnetic field for multiple frequencies and relatively similar coil separations of 7.9 and 9.0 m from measurements at multiple elevations between 10 and 60 m. The inversion uses fixed layer thicknesses as well as a regularization and weighting to constrain the subsurface models.

1.4 Objectives and Outline

The ultimate objective of this thesis is to obtain quantitative and stable EMI data by solving the following two questions:

1. What prevents the EMI system from producing temperature independent measurements, and how to correct the corresponding drifts?

2. Are EMI systems able to obtain quantitative measurement data without using additional instruments?

To monitor the thermal changes due to internal electrical components, chapter 2 introduces a temperature correction method for a custom-made EMI system developed by Mester et al. (2014). An build-in transfer function analyzer (TFA) circuit is implemented to measure the transient response of the main part of the circuit, whereas external ambient temperature sensors (ATS) are used to correct the temperature drifts of the read-out circuit. As a preliminary investigation, this study focuses on correcting for the receiver unit and keeping the transmitter unit under a stable temperature condition. The objective of this method is to reach the designed accuracy which is about 1 mS/m for the custom-made EMI system (Mester et al., 2014) when measuring the soil with the ECa from 5 to 40 mS/m. Because of the instability of the temperature, the proposed method monitors the phase response of the TFA in between the ECa measurements. The verification is performed using a temperature controlled setup as well as two case studies with realistic ambient temperature changes. Another two correction methods using either a temperature sensor or the TFA are compared with the proposed correction method.

The following chapter 3 introduces a multi-elevation calibration and inversion (MECI) method to improve the calibration approach in a fast and easy way and to obtain quantitative EMI data without using additional methods or pre-knowledge of the subsurface. To improve the efficiency by combining the calibration together with a quantitative layered inversion, the MECI method solves for calibration parameters, including multiplicative and additive factors for each coil configuration, and simultaneously returns an inverted 1D horizontally layered subsurface model. Because the temperature drift correction for the transmitter has not been implemented in the custom-made EMI system, this MECI method was performed using commercial rigid-boom single-frequency multi-coil EMI systems. The presented MECI method in chapter 3 uses a multi-configuration EMI system to acquire data at multiple elevations of up to 1 m on a single position, and only accounts for the out-of-phase responses of the magnetic fields.

To further investigate the MECI method toward an extended field application, chapter 4 presents MECI results for two EMI measurement setups with sleds and DGPS which are used for field-scale measurements. In addition, different electrode-based calibration approaches including vertical electrical sounding (VES) and electrical resistivity tomography (ERT) measurements are implemented as verification methods that are investigated and compared with the MECI approach.

Finally, chapter 5 presents the conclusions for the main results achieved in this thesis, as well as the review of major objectives and goals that have been accomplished. In addition, some possible directions for further improvements of EMI systems are discussed.

2. Temperature Drift Correction

In chapter 1, two critical issues of the EMI measurements have been introduced, one of which addresses that the ambient temperature causes drifts to the output data. To correct these drifts, the current chapter presents a correction method which is based on a transfer function analyzer (TFA) as well as ambient temperature sensors (ATS).

The chapter begins with analyzing the internal electronic components of the EMI circuit, arguing that the coil of the receiver is the major source of the drifts. Then the methodology of the TFA is introduced which monitors the transient phase response of the coil. In the next step, the corresponding temperature correction method is presented which includes the TFA and the ATS monitoring shifts from the coil and the read-out circuit, respectively. Experiments with manually controlled temperature setup are analyzed to verify the correction method. In addition, two case studies are discussed representing two realistic ambient conditions during the measurement.

2.1 Electromagnetic Induction System

A block circuit diagram of an EMI system with a single receiver unit is shown in figure 2.1. When the generator in the transmitter unit is providing an alternating signal with a fixed frequency (U_0^* with a constant peak amplitude and initial phase) to the transmitter (Tx) coil, an alternating current (I_{tx}^*) is generated with an initial phase φ_{tx} to U_0^* (figure 2.2) determined by the impedance parameter of Tx (presented as the transfer function G_{tx}^* in figure 2.1). Note that in figure 2.2, I_{tx}^* is used as the reference signal with a phase angle of zero. Under the free space condition, where no electrical conductive object is within the sensing

range of the system, the magnetic field at the location of the receiver (Rx) coil is presented as the primary magnetic field (H_p^*, figure 2.2), which is in-phase with I_tx^*. As a consequence, the induced voltage U_p^* is generated at the Rx coil. Because U_p^* cannot be measured in a realistic situation, the concept of the free-space transfer impedance is introduced, which is defined as

$$Z_0^* = \frac{U_\mathrm{p}^*}{I_\mathrm{tx}^*}. \tag{2.1}$$

According to the Maxwell equations (Ward et al., 1988), the phase of Z_0^* is equal to $\pi/2$ (figure 2.2).

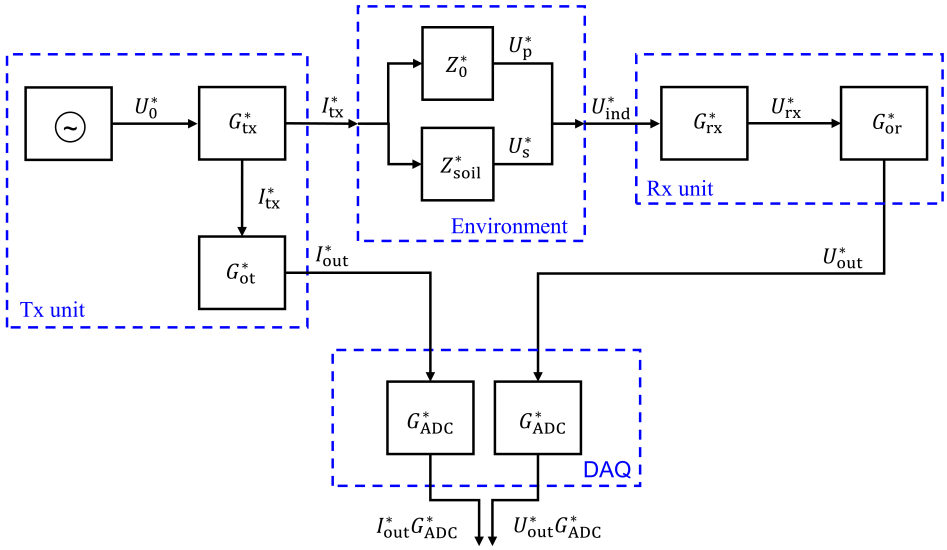

Figure 2.1: Block diagram showing a single transmitter-receiver EMI system. Each block represents the equivalent transfer function of the sub-circuit with input and output indicated. The output signals from both Tx and Rx units are acquired using a data acquisition system (DAQ) with two analogue-to-digital converters (ADC).

When the EMI system is measuring on top of a conducting subsurface, i.e., the soil presented as the equivalent impedance Z_soil^* in figure 2.1, eddy currents are induced in the subsurface with their amplitude depending on the transmitter current and the electrical conductivity σ of the subsurface. The magnetic field generated by the eddy currents at the location of the receiver is presented as the secondary magnetic field (H_s^*, figure 2.2). For small frequencies considered in the current study which are usually below 50 kHz ($\sigma/\omega\varepsilon \geq 1$,

ω is the angular frequency of I^*_{tx}, and ε is the electric permittivity), the displacement current in the soil is negligible. Similar to equation 2.1, a soil transfer impedance is defined as

$$Z^*_{soil} = \frac{U^*_s}{I^*_{tx}}, \tag{2.2}$$

where U^*_s (figure 2.1 and 2.2) represents the secondary induced voltage. As a consequence of the double induction effect, i.e., first into the subsurface and then into the Rx coil, the phase angle of Z^*_{soil} is approximately equal to π with respect to I^*_{tx}.

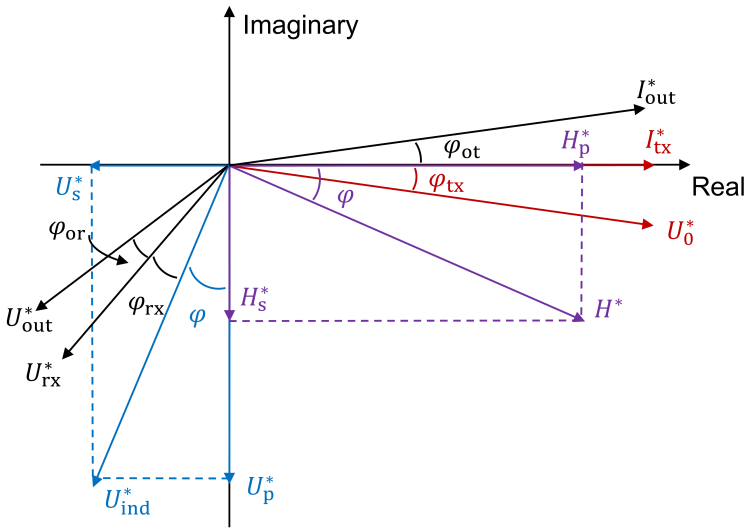

Figure 2.2: Phase diagram of the EMI system with the transmitter current (I^*_{tx}) as the reference signal. Phase angles plotted in black are arbitrary and depend on the specific circuit parameters.

The magnetic field (H^*, figure 2.2) detected by the receiver is the superposition of both, primary and secondary fields, and the induced voltage at the receiver coil equals

$$U^*_{ind} = U^*_p + U^*_s. \tag{2.3}$$

It is observed from the phase diagram (figure 2.2) that the phase difference between H^*_p and H^*_s is equal to $\pi/2$, and the same is valid for U^*_p and U^*_s. Therefore, the imaginary part of the secondary to primary fields/induced-voltage ratio can be presented as

$$\mathrm{Im}\left(\frac{H^*_s}{H^*_p}\right) = \mathrm{Im}\left(\frac{U^*_s}{U^*_p}\right) = \tan(\varphi) \approx \varphi. \tag{2.4}$$

Note that the approximation of equation 2.4 is based on the small-angle approximation which is usually the case when measuring the soil using the EMI system considered in the current study (with Tx-Rx separation smaller than 4 m, and the frequency within 50 kHz). By replacing U_{p}^{*} with the free-space transfer impedance Z_0^{*} according to equation 2.1, φ can be written as

$$\varphi = \arg\left(\frac{U_{\mathrm{ind}}^{*}}{U_{\mathrm{p}}^{*}}\right) = \arg\left(\frac{U_{\mathrm{ind}}^{*}}{I_{\mathrm{tx}}^{*} Z_0^{*}}\right). \tag{2.5}$$

With the known phase information of Z_0^{*}, which is $\pi/2$, the virtual parameter U_{p}^{*} is now replaced by an actual parameter I_{tx}^{*} which is possible to be measured.

The mathematical expression for the apparent electrical conductivity (ECa) used by McNeill (1980) describes a linear relationship between ECa and the imaginary part of the H_{s}^{*} to H_{p}^{*} ratio. This approximation was derived for the low induction number (LIN) conditions, and is written as (McNeill, 1980)

$$\mathrm{ECa} = \frac{4}{\mu_0 \omega s^2} \mathrm{Im}\left(\frac{H_{\mathrm{s}}^{*}}{H_{\mathrm{p}}^{*}}\right), \tag{2.6}$$

where μ_0 is the magnetic permeability of free space, and s is the Tx-Rx separation. Note that the LIN approximation is also within the small-angle approximation (equation 2.4). Based on equation 2.4 and 2.5, equation 2.6 can be written as

$$\mathrm{ECa} \approx \frac{4}{\mu_0 \omega s^2} \arg\left(\frac{U_{\mathrm{ind}}^{*}}{I_{\mathrm{tx}}^{*} Z_0^{*}}\right). \tag{2.7}$$

2.2 Circuit Design of the EMI System

In order to measure I_{tx}^{*}, which describes the current flowing through the equivalent inductor of the transmitter coil, the voltage drop is measured over a shunt resistor connected in series with the Tx coil using a differential voltage amplifier. By defining the shunt resistor and the differential voltage amplifier as a transfer function G_{ot}^{*} shown in figure 2.1, the output current I_{out}^{*} is presented as

$$I_{\mathrm{out}}^{*} = G_{\mathrm{ot}}^{*} I_{\mathrm{tx}}^{*}. \tag{2.8}$$

Note that I_{out}^{*} (as shown in figure 2.2) is the current through the Tx coil, and therefore has the phase difference φ_{ot} with respect to I_{tx}^{*}.

To obtain the phase information of U^*_{ind}, which describes the induced voltage of the equivalent inductor of the Rx coil, the voltage over the Rx coil is measured and presented as U^*_{rx} in figure 2.1. The term G^*_{rx} is defined as the transfer function of the Rx coil including the equivalent inductance, resistance, and capacitance of the Rx coil. Consequently, the relationship between U^*_{ind} and U^*_{rx} is presented as

$$U^*_{\mathrm{rx}} = G^*_{\mathrm{rx}} U^*_{\mathrm{ind}}. \tag{2.9}$$

The phase difference between U^*_{rx} and U^*_{ind} is presented as φ_{rx} (figure 2.2).

In order to analyze the phase drifts caused by the internal change of Tx and Rx coils, the circuit is simulated with SPICE. For each simulation, one of the parameters, i.e., the equivalent inductance, resistance, and capacitance of Tx and Rx coils, is increased by 1% where the others stay the same. Note that 1% is chosen based on a sensitivity analysis where small changes are approximated within a linear relationship. The phase differences of the transfer impedance (Z^*_{ind}) between each simulation and the reference model are given in percentage in table 2.1. Based on the design of the EMI system used in the current study (Mester et al., 2014), six operating frequencies are selected for the simulations, which are 5, 10, 15, 20, 25, 30 kHz, respectively.

The SPICE simulation indicates that the Rx coil is dominating the phase drifts. Among those drifts, the equivalent inductor is the major source, returning a maximum contribution of about 80% at a frequency of 5 kHz, whereas the second major source is the capacitor contributing from 5% at 5 kHz up to 29% at 30 kHz. Note that both Tx and Rx coils are based on the design by Mester et al. (2014). The resonance frequency of the Rx coil is about 38 kHz, which ensures a large sensitivity of the EMI system. However, small changes of the parameter in the Rx coil lead to large phase drifts that cannot be neglected.

Changes in the Tx coil result in a total contribution of less than 1% to the overall drift for all six frequencies (table 2.1). One reason is that the phase changes in I^*_{tx} are normalized when calculating the ECa value (equation 2.7). Another reason is that the resonance frequency of the Tx coil is about 2 MHz (Mester et al., 2014), which is far higher than the operating frequency such that a drift of the Tx coil results in very small phase changes. Therefore, the focus of this study is on monitoring the phase response from the Rx coil only.

Table 2.1: Phase drifts in percentage (%) caused by each component in Tx and Rx coils for six frequencies (5, 10, 15, 20, 25, and 30 kHz).

		5 kHz	10 kHz	15 kHz	20 kHz	25 kHz	30 kHz
Tx coil		< 1	< 1	< 1	< 1	< 1	< 1
Rx coil	R_{rx}	14.3	10.6	5.2	1.3	7.2	11.7
	L_{rx}	80.3	80.1	79.9	76.0	67.2	59.8
	C_{rx}	5.4	9.3	15.0	22.7	25.7	28.5

2.3 Transfer Function Analyzer (TFA)

The transfer function analyzer (TFA) circuit is designed to monitor the phase response of the receiver unit alternating with the ECa measurements when the transmitter signal is shortly switched off. Figure 2.3 shows the Rx unit (blue circuit) together with the TFA (green circuit), which mainly consists of a direct current (DC) source, and a control unit (a transistor and a microcontroller). When the gate-to-source voltage of the transistor is turned off by the microcontroller, the transistor reacts as an open circuit. As a consequence, the current of the DC source flows into the receiver circuit and charges the dynamic components, which is defined as the charging stage. After the steady state is reached, the gate-to-source voltage is turned on such that the transistor reacts as a short circuit, connecting the DC source to the ground, which is defined as the discharging stage. Consequently, the energy stored inside the Rx circuit is dissipated. Both the charging and discharging stages generate transient responses that are measured from the output terminal. Note that during the ECa measurement, the transistor connects the DC source to ground, such that its electronics have no influence on the Rx circuit. For the same reason, the transient signals of the discharging stage are used for the TFA analysis. In such a way, the characteristic of the TFA signal relates to the instantaneous parameters of the Rx circuit.

The TFA signal is a damped oscillating curve as shown in figure 2.4 that is characterized by an attenuation α and a damping frequency ω_d. This transient response signal is fitted with the following function

$$f_{TFA}(t) = Ae^{-\alpha t}\mathrm{Re}(e^{j(\omega_d t+\phi)}) + B, \tag{2.10}$$

where α and ω_d can be obtained together with the amplitude A, offset B, and initial phase ϕ.

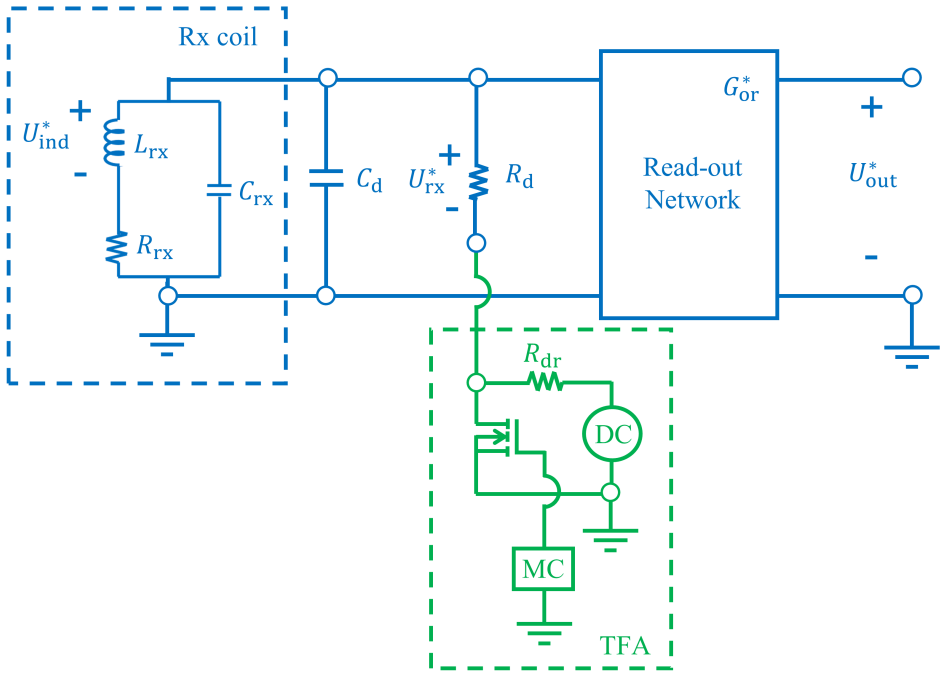

Figure 2.3: Equivalent circuit of the electromagnetic induction receiver. The green circuit extension is the transfer function analyzer circuit (TFA) implemented for the temperature correction.

Note that the values of A, B, and ϕ might change according to the selection of the starting time of the signal. The terms α and ω_d are needed for the investigation of the phase response, and are transferred to the complex frequency domain given by

$$G^*_{TFA}(j\omega) = \frac{j\omega + \alpha}{(j\omega + \alpha)^2 + \omega_d^2}. \tag{2.11}$$

The phase of G^*_{TFA} contains the information of φ_{rx} when ω equals to the transmitter frequency.

The parameters of the parallel resistor R_d, the parallel capacitor C_d, and the drain resistor R_{dr} (figure 2.3) were adjusted to maximize the decay time of the transient response curve, and to minimize the raising time of the transistor. Table 2.2 shows the circuit parameters of the receiver unit after including the TFA. Note that the resonance frequency of the Rx unit is changed to 19 kHz based on the updated parameters (table 2.2) instead of 38 kHz obtained from the original circuit (Mester et al., 2014) without implementing the TFA.

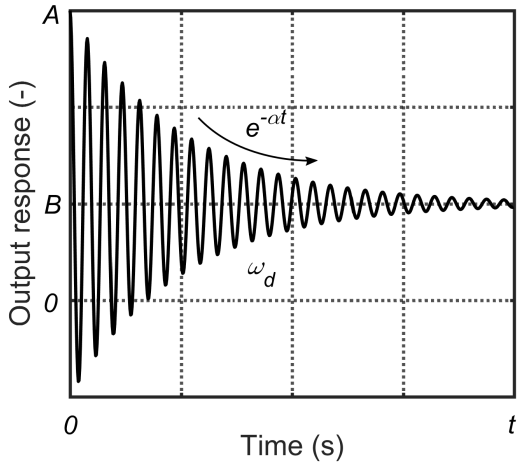

Figure 2.4: Example of a simulated transient response curve generated by the TFA circuit. The transient signal behaves as a damped oscillating curve with the damping attenuation (α), the damping frequency (ω_d), the amplitude (A), and the offset (B).

Table 2.2: Circuit parameters of the receiver unit shown in Figure 2.3.

Rx parameters	Value
Parallel resistance R_d	200 kΩ
Drain resistance R_dr	20 kΩ
Parallel capacitance C_d	1 nF
DC voltage (peak)	10 V
Resonance frequency	19 kHz

2.4 Temperature Drift Correction

Due to the small secondary-to-primary field ratio, the required dynamic range for the EMI system is in the order of 10^5 (Mester et al., 2014). Therefore, a high-resolution analog-to-digital converter (ADC) is implemented to measure the Tx and Rx signals. To optimize the input range of the ADC, the voltage of the Rx coil (U^*_{rx}) is amplified with a factor of 1 to 12 in a read-out circuit, which is presented as a transfer function G^*_{or} in figure 2.1. Recalling the mathematical expression of U^*_{rx} in equation 2.9, the output signals of the Rx unit can be written as

$$U^*_{\mathrm{out}} = G^*_{\mathrm{or}} G^*_{\mathrm{rx}} U^*_{\mathrm{ind}}. \tag{2.12}$$

The output signal measured from the system can be written as

$$\mathrm{ECa}^{\mathrm{out}} = \frac{4}{\mu_0 \omega s^2} \arg\left(\frac{U^*_{\mathrm{out}}}{I^*_{\mathrm{out}}}\right) \tag{2.13}$$

By substituting the term I^*_{out} with I^*_{tx}, and U^*_{out} with U^*_{ind} from equation 2.8 and 2.12, respectively, and according to equation 2.7, the relationship between ECa and $\mathrm{ECa}^{\mathrm{out}}$ becomes

$$\mathrm{ECa}^{\mathrm{out}} = \mathrm{ECa} + \frac{4}{\mu_0 \omega s^2} \arg\left(\frac{G^*_{\mathrm{or}} G^*_{\mathrm{rx}} Z^*_0}{G^*_{\mathrm{ot}}}\right) \tag{2.14}$$

Note that G^*_{tx} (figure 2.1) is not included because equation 2.8 use I^*_{tx} instead of U^*_0 as the base signal. By substituting the transfer function G^*_{or}, G^*_{rx}, and G^*_{ot} by their corresponding phase information, $\mathrm{ECa}^{\mathrm{out}}$ can be alternatively written as

$$\mathrm{ECa}^{\mathrm{out}} = \mathrm{ECa} + \frac{4}{\mu_0 \omega s^2} \left[\varphi_{\mathrm{or}} + \varphi_{\mathrm{rx}} + \frac{\pi}{2} - \varphi_{\mathrm{ot}}\right]. \tag{2.15}$$

Based on the circuit simulation in SPICE, the sum of all the phase information, i.e., the term $\left[\varphi_{\mathrm{or}} + \varphi_{\mathrm{rx}} + \frac{\pi}{2} - \varphi_{\mathrm{ot}}\right]$ in equation 2.15, returned an absolute value of about 1.56 rad when the system is operating at the frequency of 15 kHz. Note that this value is simulated at the room temperature of 23 °C, and will be changed when the ambient temperature changes. In addition, the data acquisition (DAQ) system (figure 2.1) contains two ADCs, which measure output signals from Tx and Rx units, respectively. This might cause additional drifts due to the transfer function of the ADC (G^*_{ADC}). Because the DAQ is an integrated system such

that all components are working under the same thermal condition, this effect is considered being compensated by dividing both output signals.

The TFA measures the phase response of all circuit components located before the first amplifier in the read-out circuit of the Rx unit, i.e., the term G^*_{rx}, and is used to correct the corresponding phase drifts. Drifts due to components such as amplifiers in both G^*_{ot} and G^*_{or} can be approximated using ambient temperature sensors (ATS) because the amplifiers are rapidly reacting to the ambient temperature. A test measurement showing the temperature drift effect from the amplifier is presented in appendix A. Therefore, a complete temperature correction is implemented containing a TFA circuit to monitor the phase changes of G^*_{rx}, together with two ATS to approximate the drift of the read-out circuits (G^*_{ot} and G^*_{or}) of Tx and Rx units.

2.5 Experimental Investigations

2.5.1 System Noise Measurement

The system configuration including the operating frequency as well as the Tx-Rx separation determines the signal to noise ratio (SNR) of the instrument and therefore needs to be optimized before the experimental investigations. According to the investigations performed by Mester (2015), the performance of the EMI system mainly depends on two factors that are (i) the dynamic range of the ADC for small Tx-Rx separations when the Rx unit is measuring a large primary magnetic field, (ii) the ambient electromagnetic noise when the system is measuring with large Tx-Rx separations. In order to evaluate the system noise level, the EMI system was tested with different configurations for eight frequencies (10.5, 15.5, 17.5, 18.5, 20.5, 21.5, 25.5, and 30.5 kHz) as well as five Tx-Rx separations from 0.4 m to 1.2 m with an increment of 0.2 m. Note that all system noise measurements as well as experimental verifications were performed outdoor at a fixed measurement location (with the soil having the ECa value of about 15 mS/m) in a minimum ambient noise environment. For each configuration, about fifty to one hundred continuously measured ECa values were obtained over about 2.5 to 5 minutes. The noise value of the corresponding system configuration was obtained by applying a polynomial fitting, after which the fitting curve was subtracted from the mea-

sured ECa values to remove the non-normally distributed effect caused by small temperature changes. Consequently, the standard deviation (STD) of the ECa value was obtained.

2.5.2 Measurement Timeline

The logic-clock timeline in figure 2.5 shows the complete procedure consisting of the TFA measurement trigger (figure 2.5a), Tx signal trigger (figure 2.5b), and the data acquisition trigger (figure 2.5c). To avoid the disturbance due to the transmitter signal during the TFA measurement, the generator in the Tx unit was switched off shortly before each TFA measurement and was switched back on afterwards for the next ECa measurement. Measurement controlling and signal processing were performed in MATLAB (Mathworks).

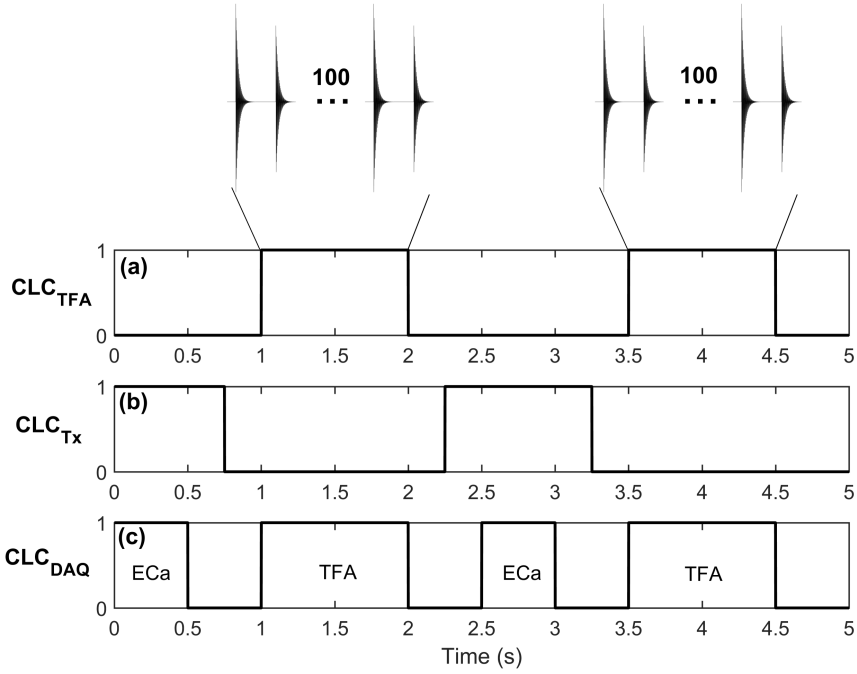

Figure 2.5: Logic-clock timeline shows (a) TFA measurement signal trigger, (b) the Tx signal trigger, and (c) the data acquisition trigger.

Electrical components usually experience warm-up effects when they are powered on, and then stay stable at the operating temperature, which differs for different components. Therefore, a system warm-up of 30 minutes was carried out before the experimental investi-

gations.

During one complete TFA measurement (figure 2.5a), one-hundred pairs of switch-on/off stages were triggered within 1 s such that the temperature changes during this short period are negligible. In order to find the curve fitting parameters in equation 2.10 for the TFA signals, the Levenberg-Marquardt algorithm for non-linear least-squares optimization was applied. Finally, the calculated values of one-hundred TFA phase responses were averaged to increase the signal-to-noise ratio.

Each ECa measurement (controlled by the Tx signal shown in figure 2.5b) lasted for 0.5 s and was recorded by the data acquisition system (figure 2.5c). With the ADC sampling frequency of 100 kHz, fifty-thousand measurement points were obtained. The measured data were processed using the lock-in technique, returning one complex value containing the phase information for each measurement period. A buffer time was applied, which took from 0.3 to 0.5 s, to ensure the data transmitting time and the independence between ECa and TFA measurements.

2.5.3 Experimental Verifications

The approach was firstly tested under controlled temperature conditions using the measurement setup shown in figure 2.6. The Tx and Rx units were separated into two thermal isolated boxes which were placed with a fixed distance. In such a way, the temperature for Tx and Rx were controlled and monitored individually. To avoid ground-loop effects, which may yield significant EM noise due to cables between Tx and Rx units, each unit is powered separately using DC voltage sources with output values from 5 to 12 V. The data from the microcontroller to the central USB hub is transmitted through an optical cable. The temperature of the Rx unit was manually changed using a plastic bottle filled with hot/cool water placed inside the thermally isolated box during the measurement. The measurement took about 20 minutes where a maximum temperature difference of 12 °C for the receiver unit was generated.

To only investigate the temperature drifts as well as the performance of the TFA circuit of the receiver, the thermal effect from the transmitter unit was minimized using a temperature

controlling system. This control system contains a fan that exchanges the air within the transmitter box using two rubber insulation tubes. It switches on/off the motor of the fan according to the pre-set temperature threshold based on a temperature sensor within the airflow. Because the manual temperature-controlling system works best when the surrounding environment has small temperature changes, the system was shaded and a measurement date with a relatively stable climate condition was chosen.

Three temperature drift correction methods for measured ECa values were analyzed, which are (i) the conventional method using the ambient temperature sensors presented as ATS method, (ii) a direct comparison of the phase responses between the TFA and ECa without any fitting (TFA method), and (iii) the combination of both methods (TFA-ATS method), respectively. The ambient temperature needs to be transferred into ECa values using an empirical equation. Note that the initial phase value for calculating the measured ECa is shifted by the initial value of φ_{rx}, φ_{or}, φ_{ot}, and $\frac{\pi}{2}$ in equation 2.15, which has the total absolute phase of about 1.56 rad as mentioned in section 2.4. As the focus of the current study is the relative ECa drifts due to the temperature, only the relative change ΔECa is

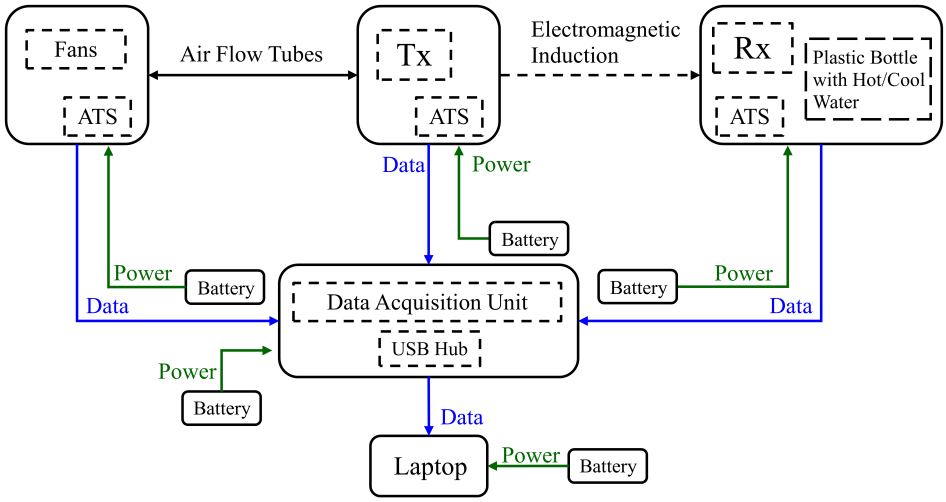

Figure 2.6: Diagram of the measurement verification setup. Tx and Rx units are placed separately in two thermal isolated boxes. A temperature controlling unit (upper left block) constantly exchanges the air with the Tx box (upper middle block) using two rubber insulation tubes. The temperature in the Rx box (upper right box) is varied by placing hot/frozen water bottles in the box. All data from the EMI system and the temperature sensors are acquired by the data acquisition unit (central block) and are transferred to a laptop.

Table 2.3: Mathematical expressions for the three methods.

Method	Data used	Mathematical expression
ATS	T_{Tx}, T_{Rx}	$\arg(\mathrm{ECa}^{\mathrm{pre}}) = \mathrm{offset} + b\Delta T_{\mathrm{Tx}} + c\Delta T_{\mathrm{Rx}}$
TFA	$\Delta\varphi_{\mathrm{TFA}}$	$\arg(\mathrm{ECa}^{\mathrm{pre}}) = \Delta\varphi_{\mathrm{TFA}}$
TFA-ATS	$\Delta\phi_{\mathrm{TFA}}$, T_{Tx}, T_{Rx}	$\arg(\mathrm{ECa}^{\mathrm{pre}}) = \mathrm{offset} + a\Delta\varphi_{\mathrm{TFA}} + b\Delta T_{\mathrm{Tx}} + c\Delta T_{\mathrm{Rx}}$

presented in the measurement results thereafter by subtracting the initial value.

To derive the parameters for the ATS and TFA-ATS methods, the multiple linear regression (MLR) algorithm was applied, similar to what has been shown in the literature to predict soil properties from EMI data (Lesch et al., 1995; Abdu et al., 2008; Altdorff et al., 2016). In this study, the stepwise MLR was used which finds the best model fits by adding/removing variables such that the least significant variables are excluded by setting the probability threshold (p-value) to 0.05 (Amezketa, 2006; Altdorff et al., 2018). The selected variables include the TFA phase response, and the ambient temperature of the Rx and Tx units (T_{Rx} and T_{Tx}, respectively). The standardized regression coefficient, also known as the beta weight (Bring, 1994), returned from the MLR was used to indicate the correlation between the ΔECa values and the drift data obtained from the TFA circuit as well as the ATS. The predicted ΔECa values obtained from the MLR approach were compared with the measured ΔECa results returning the root mean square error (RMSE) which indicates the general performance of the data fitting. Note that the ideal/reference result should return ΔECa values approaching zero. Table 2.3 summarizes the mathematical expressions for all the three correction methods.

2.5.4 Case Studies

In order to investigate the temperature drifts of the Rx unit under realistic conditions, two case studies were carried out under different weather conditions, which are cloudy and partly sunny, respectively. Each case study contains a long-term measurement that took approximately 3 hours. In contrast to the manually controlled experiments, no temperature controlling was applied for the Rx unit for both two case studies. Instead of maintaining the temperature of the Tx unit by switching on/off the ventilation, in this setup, a Peltier-element-based automatic heating/cooling system was used. As a consequence, the fan was

continuously running ensuring a constant airflow from a reservoir with a controlled temperature to the transmitter unit. However, such a system can only compensate slow temperature changes.

2.6 Results and Discussion

2.6.1 Optimization of the System Noise

From the system noise test results shown in figure 2.7, it is observed that the noise levels are decreasing with increasing Tx-Rx separations for all frequencies. For the smallest Tx-Rx separation of 0.4 m, the noise test result shows a significantly large ECa noise of up to 6 mS/m at 17.5 kHz. This large noise level is possibly due to the reduced secondary to primary magnetic field ratio, e.g. approximately 2.9×10^{-5} for 17.5 kHz and 1.6×10^{-5} for 10.5 kHz, which have the same amplitude order as the required dynamic range (Mester et al., 2014).

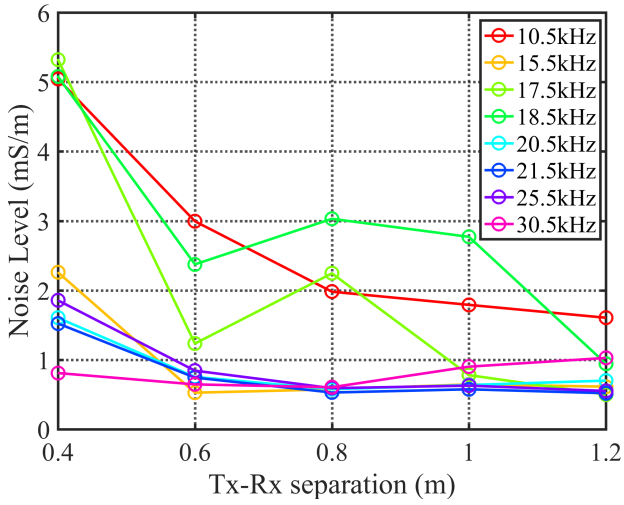

Figure 2.7: System noise processed into ECa values for different Tx-Rx separations. Each colored line is measured at a different transmitter frequency.

When comparing the accuracy results obtained from different operating frequencies, the smallest noise level of about 1 mS/m was returned for frequencies of 15.5, 20.5 21.5, 25.5, 30.5 kHz at a Tx-Rx separation of 0.8 m. Larger noise levels were obtained for frequencies of

10.5, 17.5 and 18.5 kHz for all separations, which is probably due to the ambient magnetic noise at the corresponding frequencies. In general, the measuring frequency can be changed flexibly depending on the ambient noise spectrum. In this study, the frequency of 15.5 kHz was selected as the operating frequency because it generally shows a low noise level in combination with the Tx-Rx separation of 0.8 m. This configuration was used for all of the following experimental investigations.

2.6.2 Initial Value for Calibration

When measuring at the experimental test location using the proposed EMI configuration (with the frequency of 15.5 kHz, and the Tx-Rx separation of 0.8 m), the initial phase returned the value of about 1.50 rad. By subtracting the term $[\varphi_{\mathrm{or}} + \varphi_{\mathrm{rx}} + \frac{\pi}{2} - \varphi_{\mathrm{ot}}]$ in equation 2.15 with the value of 1.56 rad (according to the simulation as discussed in section 2.4), the phase −0.06 rad was returned corresponding to the ECa value of about 3000 mS/m. Note that the minus sign indicates the direction between the U^*_{ind} and I^*_{tx}.

In addition to the electrical conductivity of the subsurface (with the ECa value of about 15 mS/m), this initial ECa value (of about 3000 mS/m) contains the electromagnetic response from the measurement setup (cables, metals, electronic devices, etc). A calibration is required to correct this shift, but it is not the focus of the current chapter. Consequently, the initial value was subtracted and only the drifts due to temperature changes were investigated in the following sections.

2.6.3 Temperature Controlled Measurement

The temperature controlled measurement is shown in figure 2.8. The temperature of the Tx unit was kept stable within 0.5 °C of variations (figure 2.8, pink line). However, the small changes of the Tx temperature are still visible in the measured ΔECa results (figure 2.8, black line) which indicates that the thermal effect of the Tx unit has an influence and cannot be neglected for the situation where no temperature stabilization is applied to the Tx unit.

When the temperature of the Rx unit (figure 2.8, blue line) was heated up from 26 to 37 °C in the first 12 minutes, the measured ΔECa followed the temperature but with a short

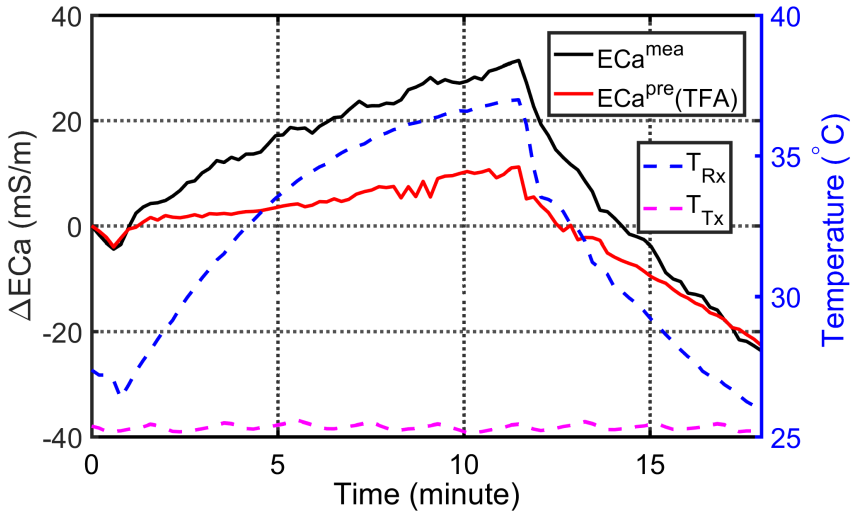

Figure 2.8: Measured ΔECa values (black solid line) together with the equivalent ΔECa values obtained from TFA (red solid line) for the left axis. The temperature values for the Tx (pink dash line) and Rx (blue dash line) are plotted for the right axis.

delay and increased to of about 30 mS/m. When the Rx unit was cooled down to the initial temperature, the ΔECa decreased to a negative value of about −22 mS/m. In general, the ECa drifts show a strong correlation with the Rx temperature indicating that these drifts need to be corrected for in order to obtain stable data. However, the ΔECa curve does not only follow the ambient temperature curve, which can be observed by the difference between the start and end values as shown in figure 2.8. This difference between the ΔECa and the ambient temperature curves indicates the complexity of the thermal drifts depending on both the instant ambient temperature and the thermal history of the EMI system, which is complex due to different thermal capacities for different electrical components. As a consequence, the thermal energy stored in each component results in different thermal decaying trends, and leads to a thermal legacy, which cannot be monitored by only measuring the instant ambient temperature.

In contrast, the equivalent ΔECa values obtained from the TFA measurement returned the same start and end values in comparison to the measured ΔECa indicating that the thermal legacy of the system can be monitored by the TFA measurement. It is also observed that increasing/decreasing trends of TFA are similar to the measured ΔECa curve, but

returned a different maximum value of about 10 mS/m instead of 30 mS/m during the heat-up period. This is probably due to the additional thermal effects from fast reacting components in the read-out circuit, which also need to be monitored and corrected.

2.6.4 Temperature Drift Correction

To analyze the temperature drifts of each component in more detail, the standardized regression coefficients (beta weight β) were obtained (table 2.4) from the MLR algorithm including all the explanatory variables. It is observed that T_{Tx} returned the smallest beta weight values indicating that the ambient temperature of the Tx unit has the smallest contribution to the ECa drifts. This result is expected because of the temperature stabilization of the Tx unit. Moreover, β of the TFA data resulted in a value of 0.56, which is larger in comparison to the T_{Rx} with the value of 0.48, indicating that the internal parameters of the Rx coil measured by the TFA influence the measured values more than the fast reacting components of the read-out circuit measured by the ATS.

Table 2.4: Standardized regression coefficient (beta weight) for TFA-ATS method when considering the variable φ_{TFA}, T_{Tx}, T_{Rx}.

$\beta(\varphi_{\mathrm{TFA}})$	$\beta(T_{\mathrm{Tx}})$	$\beta(T_{\mathrm{Rx}})$
0.56	0.02	0.48

To evaluate the performances of the three temperature correction methods, the predicted ΔECa values obtained from MLR are presented as a scatter plot against the measured ΔECa values (figure 2.9) and the fitting parameters are shown in table 2.5. The conventional temperature correction (ATS method) returns a RMSE value of 4.8 mS/m (figure 2.9a, and table 2.5, first row). Note that the variable T_{Tx} is excluded automatically from the MLR indicating that T_{Rx} is the only explanatory variable of the ATS correction method. This result indicates that the model is not well fitted when only temperature data is considered as an explanatory variable. The TFA correction method (table 2.5, second row), which only considers the TFA phase information, returns an even larger RMSE of 12.3 mS/m (figure 2.9b), such that the TFA method is less suited for the drift correction. Note that for the TFA correction method, the phase of the TFA measurement is directly subtracted from the measured phase of the ECa measurement without any fitting process (equation 2.15), whereas

Table 2.5: RMSE values and parameters of the mathematical expression (from table 2.3) for each temperature correction method.

Method	RMSE (mS/m)	Offset (mS/m)	a ($\Delta\varphi_{\mathrm{TFA}}$)	b (ΔT_{Tx})	c (ΔT_{Rx})
ATS	4.8	-8.7	-	-	4.0×10^{-3}
TFA	12.2	-	1	-	-
TFA-ATS	1.2	0.96	0.97	2.8×10^{-3}	2.0×10^{-3}

the ATS data need to be processed into ΔECa using an empirical equation including fitted parameters that are gathered during calibration measurements.

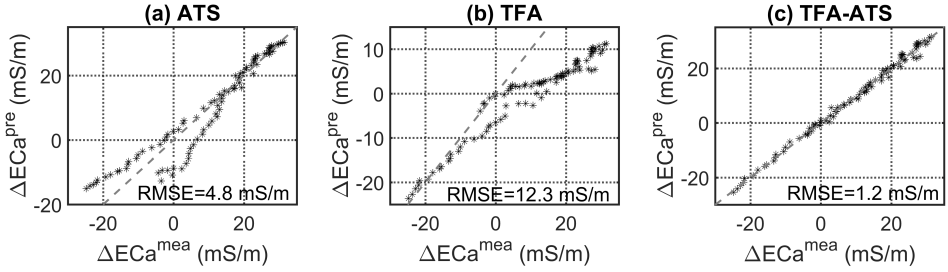

Figure 2.9: Scatter plot of the predicted versus measured ΔECa values for three temperature correction methods (a-c), including the 1:1 lines (dashed grey line) and the values of the root mean square error (RMSE).

Finally, the combined TFA-ATS method returns the RMSE value of 1.2 mS/m, which is the best result of all three introduced correction methods. When looking at the regression coefficient of $\Delta\varphi_{\mathrm{TFA}}$ (table 2.5, third row), it returned the value of 0.97 for the TFA component, which is close to 1. This result verifies the approach of calculating the phase response of the Rx circuit from the TFA measurement.

2.6.5 Case Studies

The measured results of two case studies are plotted in figure 2.10 showing two different weather situations. For the case study "cloudy", which was measured on a cloudy afternoon, T_{Rx} drops smoothly from 38 to 27 °C over 190 minutes with a small increasing peak between 40 and 60 minutes. At the same time, T_{Rx} drops gently from about 32 to 26 °C, and stays stable during the last 90 minutes. Consequently, the measured ΔECa followed the trends of T_{Rx} and T_{Tx} returning a deviation of about 80 mS/m. In contrast, case study "partly sunny" was taken on a partly sunny day with occasionally strong sunshine. It is observed that both T_{Tx}

and T_{Rx} change rapidly due to the direct sun exposure on the boxes, responding with multiple temperature changes between 23 and 32 °C. As a consequence, ΔECa values behave unstable showing similar trends as the ambient temperature and returning a maximum deviation of approximately 60 mS/m but with a short time delay compared to the corresponding peak in the ambient temperature. Similar to the observations from the manually temperature controlled measurement, the equivalent ΔECa values of the TFA phase response correlate with the measured ΔECa values.

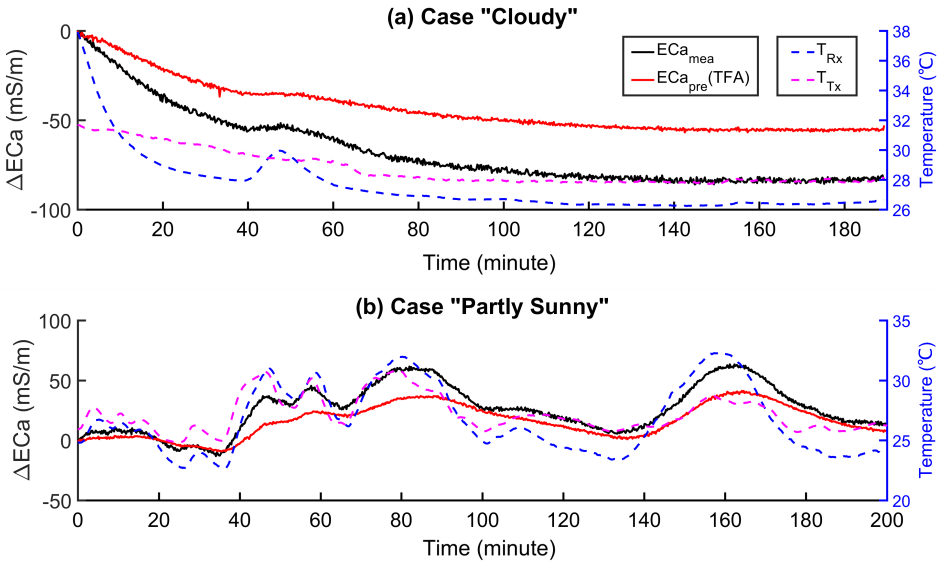

Figure 2.10: Two case studies measured for about 200 minutes with (a) smooth temperature changes (case "Cloudy"), and (b) rapid temperature changes (case "Partly Sunny").

It is observed that for case study "cloudy", the ATS correction method returned better temperature correction results with the RMSE of 2.6 mS/m (figure 2.11a) when comparing with the case "partly sunny" returning the RMSE of 10.2 mS/m (figure 2.11d). This is probably because when the temperature is changing gently the inner thermal changes of the coil and resistors also follow the ambient temperature such that the delay due to the heating/cooling of the copper is not significant.

In contrast, the large misfit for the case study "partly sunny" indicates the limitation of only using ATS to monitor the drifts for such environmental conditions, where the ambient temperature changes dramatically in a short time period resulting in different temperature

gradients for different electronics. Increasing the amount of temperature sensors and setting up a look-up table is a possible way to minimize the temperature drifts under this "partly sunny" environment. However, it requires a significant number of temperature sensors to observe the complete temperature distribution inside the EMI system and each electronic component.

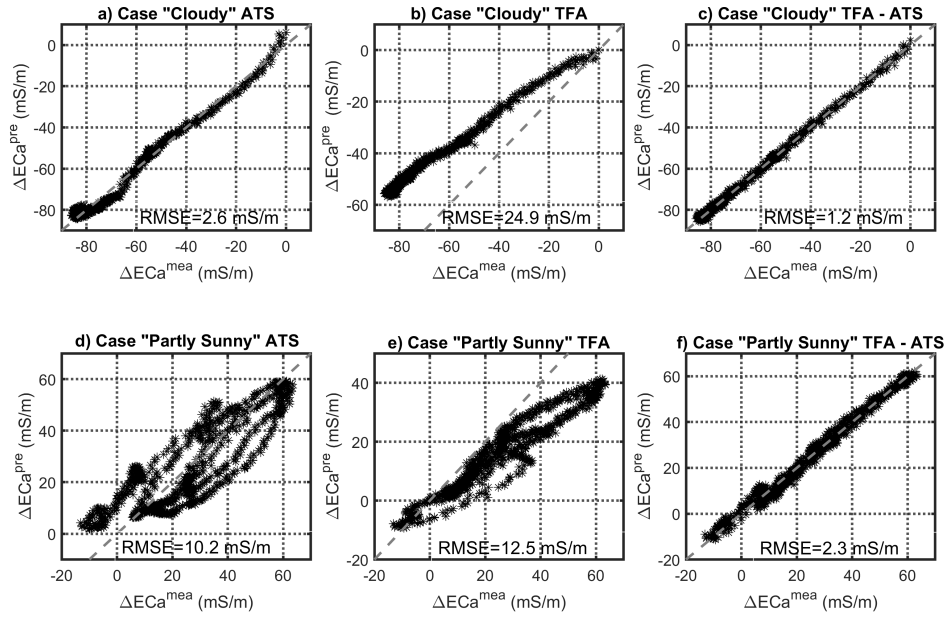

Figure 2.11: Scatter plot of the predicted versus measured ECa values with 1:1 lines (dashed grey line) of three temperature correction methods for case "cloudy" (a-c) and case "partly sunny" (d-f) with the corresponding value of the root mean square error (RMSE).

Large RMSE values for both two case studies were obtained from using the TFA method with values of 24.9 and 12.5 mS/m, respectively (figure 2.11b and 2.11e). A constant offset is observed especially for the results of the case "cloudy" (figure 2.11b) indicating the requirement of additional information for the correction.

The coefficient of $\Delta\varphi_{\mathrm{TFA}}$ in the TFA-ATS method was manually set to 1 for the two case studies, according to the results obtained from section 2.6.4 showing that this coefficient can be approximated to 1. The corresponding RMSE values of the TFA-ATS correction method for the two case studies are 1.2 and 2.3 mS/m, respectively (figure 2.11c and f). These results indicate that the temperature drifts for both of the two case studies can be corrected using

Table 2.6: Linear regression coefficients of the TFA-ATS method for three measurements

Measurements	$b(\Delta T_{\mathrm{Tx}})$	$c(\Delta T_{\mathrm{Rx}})$
Manually controlled	2.8×10^{-3}	2.0×10^{-3}
"Cloudy"	3.3×10^{-3}	1.5×10^{-3}
"Partly Sunny"	1.8×10^{-3}	1.7×10^{-3}

the TFA-ATS method while it shows a better performance for the "cloudy" case study where the temperature changes more gently.

In general, the TFA-ATS correction method returned the best results for all experimental investigations with a maximum RMSE value of 2.3 mS/m. The temperature information obtained from both TFA and ATS is necessary for correcting the temperature drifts. Note that neither the TFA method nor the ATS method resulted in a better correction for any of the presented investigations. However, the regression coefficients for T_{Tx} and T_{Rx} of the TFA-ATS method for all measurements (Table 2.6) are not constant. As a consequence, the ATS needs to be calibrated prior to each EMI survey by a measurement at a fixed position but at different temperatures. A possible reason is that the thermal effect of the Tx unit is not negligible, which is supported by the data shown in figure 2.8 and discussed above. Further investigations, e.g., adding a TFA to the Tx unit, are needed in order to predict the ATS regression coefficients.

An alternative way is to keep the complete EMI instrument at a constant temperature using an additional temperature cooling/heating system. However, such a method requires a significant amount of energy consumption, and is difficult to realize for applications in remote areas that require high mobility and lightweight systems.

2.7 Conclusions

Temperature changes in a custom-made EMI system influence the accuracy of the measured ECa values, which need to be corrected in order to quantitatively analyze the soil properties. Here, a novel TFA circuit and correction method were introduced that monitor the transient responses of the internal electrical components of an EMI sensor in order to compensate its thermal drifts.

Experimental investigations were carried out on the receiver unit of the custom-made EMI system. The measurements include a manually temperature controlled measurement as well as two case studies presenting two different but realistic measuring environments. ECa drifts of up to 80 mS/m were returned due to ambient temperature changes of up to 12 °C. Such drifts are significant with respect to the target system accuracy of about 1 mS/m, and indicate that a proper temperature correction is necessary.

When comparing three temperature correction methods, which are based on ATS, TFA, and the combination of both (TFA-ATS), respectively, results of the TFA-ATS method returned the smallest RMSE value of up to 2.3 mS/m indicating that both the ATS and the TFA data are necessary for the correction procedure. Different electrical components react with different delays and coefficients to the ambient temperature. The TFA is able to trace the initial thermal condition of the system and to monitor the electrical components before the read-out circuit. The ATS monitors the additional effects from the read-out circuit that reacts instantaneously to the ambient temperature and cannot be traced by the TFA method. At the moment, the ATS needs to be calibrated before each survey by an elaborate measurement. A possible reason is a drift effect from the transmitter that is clearly visible in the experimental results. Further investigations such as applying a TFA to the Tx unit are necessary in order to predict the ATS regression coefficients.

One feature of the proposed TFA-ATS method is that the thermal status of each sensor unit can be monitored individually, providing the potential to apply it to a multi-sensor EMI system. Furthermore, the TFA enables testing the circuit performance of each unit individually without using the electromagnetic excitations from the Tx unit. In addition, the Rx units can be used close to its resonance frequency where it has the largest sensitivity but also the largest phase drifts. With the TFA, those phase drifts can be fully compensated.

Experimental investigations indicate that the proposed temperature correction method is a promising tool to trace and correct the phase drifts due to the thermal changes of the internal electrical components under realistic EMI survey conditions.

3. Multi-elevation Calibration and Inversion Method (MECI)[1]

In the previous chapter, the temperature drifts, as well as the corresponding correction method were investigated. When moving on to the second issue described in chapter 1 which addressed the constant ECa shifts due to the external EM influences, a calibration approach for these constant shifts is necessary. This chapter presents a multi-elevation calibration and inversion (MECI) method which uses a EMI instrument and does not rely on any additional measurement equipment.

This chapter starts with describing the EMI methodology used in the forward modeling, and then investigates the sensitivity of the EMI system for different configurations and elevations. Next, the MECI method is introduced which calibrates the ECa data using a data set measured at multiple elevations. Finally, synthetic and experimental investigations are presented verifying that the MECI is a promising calibration method to obtain quantitative ECa data.

3.1 Electromagnetic Induction Forward Modeling

The frequency-domain EMI system used in the current study contains two Tx-Rx orientations including the horizontal coplanar (HCP) coil and the vertical coplanar (VCP) coil as shown in figure 3.1. The depth of investigation (DOI) is commonly defined as "the depths at which 70% of the cumulative response of the coil configuration is reached" (Saey et al., 2015).

[1] partly adapted from Tan et al. (2019).

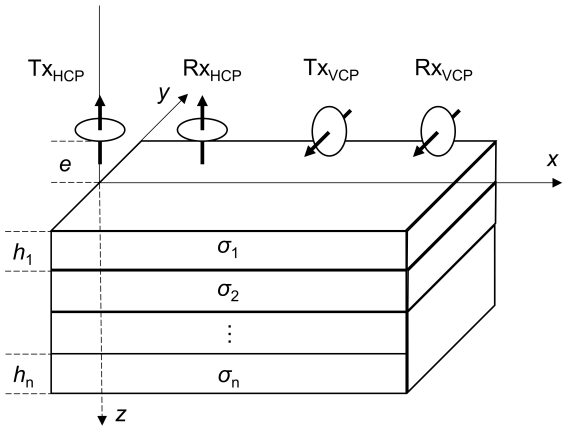

Figure 3.1: HCP and VCP configurations of the EMI system: a horizontal coplanar orientated transmitter-receiver pair (Tx_{HCP}-Rx_{HCP}) and a vertical coplanar orientated transmitter-receiver pair (Tx_{VCP}-Rx_{VCP}) placed at elevation e above a horizontally layered electrical conductivity ($\sigma_1, \cdots, \sigma_n$) model. The lowest zone is a homogeneous half-space.

This DOI is also referred to as depth of exploration (Saey et al., 2015), or effective depth of penetration (McNeill, 1980). Note that the corresponding depth range varies for different EMI configurations, such as different Tx-Rx orientations, Tx-Rx separations, and elevations of the system above the ground surface (Ward et al., 1988).

In this study, the presented electromagnetic forward model is based on Maxwell's equations in the frequency domain. When the distance between the transmitter and receiver is at least five times larger than the radius of the coil, the transmitter and receiver are considered as magnetic dipoles (Ward et al., 1988). Assuming a horizontally n-layered subsurface model with the z-axis pointing downward and HCP or VCP coils placed at an elevation e in the Cartesian coordinate system (figure 3.1), the axial component of the magnetic field along the magnetic dipole direction observed at the receiver position is given by Ward et al. (1988)

$$H^{*,\mathrm{HCP}} = \frac{M}{4\pi}\int_0^\infty [\exp(-u_0(z+e)) + r^*_{\mathrm{TE}}\exp(u_0(z-e))]\frac{\lambda^3}{u_0}J_0(\lambda l)d\lambda, \tag{3.1}$$

$$\begin{aligned} H^{*,\mathrm{VCP}} = &-\frac{M}{4\pi}\left(\frac{1}{l} - \frac{2x^2}{l^3}\right)\int_0^\infty [\exp(-\lambda(z+e)) - r^*_{\mathrm{TE}}\exp(\lambda(z-e))]\lambda J_1(\lambda l)d\lambda \\ &-\frac{M}{4\pi}\frac{x^2}{l^2}\int_0^\infty [\exp(-\lambda(z+e)) - r^*_{\mathrm{TE}}\exp(\lambda(z-e))]\lambda^2 J_0(\lambda l)d\lambda, \end{aligned} \tag{3.2}$$

where the superscripts HCP and VCP represent the horizontal and vertical coplanar configu-

rations respectively. M is the magnetic moment, J_0 and J_1 are the Bessel functions of zeroth and first order, λ is the Henkel transform integral parameter, $u_0 = \sqrt{\lambda^2 - k_0^2}$ with the wave number in free space (k_0), and l is the distance in the $x - y$ plane: $l = \sqrt{x^2 + y^2}$.
The reflection coefficient r_{TE} is given by

$$r^*_{\mathrm{TE}} = \frac{Y_0^* - \hat{Y_1^*}}{Y_0^* + \hat{Y_1^*}}, \tag{3.3}$$

where Y_0^* is the intrinsic admittance of free space and $\hat{Y_1^*}$ is the surface admittance of the first layer (Ward et al., 1988). The term $\hat{Y_1^*}$ can be calculated recursively by starting with the deepest layer where the surface admittance is equal to the intrinsic admittance, i.e., $\hat{Y_n^*} = Y_n^*$. For the i-th layer, the surface admittance is

$$\hat{Y_i^*} = Y_i^* \frac{\hat{Y}^*_{i+1} + Y_i^* \tanh(u_i h_i)}{Y_i^* + \hat{Y}^*_{i+1} \tanh(u_i h_i)}, \tag{3.4}$$

where $Y_i^* = \frac{u_i}{i\omega\mu_0}$, $u_i = \sqrt{\lambda^2 - k_i^2}$, h_i is the thickness of the i-th layer, $k_i = \sqrt{-i\mu_0\sigma_i\omega}$ is the wavenumber with the corresponding electrical conductivity of the i-th layer σ_i, and the magnetic permeability of free space μ_0.

When the system is placed in free space, the primary magnetic field (H_{p}^*) at the receiver position is calculated based on equations 3.1 to 3.4 with the assumption $r^*_{\mathrm{TE}} \to 0$. The secondary magnetic field (H_{s}^*) is given by

$$H_{\mathrm{s}}^{*,\mathrm{HCP,VCP}} = H^{*,\mathrm{HCP,VCP}} - H_{\mathrm{p}}^{*,\mathrm{HCP,VCP}}. \tag{3.5}$$

According to the concept of ECa described in chapter 2 (section 2.1), the mathematical expression of ECa (equation 2.6) can be alternatively written as

$$\mathrm{ECa} = \frac{4}{\mu_0\omega s^2} \mathrm{Im}\left(\frac{H_{\mathrm{s}}^{*,\mathrm{HCP,VCP}}}{H_{\mathrm{p}}^{*,\mathrm{HCP,VCP}}}\right). \tag{3.6}$$

3.2 Local Sensitivity for Different Tx-Rx Configurations and Elevations

Local sensitivity is defined as how much the ECa value changes when the σ value for a certain layer is changed. McNeill (1980) has derived the sensitivity curves for HCP and VCP configurations in which the coils are on the surface. Based on the Jacobian matrix calculation, the sensitivities are calculated for Tx-Rx coils being elevated in the air. A horizontally layered subsurface model with n thin layers $[\sigma_i, i = 1...n]$ is used, in which the upper n-1 layers have equal thicknesses, whereas the n-th layer is a homogeneous half-space. Starting with a homogeneous electrical conductivity of the subsurface, the sensitivity for the i-th layer is obtained by calculating the derivative of the ECa when the σ of the i-th layer is increased by $\Delta\sigma$, and is given by Raiche (1988)

$$\psi(\sigma_i) = \frac{\partial \mathrm{ECa}(\sigma_i)}{\partial \sigma_i} \approx \frac{\mathrm{ECa}(\sigma_i + \Delta\sigma) - \mathrm{ECa}(\sigma_i)}{\Delta\sigma}. \tag{3.7}$$

For multiple Tx-Rx configurations elevated at multiple elevations, the sensitivity matrix becomes an N-by-n matrix, where N is the total number of measurements, and is given by

$$\Psi = \begin{bmatrix} \frac{\partial \mathrm{ECa}^1(\sigma_1)}{\partial \sigma_1} & \cdots & \frac{\partial \mathrm{ECa}^N(\sigma_1)}{\partial \sigma_1} \\ \vdots & \ddots & \vdots \\ \frac{\partial \mathrm{ECa}^1(\sigma_n)}{\partial \sigma_n} & \cdots & \frac{\partial \mathrm{ECa}^N(\sigma_n)}{\partial \sigma_n}. \end{bmatrix} \tag{3.8}$$

The EMI system used in this study is a rigid-boom custom made CMD-MiniExplorer (GF Instruments, Czech Republic) instrument using a frequency of 25.17 kHz, and consisting of six different Tx-Rx separations that can be used in HCP or VCP orientations. Illustrations of the corresponding normalized sensitivity matrix (see equation 3.8) for Tx-Rx separations of 0.35, 0.50, 0.71, 0.97, 1.35, and 1.80 m (hereafter referred to as s35, s50, s71, s97, s135, and s180) for VCP $(c_1, \cdots, c_6)$ and HCP $(c_7, \cdots, c_{12})$ configurations are shown in figure 3.2 for six elevations $(e_1, \cdots, e_6)$: 0.0, 0.2, 0.4, 0.6, 0.8, and 1.0 m. For better visualization, each column, i.e., each Tx-Rx configuration at each elevation, is normalized by dividing the maximum value of that column. Note that this normalization is not applied during the inversion process (which will be introduced in section 3.3).

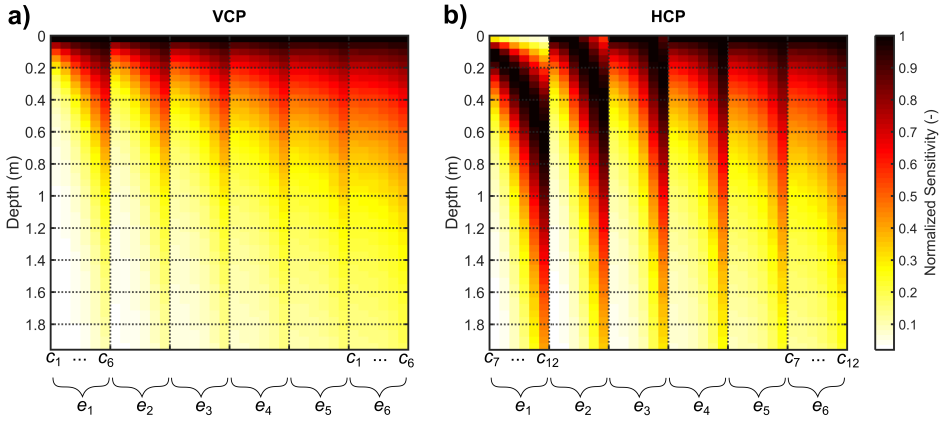

Figure 3.2: Normalized sensitivity as a function of coil configurations and elevations for (a) VCP orientations $(c_1, \cdots, c_6)$ and (b) HCP $(c_7, \cdots, c_{12})$ orientations. The six elevations $(e_1, \cdots, e_6)$ are 0.0, 0.2, 0.4, 0.6, 0.8, and 1.0 m, respectively. The sensitivity is normalized for each elevation and each Tx-Rx configuration.

Table 3.1: Normalization factors of the sensitivity shown in figure 3.2 for each configuration and elevation.

	Elevation	s35	s50	s71	s97	s135	s180
VCP	e_1	5	7	9	12	17	23
	e_2	20	18	18	20	24	29
	e_3	56	44	37	34	35	38
	e_4	114	86	66	56	51	51
	e_5	195	144	106	86	73	68
	e_6	299	218	157	123	100	89
HCP	e_1	11	16	23	31	43	58
	e_2	14	16	23	31	43	58
	e_3	31	27	27	32	43	58
	e_4	60	48	41	40	45	58
	e_5	101	77	60	53	53	60
	e_6	53	114	86	72	65	68

At zero elevation, $e_1 = 0$, the sensitivity curves equal the local sensitivity curves given by McNeill (1980) indicating that the VCP configuration senses the shallow part of the subsurface, whereas HCP has expertise in sensing to the deeper part of the subsurface. When increasing the elevation, the sensitivity for the deeper subsurface decreases, which was also indicated by increasing normalizing factors (table 3.1). Nevertheless, the larger coil separations have a higher sensitivity in the deeper subsurface compared with the smaller coil separations. It is clear that different elevations return different and complementary sensitivities that will

be exploited in the simultaneous calibration and inversion algorithm.

3.3 Simultaneous Calibration and Inversion Algorithm

In this section, a simultaneous calibration and inversion approach is introduced that obtains coil specific calibration factors and a 1D subsurface model at the chosen calibration position (CP) using multi-configuration EMI data of multiple elevations. This calibration and inversion approach presented as MECI assumes (i) that quantitative apparent electrical conductivity values can be obtained for each Tx-Rx configuration using a set of multiplicative and additive factors (Lavoué et al., 2010), (ii) that these factors are stable during the field measurements (von Hebel et al., 2014), and (iii) that the subsurface structure is horizontally layered. The latter is valid for many agricultural sites. The MECI approach estimates the multiplicative and additive calibration factors ($\mathbf{MF} = [\mathrm{MF}_1, \cdots, \mathrm{MF}_m], \mathbf{AF} = [\mathrm{AF}_1, \cdots, \mathrm{AF}_m]$) for m pairs of Tx-Rx configurations and an n-layered horizontal subsurface model defined by layer conductivities ($\sigma = [\sigma_1, \cdots, \sigma_n]$) and thicknesses ($\mathbf{h} = [h_1, \cdots, h_{n-1}]$).

Based on all the assumptions mentioned above, the modified apparent electrical conductivity ($\mathrm{ECa}^{\mathrm{mod}}$) is written as

$$\begin{bmatrix} \mathrm{ECa}^{\mathrm{mod},1} \\ \vdots \\ \mathrm{ECa}^{\mathrm{mod},m} \end{bmatrix} = \begin{bmatrix} \mathrm{MF}_1 & \cdots & 0 \\ \vdots & \ddots & \vdots \\ 0 & \cdots & MF_m \end{bmatrix} \begin{bmatrix} \mathrm{ECa}^{\mathrm{syn},1}(\sigma_1, \cdots, \sigma_n, h_1, \cdots, h_{n-1}) \\ \vdots \\ \mathrm{ECa}^{\mathrm{syn},m}(\sigma_1, \cdots, \sigma_n, h_1, \cdots, h_{n-1}) \end{bmatrix} + \begin{bmatrix} \mathrm{AF}_1 \\ \vdots \\ \mathrm{AF}_m \end{bmatrix}, \tag{3.9}$$

where $\mathrm{ECa}^{\mathrm{syn}}$ are the synthetic ECa values obtained by using the forward modeling equations 3.1 to 3.6. Finally, the matrix of unknown parameters can be written as

$$\mathbf{p} = \Big[\sigma_1, \cdots, \sigma_n, h_1, \cdots, h_{n-1}, \mathrm{MF}_1, \cdots, \mathrm{MF}_m, \mathrm{AF}_1, \cdots, \mathrm{AF}_m\Big], \tag{3.10}$$

with the total number of $u = 2n - 1 + 2m$ parameters. The inversion minimizes the misfit between measured and modified apparent electrical conductivity using an L2-norm objective function given by

$$\Delta \mathrm{ECa}(\mathbf{p}) = \frac{1}{N}\sqrt{\sum_{i=1}^{N}\frac{(\mathrm{ECa}^{\mathrm{mea}} - \mathrm{ECa}^{\mathrm{mod}}(\mathbf{p}))^2}{(\mathrm{ECa}^{\mathrm{mea}})^2}}, \tag{3.11}$$

where $\mathrm{ECa}^{\mathrm{mea}}$ is the measured ECa data, and N is the total number of measurements including different Tx-Rx configurations and elevations.

3.3.1 Shuffled Complex Evolution Method

Shuffled Complex Evolution (SCE) algorithm is used that combines probabilistic and deterministic approaches with evolutions between shuffled clusters of points, i.e., complexes, to search for the global minimum (Duan et al., 1993) of the objective function. The inversion procedure starts with building up a series of initial input parameters within the pre-defined searching space. For the SCE settings, five times the number of unknowns are used as the number of complexes ($5u$), with $2u + 1$ parameter sets in each complex, whereas further settings are set to the default values as described by Duan et al. (1994). This SCE algorithm has been successfully used for inverting EMI data (von Hebel et al., 2018), Moreover, it has also been applied to invert ground penetrating radar (GPR) data for resolving water content profiles (Mangel et al., 2017), to estimate the radius of subsurface object (Liu et al., 2018), and to obtain hydrologic parameters (Busch et al., 2013; Léger et al., 2014; Léger et al., 2016).

The L2-norm objective function is adapted from an L1-norm misfit function which is implemented by Mester et al. (2011) for a 1D, two-layer inversion based on a combined global-local search algorithm. Such an L1-norm function was later extended to a three-layered subsurface inversion with the SCE algorithm by von Hebel et al. (2014). For inverting a high-dimensional parameter space, the L2-norm has improved performance to reach the global minimum and is suitable for this calibration and inversion approach, whereas outliers can be better treated by the L1-norm algorithm due to electrical changes perpendicular to the measuring direction during large-scale field measurements. Note that no regularization or weighting is necessary for this inversion. When comparing the method presented in this study to the algorithm for airborne multi-frequency FDEM system calibration introduced by Minsley et al. (2014), the latter inverts for smooth subsurface models with multiple layers

having a fixed thickness up to several tens of meters in depth with weighting and regularizations. Moreover, the used airborne system uses different frequencies, larger coil separations, and elevations of up to 60 m, whereas the ground-based EMI system in this study uses one fixed frequency and has multiple coil separations that are far smaller than the skin depth. Note that the proposed method solves for a layered subsurface model whose electrical conductivity as well as layer thicknesses are unknown, which is a better assumption for agricultural subsurface where a plow layer is usually expected compared with a smoothed model.

3.3.2 Gauss-Newton Method

In addition to the SCE based inversion approach, another method using a Gauss-Newton algorithm was investigated. This method solves for the non-linear least-square problems with a second order Laplacian regularization matrix. By inverting the subsurface model with fixed thickness for each layer, which is different from the SCE method, as well as applying the regularization factors that restrict the electrical conductivity between each neighboring layer, this Gauss-Newton inversion algorithm returned smooth-layered model and is suitable for analyzing the subsurface which does not have clear boundaries between each layer.

However, only additive factors can be solved when using this method for the calibration and inversion process which might be limiting especially for calibrating the system whose multiplicative parameters have been indicated in the previous studies. Consequently, only the SCE method is applied for the experimental investigations in the following sections. Nevertheless the Gauss-Newton based algorithm is valuable to be further developed which shows merit in smoothed subsurface modeling. Detailed methodology as well as synthetic model analyses are presented in Appendix B as preliminary investigations.

3.4 Determination of the Minimum Number of Elevations

The linear-independence and non-uniqueness of the problem depend on the number of elevations and Tx-Rx configurations used in the EMI system. According to the Jacobian matrix definition, the sensitivity matrices of ECa^{mod} for different unknown parameters are written separately as

$$\mathbf{J}_\sigma = \begin{bmatrix} \frac{\partial \mathrm{ECa}^{\mathrm{mod},1}(\mathbf{p})}{\partial \sigma_1} & \cdots & \frac{\partial \mathrm{ECa}^{\mathrm{mod},1}(\mathbf{p})}{\partial \sigma_n} \\ \vdots & \ddots & \vdots \\ \frac{\partial \mathrm{ECa}^{\mathrm{mod},m}(\mathbf{p})}{\partial \sigma_1} & \cdots & \frac{\partial \mathrm{ECa}^{\mathrm{mod},m}(\mathbf{p})}{\partial \sigma_n} \end{bmatrix}, \tag{3.12}$$

$$\mathbf{J}_h = \begin{bmatrix} \frac{\partial \mathrm{ECa}^{\mathrm{mod},1}(\mathbf{p})}{\partial h_1} & \cdots & \frac{\partial \mathrm{ECa}^{\mathrm{mod},1}(\mathbf{p})}{\partial h_{n-1}} \\ \vdots & \ddots & \vdots \\ \frac{\partial \mathrm{ECa}^{\mathrm{mod},m}(\mathbf{p})}{\partial h_1} & \cdots & \frac{\partial \mathrm{ECa}^{\mathrm{mod},m}(\mathbf{p})}{\partial h_{n-1}} \end{bmatrix}, \tag{3.13}$$

$$\mathbf{J}_{\mathrm{MF}} = \begin{bmatrix} \frac{\partial \mathrm{ECa}^{\mathrm{mod},1}(\mathbf{p})}{\partial \mathrm{MF}_1} & \cdots & 0 \\ \vdots & \ddots & \vdots \\ 0 & \cdots & \frac{\partial \mathrm{ECa}^{\mathrm{mod},m}(\mathbf{p})}{\partial \mathrm{MF}_m} \end{bmatrix}, \tag{3.14}$$

and

$$\mathbf{J}_{\mathrm{AF}} = \begin{bmatrix} \frac{\partial \mathrm{ECa}^{\mathrm{mod},1}(\mathbf{p})}{\partial \mathrm{AF}_1} & \cdots & 0 \\ \vdots & \ddots & \vdots \\ 0 & \cdots & \frac{\partial \mathrm{ECa}^{\mathrm{mod},m}(\mathbf{p})}{\partial \mathrm{AF}_m} \end{bmatrix} = \begin{bmatrix} 1 & \cdots & 0 \\ \vdots & \ddots & \vdots \\ 0 & \vdots & 1 \end{bmatrix}. \tag{3.15}$$

Considering for a single elevation, the sensitivity matrix including all unknown parameters is given by

$$\mathbf{J} = \begin{bmatrix} \mathbf{J}_\sigma & \mathbf{J}_h & \mathbf{J}_{\mathrm{MF}} & \mathbf{J}_{\mathrm{AF}} \end{bmatrix}. \tag{3.16}$$

Accounting for all q elevations, the sensitivity matrix in equation 3.16 now becomes

$$\mathbf{J} = \begin{bmatrix} \mathbf{J}_\sigma^1 & \mathbf{J}_h^1 & \mathbf{J}_{\mathrm{MF}}^1 & \mathbf{J}_{\mathrm{AF}}^1 \\ \vdots & \vdots & \vdots & \vdots \\ \mathbf{J}_\sigma^q & \mathbf{J}_h^q & \mathbf{J}_{\mathrm{MF}}^q & \mathbf{J}_{\mathrm{AF}}^q \end{bmatrix}. \tag{3.17}$$

The criterion for determining the minimum number of elevations is that the total number of data sets needs to be equal to or greater than the number of unknowns (rows and columns of

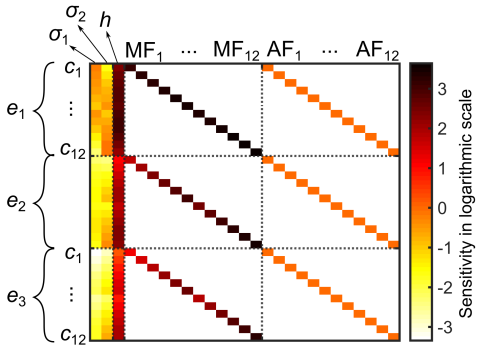

Figure 3.3: Illustration of the Jacobian matrix in equation 3.17 in logarithmic scale. Each column of the matrix represents an unknown parameter. Twenty-seven parameters including two electrical conductivity values, the thickness of the first soil layer, twelve multiplicative factors ($\mathrm{MF}_1, \cdots, \mathrm{MF}_{12}$) and twelve additive factors ($\mathrm{AF}_1, \cdots, \mathrm{AF}_{12}$) are included in this matrix for the case of three exemplary elevations (e_1, e_2, e_3) and twelve Tx-Rx configurations ($c_1, \cdots, c_{12}$) shown in rows.

the matrix in equation 3.17). Considering a situation with twenty-seven unknown parameters (u =27), i.e., two electrical conductivities ($n = 2$), one layer thickness, twelve multiplicative and twelve additive factors for the case with twelve Tx-Rx configurations ($m = 12$), the minimum elevation number of 3 can be determined by $q \geq u/m$. However, this is not a robust criterion because it does not hold if the data contain linearly-dependent information. Therefore, the rank of the sensitivity matrix is calculated in equation 3.17. The rank will be either equal to the number of unknowns when enough linear-independent measurements are performed, or it will be smaller when non-uniqueness exists.

To test the algorithm, the ranks using different synthetic subsurface models and calibration parameters are calculated. It is observed that the rank always returns the same number of unknowns when the required minimum number of elevations is used. In other words, the information provided by each Tx-Rx configuration or elevation is unique to the others which indicates the theoretical possibility to invert the subsurface structure by gathering information from multiple elevation measurements. Figure 3.3 shows the sensitivity matrix for equation 3.17 with the two-layer subsurface model and twelve Tx-Rx configurations for three elevations, similar to the visualization of Minsley et al. (2014). For experimental measurements, six elevations are used to stabilize the inversion and make it less dependent on the expected signal noise. To gather independent responses for each Tx-Rx configuration, subsequent elevations of 0.2 m with a maximum elevation of 1 m are chosen.

3.5 Synthetic Data Simulation

Synthetic models were built to verify the validity of the MECI approach. The data processing was implemented in MATLAB (The Mathworks Inc.) by extending the forward modeling from van der Kruk et al. (2000) for elevated EMI systems. A homogeneous half-space subsurface model with an electrical conductivity of σ=20 mS/m; a heterogeneous two-layered subsurface model with σ_1=20 mS/m, σ_2=40 mS/m, h=0.5 m; and a three-layered subsurface model with σ_1=10 mS/m, σ_2=20 mS/m, σ_3=50 mS/m, h_1=0.3 m, h_2=0.5 m are simulated based on the values obtained from previous investigations (von Hebel et al., 2014).

Multiplicative factors (MF^{syn}) and additive factors (AF^{syn}) (shown in table 3.2) were added artificially to the synthetic apparent electrical conductivities (ECa^{syn}). For all three synthetic model simulations, the EMI setup contained twelve Tx-Rx configurations (six Tx-Rx separations in HCP and VCP orientation) and ECa^{syn} values were modeled at six elevations. Note that the given subsurface models, calibration factors, and Tx-Rx configurations are based on previous surveys performed at the same test site (Lavoué et al., 2010; von Hebel et al., 2014) and represent realistic values for the following experimental measurements.

Table 3.2: Artificial calibration parameters used for the synthetic analysis for each Tx-Rx configuration. The values are based on measured data shown in Lavoué et al. (2010) and von Hebel et al. (2014)

	VCP		HCP	
Tx-Rx	MF^{syn} (-)	AF^{syn} (mS/m)	MF^{syn} (-)	AF^{syn} (mS/m)
s35	1.6	1	1.7	-1
s50	1.7	-2	1.6	-1
s71	1.7	-3	1.7	-2
s97	1.6	-3	1.4	1
s135	1.5	-2	1.1	3
s180	1.3	-1	0.9	4

3.5.1 Noise Free Model

The inversion using surface EMI data without simultaneous inverting for the calibration parameters returns erroneous electrical conductivity distributions (figure 3.4), which indicates the necessity of performing a calibration for quantitative subsurface electrical conductivity re-

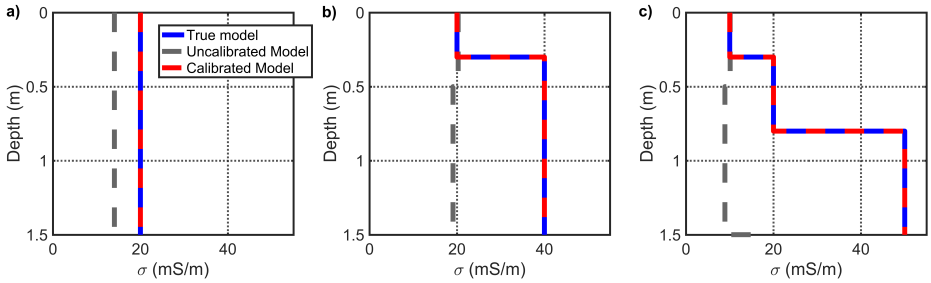

Figure 3.4: Inversion results for (a) homogeneous, (b) two-layer and (c) three-layer subsurface models (solid blue lines) for uncalibrated EMI data (dashed grey lines), and the MECI approach using surface and elevated EMI data (dashed red line).

constructions. The MECI approach using surface and elevated EMI data truly reconstructed the subsurface returning misfits (equation 3.11) below 10^{-13} for all three subsurface models (figure 3.4), which indicates the validity of using this approach to reconstruct homogeneous and multi-layer subsurface models.

3.5.2 Noisy Model

To investigate the performance under noisy conditions, random normally distributed noise with a magnitude of 0.1 mS/m (the specified resolution of the CMD-MiniExplorer used in this study) was applied to the ECa^{syn} values before adding artificial calibration parameters. figure 3.5 shows the inverted subsurface models from twenty independent simulations (grey dashed lines) together with their mean values (red solid lines) and the synthetic models (blue solid lines). The mean value of the three-layer model (figure 3.5c) is close to the synthetic subsurface model although the reconstruction of each simulation (grey dashed lines) covers a large range of variations especially for the third layer. This indicates that an increase for subsurface complexity increases the difficulty to reconstruct the true model. In other words, when increasing the number of unknowns, i.e., complexity of the search space, the similarity of each local minimum increases significantly during the inversion. Meanwhile, due to the reduced DOI when lifting the EMI system, the effect of noise when inverting the deeper layer is increased. It is expected that the three-layer model inversion together with calibration parameter estimation is possible by increasing the separation of Tx-Rx which compensates for the reduced sensitivity after lifting the instrument. For the given EMI system, it is concluded

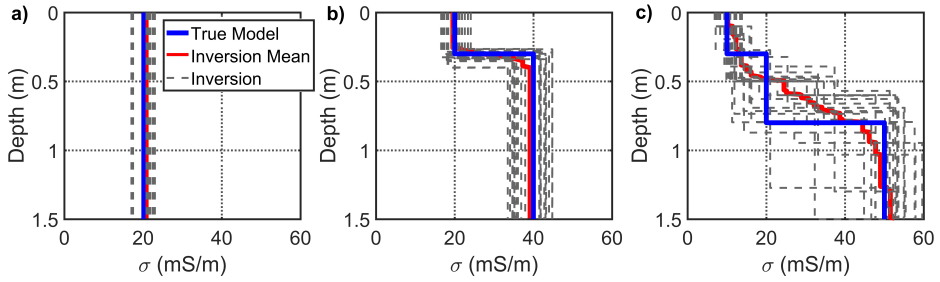

Figure 3.5: Inversion results for the subsurface models with 0.1 mS/m noise added to the apparent electrical conductivity values. The grey dashed lines show the inversion results of twenty simulations, and the red solid lines represent their mean values.

Table 3.3: Misfits between synthetic and inverted values when adding noise with a standard deviation of 0.1 mS/m to ECa. Results are calculated as the mean values over all coil configurations and twenty simulations. Normalized misfits of ECa between ECa^{syn} and ECa^{inv} only account for the ground level but for all coil configurations.

Misfit	One-layer	Two-layer	Three-layer
ΔMF (absolute value) (-)	0.158 ± 0.030	0.165 ± 0.034	0.159 ± 0.033
ΔAF (absolute value) (mS/m)	0.172 ± 0.045	0.249 ± 0.070	0.438 ± 0.110
ΔECa (%)	10.45±0.14	10.03±0.43	10.30 ± 0.72

that the calibration and simultaneous inversion is possible for a two-layer subsurface.

The calibration parameters for the noisy conditions and the three synthetic models are analyzed by calculating the mean value and its standard deviations of the misfits over all Tx-Rx configurations (table 3.3). The MF factor shows stable results with misfits around 0.16 while the biases for the additive calibration factor increase when the layer number increases. To check the performance of the calibration, the normalized misfits between ECa^{syn} and ECa^{inv} were calculated only for the ground level but for all Tx-Rx configurations (table 3.3, ΔECa). The average relative error for the obtained multiplicative and additive calibration values is around 10% for all three synthetic models, which is reasonable for the considered noise level.

3.6 Experimental Data Verification

Experimental measurements were carried out on a bare-soil test field in Selhausen (North Rhine-Westphalia, Germany) where the soil consists of silt (70%), sand (13%) and clay (17%) (Weihermüller et al., 2007; Busch et al., 2014; von Hebel et al., 2014). On this test site, a 30 m long transect was selected that contains variations of electrical conductivity values between 5 and 30 mS/m. Such soil is often observed in agricultural fields. Similar to the findings of von Hebel et al. (2014), it is expected that the presented calibration approach turns the measured ECa values of the entire field into quantitative large-scale EMI data.

The experimental data acquired along the line consists of three types of measurements: (i) EMI measurements on the ground surface along the transect line, (ii) multi-elevation EMI measurements above the ground at selected calibration positions (CP), and (iii) vertical electrical sounding (VES) measurements at the selected calibration positions. In order to validate the calibration results, a VES based calibration was carried out for the same on-ground transect data. A detailed flowchart that illustrates each step of the verification is shown in figure 3.6.

3.6.1 EMI Data Acquisition and Processing

Along the transect, thirty-one discrete EMI measurements with twelve Tx-Rx configurations at a frequency of 25.17 kHz were carried out on the ground surface with a spatial sampling of 1 m. The EMI system measured ECa values with a sampling rate of 5 Hz for 40 s at each position, where the averaged measured ECa value (ECa^{mea}) was used. Five equidistant CPs were selected along the transect line that represent different electrical conductivity properties of the subsurface.

At each CP, EMI measurements (ECa^{ele}) at six elevations were carried out between 0 and 1.0 m above the ground with an increment of 0.2 m using a wooden rack (figure 3.7). A wireless controller unit was attached to the main body of the EMI instrument using a plastic crutch. The MECI approach was used to obtain the calibration factors as well as a single position subsurface model. Using the obtained calibration factors, the EMI data measured on the ground surface along the transect line (ECa^{mea}) were calibrated (presented as ECa^{MECI})

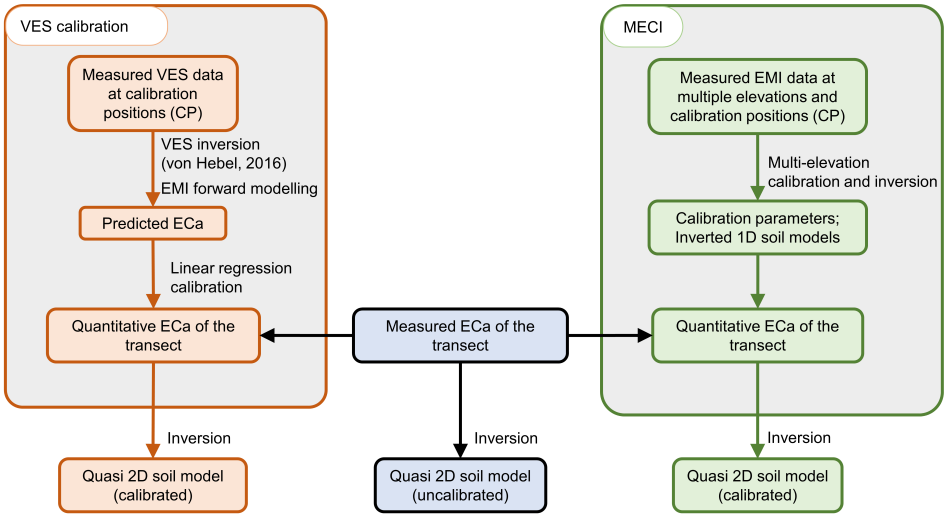

Figure 3.6: Flowchart of the experimental verification which shows the procedure of the MECI approach for the transect line (right panel), as well as a VES based calibration for comparison (left panel). Three individually inverted subsurface models are obtained using uncalibrated data and calibrated data using the VES based linear-regression calibration, and using the MECI approach.

and inverted to reconstruct the electrical conductivity distribution of the subsurface.

Figure 3.7: The measurement setup. A customized six coil CMD-MiniExplorer (GF Instruments, Czech Republic) is used with its Bluetooth handheld fixed to the crutch handle during measurements. The elevation was changed in steps of 0.2 m.

3.6.2 Vertical Electrical Sounding (VES)

The vertical electrical sounding (VES) method uses four electrodes including two current electrodes for feeding currents into the soil, and two potential electrodes for measuring voltage potentials. A different DOI can be obtained by changing the distance between the electrodes. To carry out the VES calibration similarly to Lavoué et al. (2010), and thereby estimate the linear-regression calibration factors, multiple locations need to be measured. Here, the five selected CPs were also used for the MECI approach. In order to record resistivity data, the Schlumberger configuration was used with fourteen electrode arrays with separations of the current electrodes from 1 to 10 m, and from 0.5 to 1.5 m for the potential electrodes at each CP.

A 1D subsurface model was obtained at each VES measurement position based on a multi-layer inversion algorithm implemented by von Hebel (2016). For the next step, predicted ECa values (ECa^{pre}) were modeled using the Tx-Rx configuration and frequency of the EMI system and the VES based subsurface model (see equations 3.1, 3.2, and 3.6). Linear regression between measured and predicted ECa (Lavoué et al., 2010) was applied for finding VES based calibration factors. Finally, the VES based calibrated EMI transect data (ECa^{VES}) were inverted based on the VES based calibrated EMI data to enable an independent comparison with the subsurface model obtained from the MECI approach.

3.7 Results and Discussion

The on-ground EMI data measured along the transect line (ECa^{mea}) are shown in figure 3.8. The ECa values from Tx-Rx configurations with small DOI (VCP s35, and VCP s50) returned values about 15 mS/m, whereas ECa values of the largest DOI (s180) increased to about 25 mS/m in the first part of the transect (0 to 15 m), which indicates a layered subsurface that is relatively resistive at shallow depths and more conductive in the deeper depths. The measured data of all Tx-Rx configurations returned dipping trends between 15 and 20 m. At the remaining part of the transect (20 to 30 m), the different Tx-Rx configurations measured small differences with a maximum ECa variation of about 5 mS/m, which indicates a relatively homogeneous subsurface.

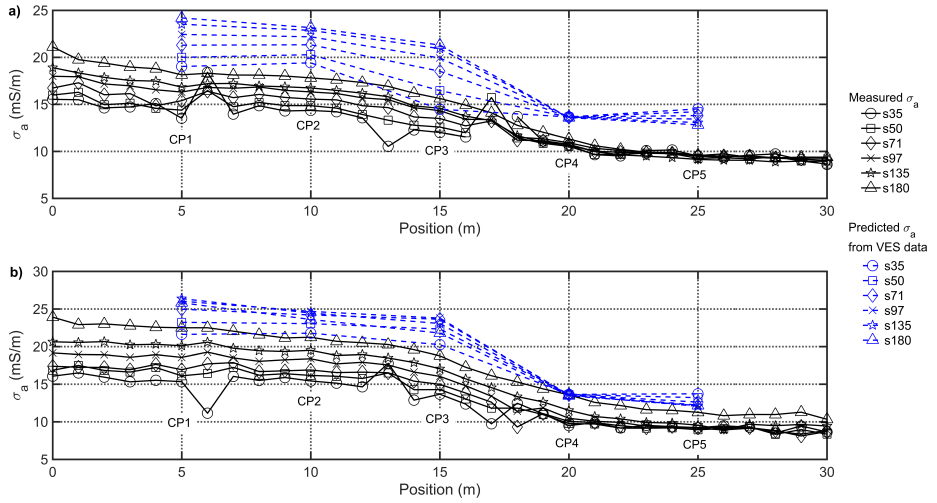

Figure 3.8: Measurements along the 30 m long transect line on a bare-soil test field in Selhausen (North Rhine-Westphalia, Germany) for (a) VCP and (b) HCP configurations. Solid black lines with markers show ECa values (ECa^{mea}) obtained from each coil separation. The corresponding dashed blue lines with markers are the predicted ECa values (ECa^{pre}) obtained from inverted VES data at five selected calibration positions (CP1 to CP5) at 5, 10, 15, 20, and 25 m, respectively. Note that the predicted ECa values are used for the VES calibration.

Using inverted VES data to predict ECa data (figure 3.8, blue markers), ECa^{pre} were obtained that differ from the measured ECa data by up to 10 mS/m, which clearly point out the necessity for calibration.

3.7.1 EMI Data Calibration

The multi-elevation EMI data (ECa^{ele})presented in figure 3.9 were measured at five CPs. For all Tx-Rx configurations, the ECa values decrease when the elevation increases. This is due to the influence of the air layer (0 mS/m) and the reducing sensing depth into the subsurface. The ECa values measured by Tx-Rx configurations with small DOI decrease faster than those from Tx-Rx configurations with large DOI because the increase in elevation has much greater influence on the measured ECa values for the small DOI configurations (e.g., VCP-s35) compared with the large DOI setups (e.g., HCP-s180).

Because the MECI approach for all five CPs was carried out individually, five sets of

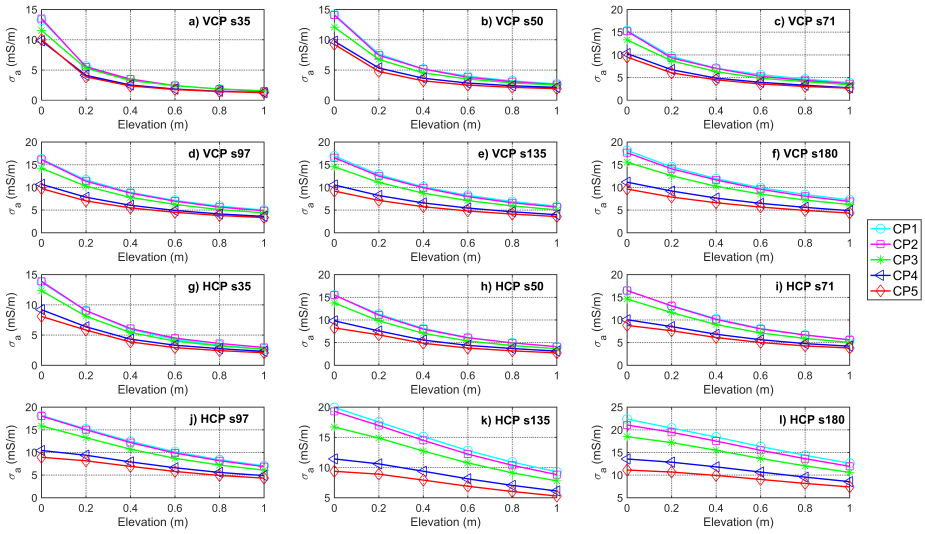

Figure 3.9: Multi-elevation EMI data sets acquired at five CPs are plotted together as a function of elevations. Results for each Tx-Rx configuration are plotted in each subplot separately.

calibration curves are obtained and plotted together with the measured ECa values in figure 3.10. For comparison, VES calibration curves were plotted. Note that calibration curves for each Tx-Rx configuration are described by one multiplicative and one additive factor.

From the results shown in figures 3.10, calibration curves obtained for VCP (figure 3.10a to 3.10f) and HCP with small coil separations (figures 3.10g to 3.10h) are very similar for the five CPs, while small deviations of the curves exist for the four larger coil separations (figures 3.10i to 3.10l). The VES based calibration curves (solid line in each subplot in figure 3.10) are similar to the MECI curves, although in figures 3.10i to 3.10l small deviations can be observed.

To investigate the quality of the calibration in more detail, calibration factors obtained from each CP were individually applied to the measured transect ECa data (figure 3.11). As expected from the earlier analysis, the MECI data (ECa^{MECI}) are in good agreement with the VES calibrated data (ECa^{VES}) for the configurations with smaller DOI (figures 3.11a to 3.11h) but show differences for the four configurations with the largest DOI (figures 3.11i to 3.11l). Note that an outlier of 15 mS/m larger than the neighboring values was removed for

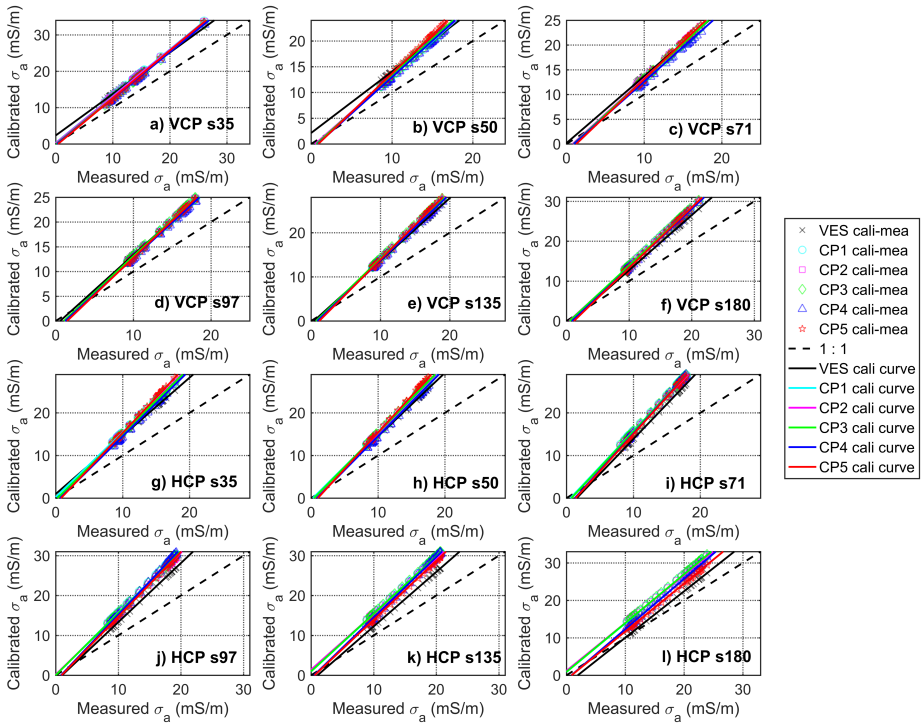

Figure 3.10: Scatter plots of calibrated ECa versus measured ECa (cali-mea) for twelve coil configurations (colored scatter markers). Each subplot contains a VES-based calibration curve (black solid line), five MECI curves obtained from five different CPs (colored solid lines), and the 1:1 line (dashed line).

the VCP s35 configuration at position 18 m (figure 3.11a).

To investigate the differences of different CPs, the STD values of ECa^{MECI} over all five CPs are calculated and presented in table 3.4 (first column). The STD shows small values from 0.16 mS/m (VCP-s180) to 1.04 mS/m (HCP-s180) with the mean value of 0.37 mS/m over all Tx-Rx configurations indicating the stability of the calibration results from different CPs. The mean shifts between the uncalibrated measured ECa data (ECa^{mea}) and the ECa^{VES} for each Tx-Rx configuration varies from 1.77 mS/m (HCP-s180) to 6.06 mS/m (HCP-s71, table 3.4, second column). Looking at the mean shifts between ECa^{mea} and ECa^{MECI}, even larger shifts are obtained having values between 3.57 mS/m (VCP-s35) and 7.87 mS/m (HCP-s97, table 3.4, third column). These results show that the calibration is necessary, and mean

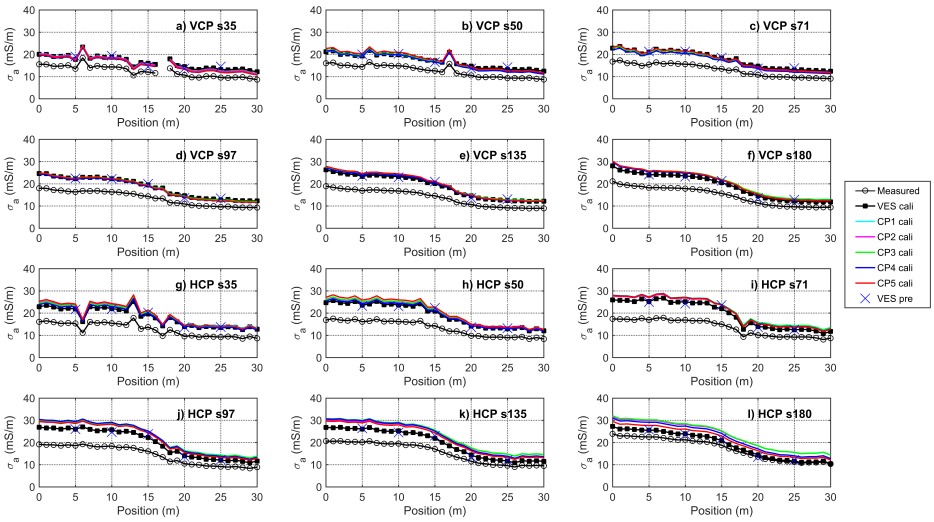

Figure 3.11: (a)-(f) VCP, and (g)-(l) HCP MECI ECa values (colored solid lines) along the transect line are shown together with un-calibrated EMI data (solid line with circle markers), and VES calibrated EMI data (solid black lines with filled square markers). The VES predicted ECa values at the five CPs are indicated with the blue crosses.

Table 3.4: First column shows the standard deviation (STD) between the five individually calibrated transect ECa values using the multi-elevation data from the five calibration positions (CP), as shown in figure 3.10. Second, third and fourth columns show the mean absolute shifts between un-calibrated data (ECa^{mea}) and VES calibrated data (ECa^{VES}), un-calibrated data (ECa^{mea}) and MECI data (ECa^{MECI}), and VES calibrated data (ECa^{VES}) and MECI data (ECa^{MECI}), respectively over all positions as shown in figure 3.10, including their means over all Tx-Rx configurations.

Tx-Rx configuration	STD of ECa^{MECI} over five CPs (mS/m)	Mean shift of ECa^{mea}-ECa^{VES} (mS/m)	Mean shift of ECa^{mea}-ECa^{MECI} (mS/m)	Mean shift of ECa^{VES}-ECa^{MECI} (mS/m)
VCP s35	0.30	4.12	3.57	0.68
VCP s50	0.39	4.54	4.28	0.60
VCP s71	0.32	4.74	4.34	0.46
VCP s97	0.20	4.80	4.59	0.26
VCP s135	0.19	5.15	5.79	0.64
VCP s180	0.16	4.47	5.77	1.29
HCP s35	0.40	5.55	6.57	1.05
HCP s50	0.45	6.04	7.05	1.02
HCP s71	0.19	6.06	7.79	1.73
HCP s97	0.30	5.41	7.87	2.46
HCP s135	0.52	4.23	7.37	3.14
HCP s180	1.04	1.77	5.34	3.57
Mean	0.37	4.74	5.86	1.41

Table 3.5: Absolute shifts between VES calibrated data (ECa^{VES}) and MECI data (ECa^{MECI}) for each Tx-Rx configuration (rows) and calibration position (columns) with the corresponding mean values. The second column shows the depth of investigation (DOI) for each Tx-Rx configuration.

Tx-Rx configuration	DOI (m)	ECa^{VES}-ECa^{MECI} (mS/m)				
		CP1	CP2	CP3	CP4	CP5
VCP s35	0.26	0.40	0.45	0.80	0.95	0.80
VCP s50	0.38	0.57	0.51	0.55	0.60	0.79
VCP s71	0.53	0.34	0.25	0.35	0.96	0.39
VCP s97	0.73	0.16	0.16	0.15	0.54	0.28
VCP s135	1.01	0.59	0.59	0.83	0.37	0.81
VCP s180	1.35	1.39	1.30	1.49	1.07	1.21
HCP s35	0.53	1.19	1.10	0.97	0.55	1.44
HCP s50	0.75	0.93	1.02	1.17	0.40	1.60
HCP s71	1.07	1.96	1.63	1.91	1.65	1.51
HCP s97	1.46	2.72	2.33	2.59	2.66	1.99
HCP s135	2.03	3.47	3.29	3.60	3.04	2.29
HCP s180	2.70	4.26	4.20	4.36	3.05	1.97
Mean		1.50	1.40	1.56	1.32	1.26

ECa shifts of about 5 mS/m are present in the measured data, which cannot be ignored for a quantitative analysis and an inversion. Shifts are similar to the previous investigations carried out on the same test site (Lavoué et al., 2010; von Hebel et al., 2014).

When comparing ECa^{VES} with ECa^{MECI} (table 3.4, fourth column), the mean shift returns the smallest value for the configuration VCP-s97 (0.26 mS/m). It shows slightly increasing differences up to 0.68 mS/m (VCP-s32) for the coil separations smaller than 0.5 m. This is probably due to a decreased sensitivity of the used VES model for the upper centimeters of the subsurface. The shift is afterward increasing with increasing DOI returning values of up to 3.57 mS/m for the largest coil separation in HCP orientation. This is possibly because that the VES measurement has a larger sensitivity for deeper depths than that of the EMI measurement after lifting the system.

For a more detailed analysis, the mean absolute shifts between ECa^{MECI} and ECa^{VES} are summarized in table 3.5 for all five CPs, individually. The largest misfit value of 4.36 mS/m is returned for HCP-s180 at CP3, whereas CP5 returns the smallest value of 1.97 mS/m (table 3.5, the row of HCP-s180). Similar results are observed for HCP-s97 and HCP-s135. In general, table 3.5 shows a trend that the deviation is related to the DOI, however, the

detailed relationship needs to be investigated in more detail in future studies. In addition, CP3 shows the largest mean misfit (1.56 mS/m), whereas CP5 returns the smallest value of 1.26 mS/m. Therefore, the transect data was inverted using the uncalibrated (measured), the VES calibrated, and the MECI data sets from positions CP3 and CP5.

3.7.2 Two-layer Inversion of Uncalibrated and Calibrated EMI Data

A two-layer inversion algorithm adapted from von Hebel et al. (2014) was applied to uncalibrated and calibrated EMI data sets. Subsurface models at all thirty-one locations of the transect were reconstructed and stitched together to present the lateral and vertical electrical conductivity distribution of the subsurface along the transect. The obtained subsurface images are presented in figures 3.12 showing the inversion of uncalibrated (measured) (figure 3.12a), VES calibrated (figure 3.12b), CP3 MECI (figure 3.12c), and CP5 MECI EMI data (figure 3.12d). Note that inversion results from multi-elevation calibrated data using CP3 and CP5 are selected to show representative results for a heterogeneous and a homogeneous calibration location, respectively.

The uncalibrated data inversion result acquired using the mentioned system and setup does not resolve a subsurface layering (figure 3.12a). After applying the VES calibration (figure 3.12b) the known subsurface layering (von Hebel et al., 2014) is well reconstructed. Furthermore, the two results from the MECI approach (figure 3.12c and d) return similar electrical conductivity distributions as the VES calibration. Both resolve the resistive upper layer (10-15 mS/m) as well as a conductive lower layer (about 30 mS/m) in the first 17 m of the transect. For the low conductive region of the transect (position 19 to 31 m), results show differences in the deeper subsurface that were already indicated by the different calibration results for HCP-s180 (figure 3.11(l), and table 3.5).

When comparing with the VES-based calibration results, the deeper subsurface from the CP5-calibration shows a better agreement than that from CP3. Furthermore, in the low conductive area (position 19 to 31 m), a shallow layer is visible in the results from the CP5-calibration (figure 3.12d) with only minor conductivity contrast, which is not resolved by the VES calibrated data. To sum up, the CP with the most homogeneous and low-conductive soil, such as CP5, where no significant electrical conductivity changes occur in the deeper

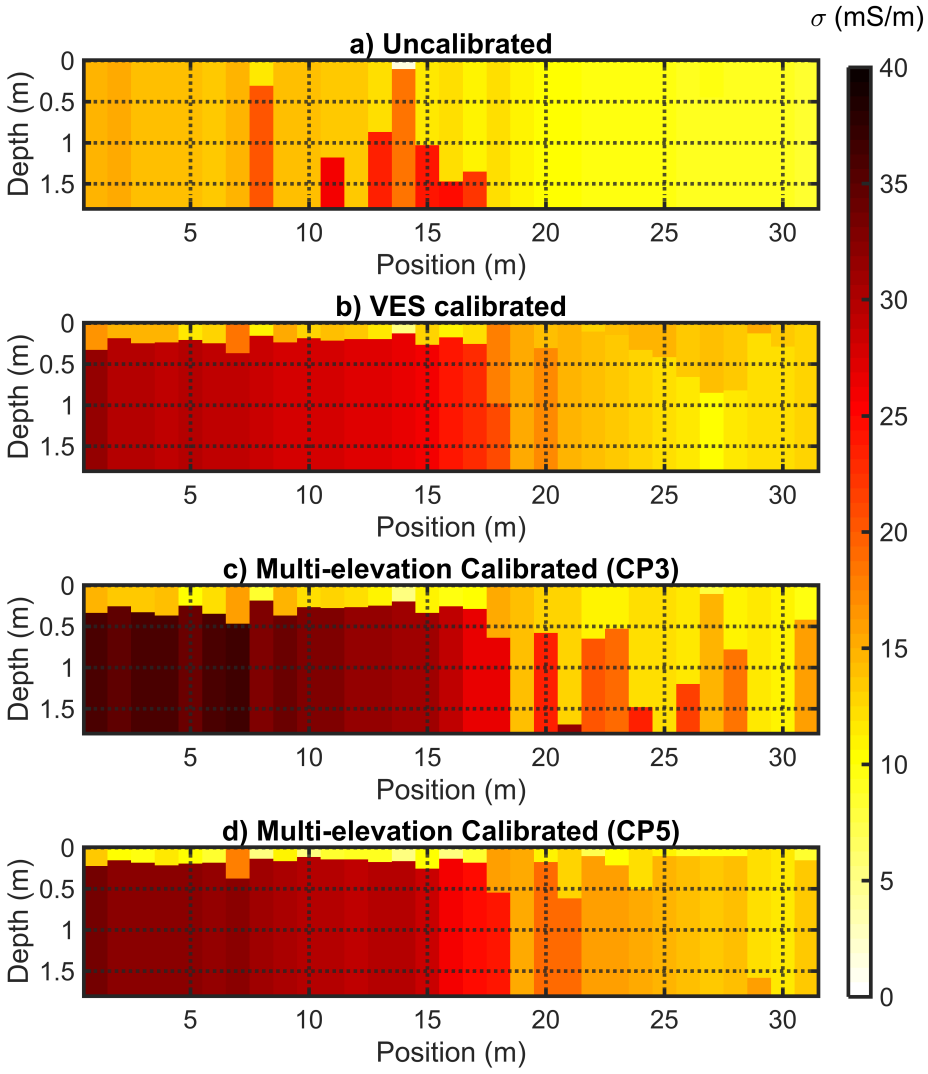

Figure 3.12: (a) Two-layer inversion results using measured EMI data without calibration. Two-layer electrical conductivity inversion results of the transect line using calibrated EMI values obtained based on (b) VES data using all CPs, and MECI method using data from (c) CP3, and (d) CP5.

depth, shows the most detailed inverted subsurface electrical conductivity distribution of the transect. In particular, the shallow plow layer could be resolved probably due to the higher sensitivity of the elevated EMI compared with the VES based calibration results. This plow layer has also been visible in EMI data (von Hebel et al., 2014; von Hebel et al., 2018) and many soil cores obtained from surrounding fields (Brogi et al., 2019).

3.8 Conclusion

The present chapter introduced a multi-elevation calibration and inversion (MECI) approach that returns a multi-layer subsurface model together with multi-configuration EMI calibration factors. The verifications with synthetic homogeneous, two-layer, and three-layer subsurface models plus artificial calibration factors returned good reconstructions of the input models and calibration factors, indicating the validity of this algorithm. When processing the EMI data acquired over a 30 m long transect at a test site with an electrical conductivity range from 5 to 30 mS/m, the ECa values shifted from 2 to 10 mS/m with the mean shift of 5 mS/m, indicating that the calibration is necessary to obtain quantitative ECa values. Similar calibrated ECa values with maximum mean standard deviations of 0.37 mS/m were obtained from the five independent Cps, which demonstrates the stability of this calibration approach.

One single CP can be used for the MECI approach, which significantly reduces the measurement time from about 1 hour for the five VES calibration measurements to 15 munites for one multi-elevation calibration.

The synthetic and experimental data analyses show the ability of the presented MECI approach for obtaining quantitative EMI values together with an inverted subsurface model at the CP. The inverted subsurface electrical conductivity distribution of the transect indicates that the MECI approach enables an improved imaging of the shallow layers, and that including EMI data with larger DOI will probably improve the sensitivity at deeper depths. These results indicate the potential of the EMI system to quantitatively characterize the subsurface electrical conductivity distribution without relying on any additional methods, which is different compared with the conventional calibration methods presented for portable rigid-boom single-frequency multi-configuration EMI systems. Consequently, this MECI approach significantly improves the experimental efficiency of EMI in terms of mobility and speed for

all applications in which EMI is used and for all state of the art commercial EMI systems.

4. Field Applications of MECI and Comparisons with Electrode-based Calibration Methods

The previous chapter introduced the MECI approach and verified the method by using a hand-held EMI instrument. To further investigate the applicability of this method, the current chapter expands the MECI towards experimental large-scale field measurements for multiple EMI instruments and setups.

The measurement-system studied here includes two different EMI instruments providing eighteen different Tx-Rx configurations in total. The EMI instruments are mounted on two customized plastic sleds including DGPS which are designed for large-scale field EMI measurements.

EMI measured data were obtained from a 60 m long transect. Similar to chapter 3, the VES-based calibration method is used to compare with the MECI results. In addition, ERT measurements showing the 2D electrical contribution of the subsurface were also investigated and are presented in the current chapter as cross-validations.

4.1 EMI Instruments

The EMI devices used in this chapter include the CMD-Special Edition abbreviated as SE (GFinstruments, Brno, Czech Republic) which was previously used in chapter 3, together with a CMD-MiniExplorer (GFinstruments, Brno, Czech Republic) with different coil con-

figurations to provide additional information about the subsurface. The CMD-MiniExplorer (ME) uses 30 kHz as the excitation frequency and contains three coil separations which are 0.32, 0.71, and 1.18 m (hereafter referred to as s32, s71, and s118) for both HCP and VCP orientations. Similar to the sensitivity analysis for the SE (chapter 3, figure 3.2), the sensitivity images of the ME system at the same six elevations (0, 0.2, 0.4, 0.6, 0.8, and 1.0 m) are presented in figure 4.1.

Table 4.1: Depth of investigation (DOI) for each Tx-Rx configuration

DOI Index	DOI (m)	Tx-Rx Symbol	Tx-Rx Configuration	DOI Index	DOI (m)	Tx-Rx Symbol	Tx-Rx Configuration
1	0.24	c_1	ME VCP s32	10	0.86	c_3	ME VCP s118
2	0.26	c_7	SE VCP s35	11	1.01	c_{11}	SE VCP s135
3	0.37	c_8	SE VCP s50	12	1.07	c_5	ME HCP s71
4	0.48	c_4	ME HCP s32	13	1.07	c_{15}	SE HCP s71
5	0.53	c_{13}	SE HCP s35	14	1.35	c_{12}	SE VCP s180
6	0.53	c_2	ME VCP s71	15	1.46	c_{16}	SE HCP s97
7	0.53	c_9	SE VCP s71	16	1.77	c_6	ME HCP s118
8	0.73	c_{10}	SE VCP s97	17	2.03	c_{17}	SE HCP s135
9	0.74	c_{14}	SE HCP s50	18	2.70	c_{18}	SE HCP s180

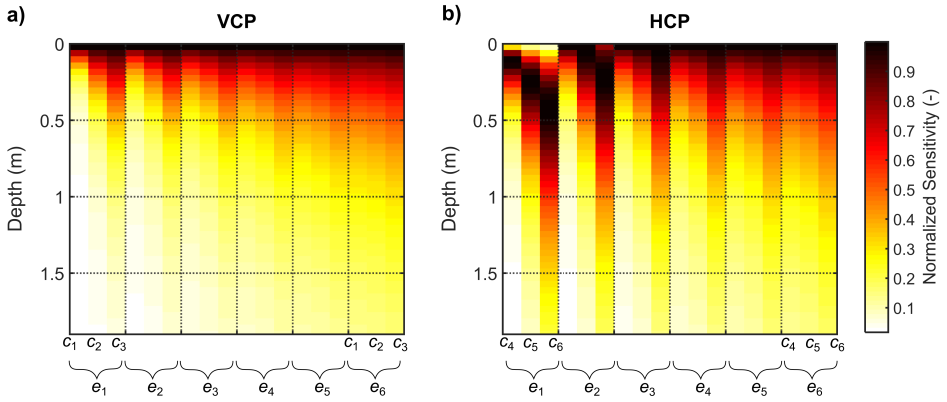

Figure 4.1: Normalized sensitivity for the CMD-MiniExplorer (ME) system as a function of coil separations and elevations for (a) VCP (c_1, c_2, c_3) and (b) HCP configurations (c_4, c_5, c_6). The six elevations ($e_1, \cdots, e_6$) are 0.0, 0.2, 0.4, 0.6, 0.8, and 1.0 m, respectively. Each sensitivity column is normalized for each elevation and Tx-Rx configuration as shown in Figure 3.2.

Table 4.1 shows the DOI of the ME and SE configurations when measuring on the ground surface in the order of increasing DOI. In order to analyze the overall DOI for each Tx-Rx configuration after accounting for all elevations, the total sensitivity images are calculated

and shown in figure 4.2. Note that for SE the sensitivity information has already been shown in chapter 3, but is repeated here for completeness. These sensitivity images for elevated instruments are obtained by summing the sensitivity columns from all elevations and then normalizing for each Tx-Rx configuration. The total sensitivity for all elevations results in a maximum DOI of about 0-1 m and 0-2 m for the VCP-s180 and the HCP-s180 configurations, respectively. In comparison with the maximum DOI measured on the ground (table 4.1), which returned the value of 0-1.4 m for VCP-s180 and 0-2.7 m for HCP-s180, elevating the EMI instrument leads to a decreased total-sensitivity depth. Consequently, the experimental analysis of the subsurface which will be discussed in the following sections is focused on the upper 2 m.

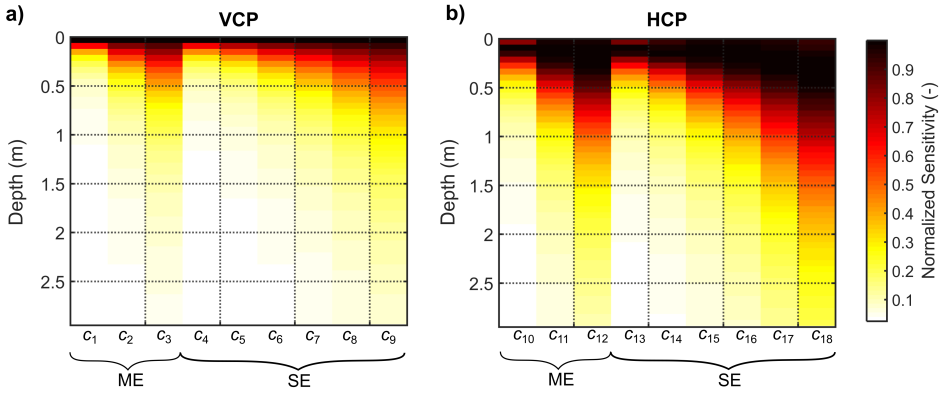

Figure 4.2: Total sensitivity images for (a) VCP and (b) HCP configurations by summing all elevations together for both ME (c_1, c_2, c_3, and c_{10}, c_{11}, c_{12}) and SE systems ($c_4, \cdots, c_9$, and $c_{13}, \cdots, c_{18}$). The sensitivity is normalized by each Tx-Rx configuration.

4.2 Study Field

The study field in this chapter belongs to the TERrestrial ENvironmental Observatories (TERENO, Bogena et al., 2018) and the Transregional Collaborative Research Centre 32 (SFB-TR32, Simmer et al., 2015) site in Selhausen, and is approximately 350 m away from the bare soil test site investigated in chapter 3. The survey area around the selected field is characterized as Upper Terrace (UT). The soil is dominated by Pleistocene sand and gravel sediments (Rudolph et al., 2015; Patzold et al., 2008). A Paleo-river channel system, which belongs to the Rhine/Meuse river system, is present under the survey area and is filled

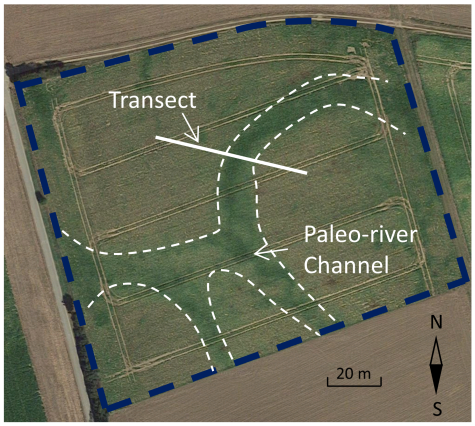

Figure 4.3: Satellite image (Google Map) of the survey area with visible paleo-river channels. Two transect lines T1 and T2 are selected across the river channels.

with aeolian sediments (Klostermann, 1992). According to previous subsurface investigations by von Hebel et al. (2018), the paleo-river channels are at around 1 m depth. Large-scale EMI measurements show increased ECa values above the paleo-river channel paths (Brogi et al., 2019), which are also visible from the satellite image shown in figure 4.3 for the field under investigation indicating correlations between crop patterns and ECa values. The transect crossing the paleo-river channels was selected with a length of 60 m (figure 4.3). The measurements were performed in May, 2018. Before the measurement day, there was an overnight raining. Note that the fertilization had been performed approximately two weeks prior to the measurements. In addition, corn plants were seeded resulting in seedlings with maximum height of about 5 cm. Those factors might have influences on the measurement data which need to be taken into account for when analyzing the measurement results.

4.3 EMI Measurement Setup

In contrast to the EMI measurements carried out in chapter 3 using the hand crutch provided by the manufacturer, here, ME and SE are mounted on two customized plastic sleds (von Hebel, 2016) which are used for large-scale field measurements. The corresponding data logger as well as a DGPS system are fixed to the central pole of each sled. As an example, the measurement setup for SE is shown in figure 4.4. During the EMI measurement, each

sled was dragged manually along the transect while the logger was continuously recording the EMI data and GPS coordinates.

The multi-elevation calibration setup designed in chapter 3 (figure 3.7), is suitable for lifting the EMI-crutch but not for the EMI-sled setup in the current study. Therefore, multiple polypropylene boxes (figure 4.4) are successively stacked to increase the height and lifting the EMI-sled setup. Two types of boxes are used having heights of 0.175 m and 0.32 m to lift the EMI-sled to seven elevations: 0, 0.175, 0.320, 0.495, 0.640, 0.815, and 0.960 m.

Performing one multi-elevation measurement for seven elevations took about 15 minutes. For two EMI devices with two orientations (VCP, HCP), the complete data acquisition of the multi-elevation measurements took about 1 hour in total for one calibration position.

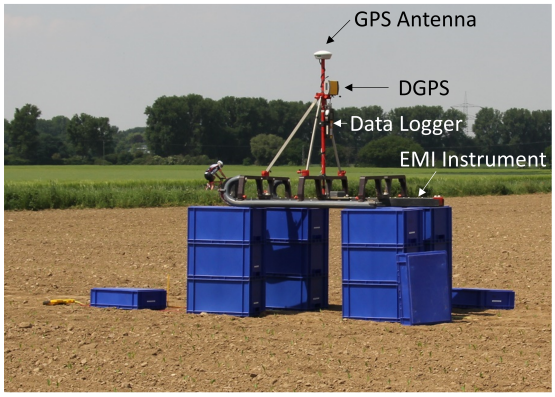

Figure 4.4: Measurement setup for the SE system for the multi-elevation calibration method. The EMI system is mounted on a custom designed plastic sled (von Hebel, 2016). Plastic boxes are used to lift the system above the ground to measure at multiple elevations.

4.4 Verification Data

Similar to chapter 3, VES measurements were performed to verify the results obtained from the MECI. Meanwhile, more elaborate ERT measurements were carried out in the current chapter as cross-validations returning detailed inverted subsurface images due to the use of a large number (120) of electrodes.

The inverted subsurface models were obtained individually from the corresponding VES

and ERT measurements. In the next step, the predicted ECa values were obtained from these inverted models and were applied to the linear-regression calibration method (Lavoué et al., 2010) returning multiplicative and additive calibration factors. In addition, the inverted soil models of the transect were obtained using the calibrated ECa values. For verification purposes, both the calibration and inversion results were compared with the MECI results.

4.4.1 Electrical Resistivity Tomography (ERT)

Two ERT measurements were carried out along the transect using a Syscal Pro instrument (IRIS Instruments) with 120 electrodes in Dipole-Dipole array configuration. One measurement used an electrode distance of 0.25 m resulting in a 30 m long survey line (presented as ERT-30). The other measurement used an electrode distance of 0.5 m resulting in a 60 m long line (presented as ERT-60). Each measurement took about 3 hours. When exporting the measured data from Prosys (IRIS Instruments), an automatic filtering together with a standard deviation of 2.5% were applied.

ERT Inversion without Electrode Correction

A robust inversion was applied based on the L1-norm inversion algorithm in RES2DINV (Geotomo Software) with a data-inversion-constraint cutoff factor of 0.05. This inversion algorithm solves for subsurface models with sharp interfaces between different layers. Inverted results of the transect line from both the ERT-30 and ERT-60 measurements (figure 4.5) returned sharp-layered electrical conductivity distributions with higher conductivity values at the location of the paleo-river channel (> 35 mS/m) compared to conductivity values from 5 to 10 mS/m for the rest of the transect. Note that the ERT-30 (figure 4.5a) was measured at the locations from 11.1 to 41.1 m of the transect, whereas the ERT-60 (figure 4.5b) was measured on the complete transect. The inverted result of ERT-60 includes the results down to the maximum depth of around 6.5 m while the ERT-30 returned the inverted results down to a depth of about 3.25 m. Because of the small electrode distance which improves the resolution for the shallow depth, the inverted subsurface from the ERT-30 measurements returned a thin upper layer with high electrical conductivities. Whereas this thin layer is only partly visible from the ERT-60 results due to the reduced sensitivity for the shallow

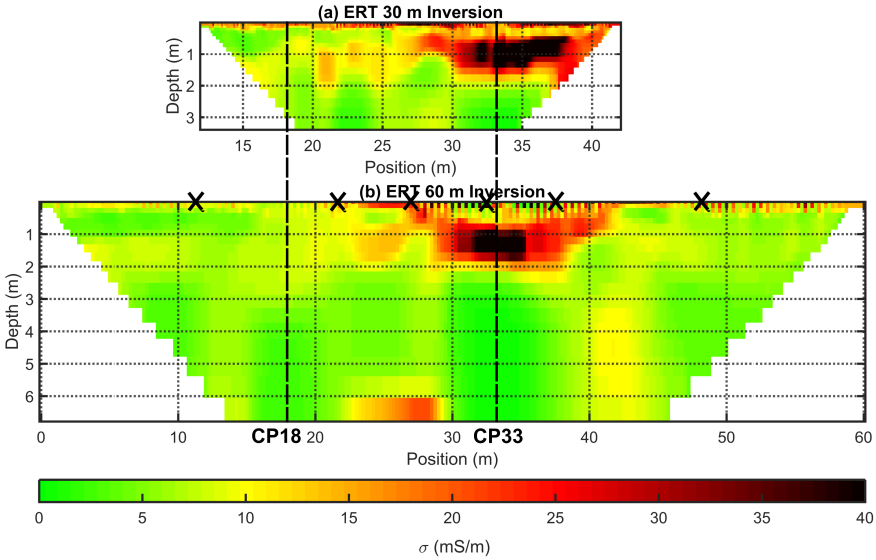

Figure 4.5: 2D electrical conductivity distributions of the transect without electrode correction using ERT-30 (upper) and ERT-60 (lower) measurement data. The six black crosses in the lower plot show the six locations of VES measurements. Two calibration positions for the MECI are indicated as CP18 and CP33.

subsurface caused by a large electrode distance.

Selecting Calibration Positions for MECI and VES Methods Based on the ERT Data

Considering the discussions in section 3.7 about the selection of the calibration position for MECI method, two CPs were selected indicated in figure 4.5a, one of which is above a relative homogeneous subsurface at 18 m (CP18) while the other is above a horizontally layered subsurface at 33 m (CP33), respectively. In addition, the locations of VES measurements are shown as the black markers in figure 4.5b for later comparisons between ERT and VES data. Note that CP33 is above the paleo-river channel. In addition, the MECI was performed to obtain both 2-layer and 3-layer inverted models for each CP using the approach described in section 3.3. The obtained calibration parameters were applied to the EMI data such that two possible calibrations for the EMI transect data were obtained.

ERT Inversion with Electrode Correction (ERTec)

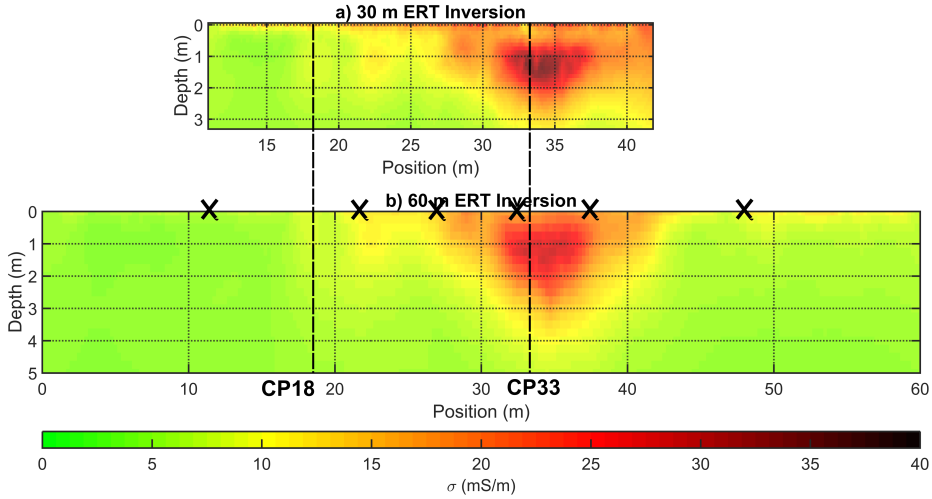

Figure 4.6: 2D electrical conductivity distributions of the transect inverted by Ochs et al. (2019) using a smoothness constraint inversion algorithm with electrode correction for the shallow depth (Rücker et al., 2017). The six black crosses in the lower plot show the six locations of VES measurements. Two calibration positions for the MECI are indicated as CP18 and CP33.

The ERT measured data were additionally inverted by Ochs et al. (2019) to reduce the electrode effect (presented as ERTec-results from here on) for the shallow subsurface using a smoothness-constraint finite element Gauss-Newton inversion algorithm (Günther et al., 2006; Rücker et al., 2017). The inversion was performed using BERT (pyGIMLi) including the electrode correction for 7 cm long electrodes with perfect coupling to the ground. The regularization factor, which controls the strengths of the smoothness constrains (Günther et al., 2006), was set to 100 and 300 for ERTec-30 and ERTec-60, respectively. For plotting, 2D electrical distributions for both ERTec-30 and ERTec-60 of the transect (figure 4.6) were obtained with a regular grid size of 0.125 m by 0.125 m. It is observed from figure 4.6a that the high-conductivity layer in the shallow subsurface is visible with an average value around 25 mS/m, whereas this layer is not visible from the inverted ERT-60 results (figure 4.6b).

The inversion model after electrode correction shows smoother results for the shallow subsurface whereas the upper layer returned from the conventional ERT result contains artificial discrete blocks possibly due to electrode effects. This indicates that different inversion algo-

rithms reveal different inverted models (figure 4.5 and figure 4.6) due to the non-uniqueness, different inversion parameters, and smoothness constraints. In the current study, both the ERT- and the ERTec-based data were analyzed to obtain completed information/understandings of the measured subsurface.

When calibrating the EMI data, 30 m data sets were used for both the ERT and ERTec calibrations because of the higher resolutions due to the smaller electrode distance in comparison to the 60 m data. This small electrode distance also matches the minimum electrode distance of the VES measurement setup (0.25 m). In addition, due to the reduced sensitivity at the start and end of the ERT electrode array, both the first and last 5 m of the ERT and ERTec data sets were excluded during the calibration process.

4.4.2 Vertical Electrical Sounding (VES) Measurements

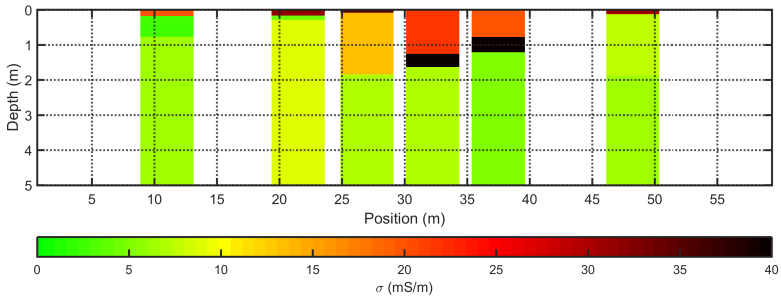

Figure 4.7: Inverted electrical conductivity distributions of six VES locations of the transect. These six locations are at 11.1, 21.6, 27.1, 32.3, 37.5, and 48.1 m, respectively. Note that the subsurface image of each location is extended to approximately 5 m width for a better visualization.

Six locations along the transect were selected for VES measurements which were at 11.1, 21.6, 27.1, 32.3, 37.5, and 48.1 m, respectively. The same VES configuration as described in section 3.6.2 was used with a minimum distance of 0.25 m between the current and potential electrodes. The inverted electrical conductivity distributions of the six corresponding locations were obtained using a 3-layer VES inversion algorithm implemented by von Hebel (2016), and are presented in figure 4.7. Note that the subsurface image of each location is extended to approximately 5 m of width for a better visualization.

The inverted results returned a relatively homogeneous subsurface at the beginning and

end of the transect while resolving a highly conductive-layer between 1 and 2 m depth with a strong conductivity contrast when measuring above the paleo-river channel. It is also observed that a thin upper layer of about 0.1 m thickness with high conductivity values (from about 20 to 35 mS/m) is obtained at the beginning and end of the transect. According to the time-lapse measurements from August 2017 to May 2018 by Iwanowitsch (2018) on the same test site, the upper layer of the soil shows strongly increased measured ECa values after the fertilization which is the reason for this inverted thin upper layer with high conductivity.

4.5 MECI Data

The measured ECa values for multiple elevations at two CPs are presented in figure 4.8 (black solid curves). CP33 returned larger values than CP18 for all Tx-Rx configurations, indicating a more conductive subsurface at CP33.

Moreover, when lifting the EMI system more than 0.5 m above the ground, measured ECa values acquired by the configurations with small DOIs (i.e., ME-VCP-s32, ME-HCP-s32, and SE-VCP-s35) approached stable values, whereas large DOI configurations such as ME-HCP-s118 and SE-HCP-s180 still show decreasing values. This is because of the limited spatial sensitivity of the small DOI configurations after lifting the system whereas large DOI configurations can still sense the upper part of the soil. This behavior also explains the similar values at regions with different conductivity that were measured by small DOI configurations at the highest elevation (for instance, ME-VCP-s32 at an elevation of 0.96 m in figure 4.8a). Meanwhile, negative values were returned by small Tx-Rx separations with the minimum value of about −14 mS/m (ME-VCP-s32 at an elevation of 0.96 m), which is different from the hand-held EMI setup investigated in chapter 3.7 (figure 3.9) showing the value of about 1 mS/m at an elevation of 1 m. These values measured by the sled-based EMI setup indicate large ECa shifts probably due to the electronic devices (GPS, cables, etc.) installed within the sensitivity volume of these Tx-Rx configurations.

In general all MECI calibrated data show higher ECa values compared to the uncalibrated data except for the ME-HCP-s71 configuration. At CP18, small deviations between calibrated and uncalibrated ECa values were returned for the large DOI configurations (such as ME-VCP/HCP-s118, SE-HCP-s135, and SE-VCP/HCP-s180), whereas the differences for

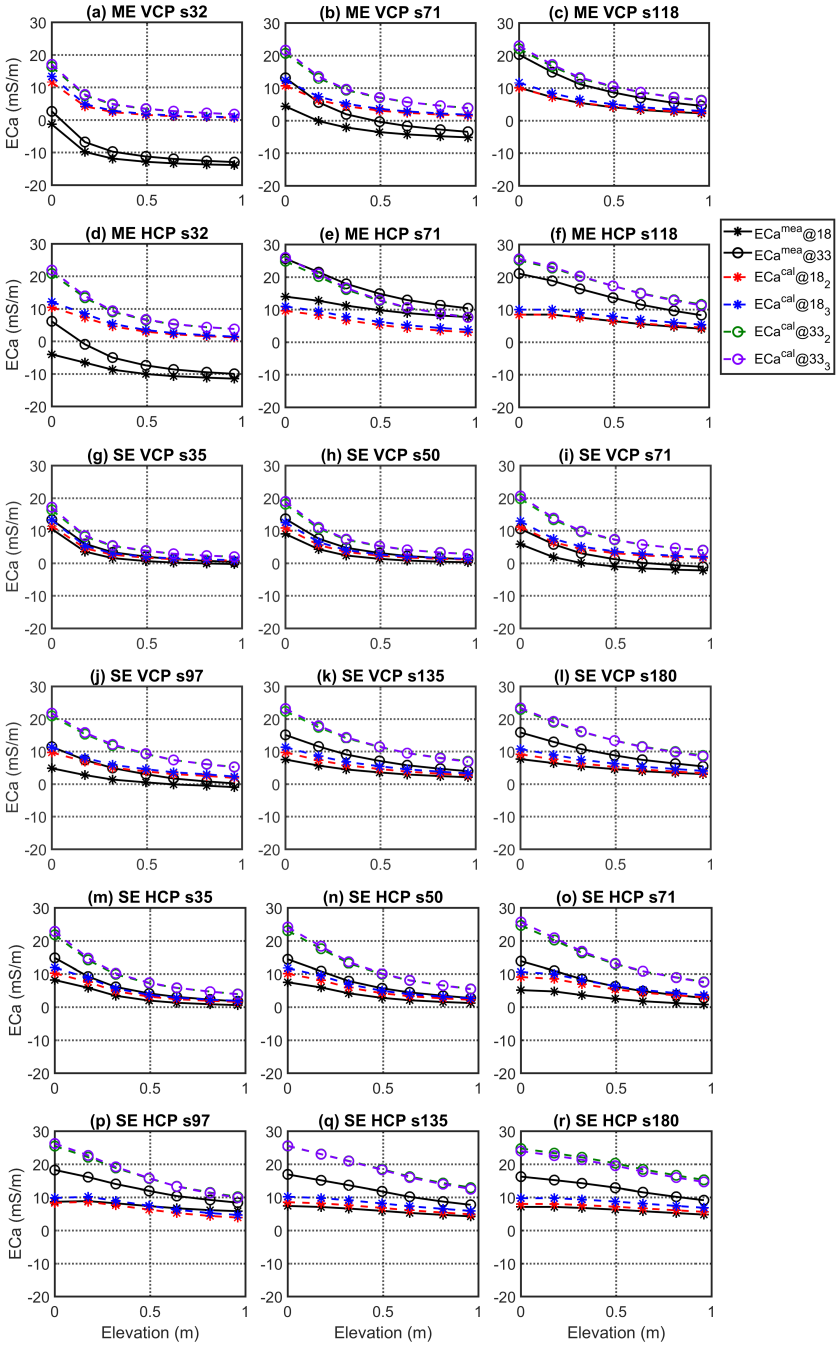

Figure 4.8: Uncalibrated EMI data at multiple elevations measured at CP18 (black solid curves with stars), and CP33 (black solid curves with circles). Calibrated EMI data obtained from the 2-/3-layer MECI approach at CP18 (red and blue color curves with stars), and CP33 (green and purple curves with circles).

these configurations are bigger at CP33. The misfit of both 2- and 3-layer results at CP18 returned the value of about 3% while smaller values of about 2% were returned by CP33.

When comparing the results between 2- and 3-layer MECI at CP18 (figure 4.8, red and blue curves with stars), the 3-layer calibrated results obtained from large DOIs (such as ME-VCP-s118, ME-HCP-s71 and -s118, SE-VCP-s135 to -s180, SE-HCP-s97 to -s180) show larger ECa values than the 2-layer results with the differences of up to about 2 mS/m. Contrary, the 2- and 3-layer results from CP33 (figure 4.8, green and purple curves with circles) show small differences (below 0.5 mS/m) for all configurations except for the SE-HCP-180 with slightly larger difference, but still within 1 mS/m.

4.6 Inverted Soil Model Comparisons between MECI and the Three Verification Methods at Two CPs

When looking at the inverted subsurface models obtained from 2-/3-layer CP18 MECI (figure 4.9a), it is observed that the 3-layer inversion (figure 4.9a, blue) returned a thicker and more conductive shallow layer (with the thickness of about 0.5 m and the electrical conductivity of about 15 mS/m), whereas the 2-layer inverted model (figure 4.9a, black) returned a less conductive upper layer (with the electrical conductivity of about 13 mS/m) with smaller thickness of about 0.3 m. These different inverted upper layers are the possible reason for the deviations of the calibrated ECa values shown in figure 4.8, considering that the ECa values measured by the configurations with large DOIs mainly contain the information from the upper layer after lifting the EMI system above the ground. Similar calibrated ECa values returned from the 2- and 3-layer MECI at CP33 shown in figure 4.8 can be explained by the similar inverted upper layers shown in figure 4.9b. Nevertheless, more detailed data analyses are needed in the following sections to evaluate the performance of the 2-/3-layer MECI.

For comparison, the inverted models from the three verification measurements are also presented in figure 4.9. Two inverted soil models from the VES measurements (green curves in figure 4.9) were obtained at the locations of 21.6 m and 32.3 m (shown in figure 4.7) which are closest to CP18 and CP33, respectively. The ERT and ERTec inverted models (red and magenta curves in figure 4.9) were obtained from figure 4.5a and 4.6a, respectively, with error

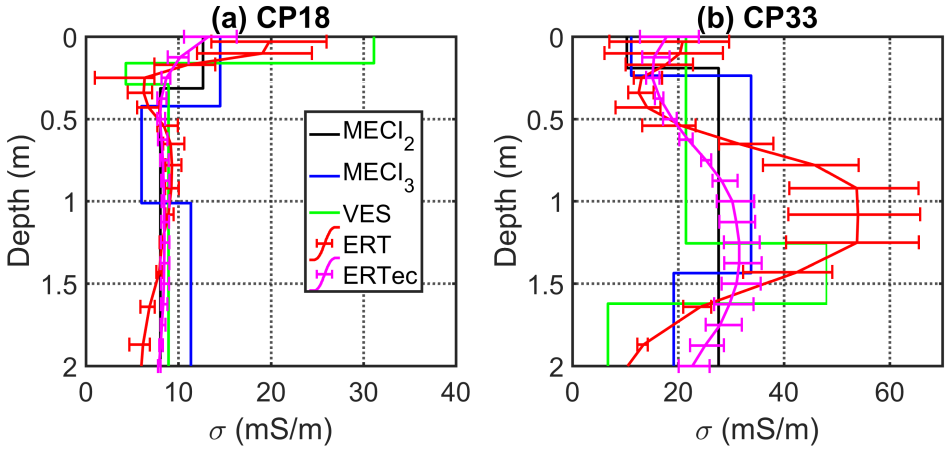

Figure 4.9: Soil models obtained from 2-layer (black) and 3-layer (blue) MECI at the location (a) CP18 and (b) CP33. Two inverted soil models from the VES measurements (green curves in figure 4.9) were obtained at the locations of 21.6 m and 32.3 m (shown in figure 4.7) which are closest to CP18 and CP33, respectively. The ERT and ERTec inverted models (red and magenta curves in figure 4.9) were obtained from figure 4.5a and 4.6a, respectively, with error bars showing the mean values of soil models over 2 m around the two CPs.

bars showing the mean values of soil models over 2 m around the two CPs. The value of 2 m is determined based on the approximate electromagnetic footprint of the EMI devices used in the current study.

For CP18, good agreements were returned between MECI and the three verification methods (as shown in figure 4.9a), except for the shallow depth where a highly conductive layer was returned from VES and ERT data. Regarding this upper layer showing divergences between EMI and electrode-based data, some potential causes such as the fertilization which might have changed the ion concentrations of the upper soil, overnight rains/plant growth holding up water content that increase the galvanic coupling effects, and the electrode effect, need to be further analyzed including the different sensitivities for this very shallow subsurface. With respect to the electrode effects, an electrode correction (ERTec) was analyzed showing a less conductive layer that is more similar to the MECI results.

For CP33 (figure 4.9b), differences were revealed from different measurements. In general, the MECI results match with the ERTec results the most. For the ERT inverted soil model, a large error bar was returned especially for the highly conductive layer (between the depths from 0.8 to 1.5 m) where the paleo-river channel is located. This large deviation

indicates a rapid change in the electrical conductivity around the position of CP33 due to the sharp-layered inversion algorithm, whereas the ERTec returned gentle inversion results indicated by the relatively small error bar. This sharp-inversion of the ERT result is also indicated by the deeper layer (below the paleo-river channel, from 1.5 m to 2 m) showing decreased σ values that are smaller than ERTec and MECI results. In a similar way to the ERT inversion, results obtained from VES returned even smaller σ value for this deeper layer. Deviations revealed from all these inversions can be due to many factors such as the complexity of the subsurface, the different algorithms used in the inversion, the corresponding inversion parameters, and the different spatial sensitivity of the used methods. Further investigations will be discussed together with the calibration and inversion results for the whole transect.

4.7 Calibration Results of the Three Verification Methods

Figure 4.10 presents the measured (uncalibrated, 4.10a), VES calibrated (4.10b), ERT calibrated without (4.10c), and with electrode correction (4.10d) EMI data of the transect. As expected, the uncalibrated EMI data show erroneous shifts especially for the small coil separations (VCP-s32, and HCP-s32) which returned negative ECa values. When comparing different calibration results shown in figure 4.10b to d, good agreements were achieved for all the three results at the locations of the paleo-river channel (about 20 to 40 m of the transect) returning similar peak values of about 20 mS/m for all the configurations. For the relatively low conductive areas located at 0 to 20 m and 50 to 60 m of the transect, variations between each configuration were returned by VES (figure 4.10b) and ERT (figure 4.10c) results returning differences of up to about 10 mS/m, whereas ERTec-calibrated values indicate a more homogeneous subsurface with the variations within 5 mS/m. Nevertheless, ECa values from ERTec for the small Tx-Rx separations such as ME-VCP-s32 and SE-VCP-s35 are still a bit higher (up to about 3 mS/m) than the other Tx-Rx separations.

In order to investigate the performance of the different calibration approaches in more detail, the predicted ECa obtained from the three verification methods are plotted against the measured ECa for each coil configuration in figure 4.11, together with the obtained linear regression curves and the corresponding root mean square (R^2) values.

For the coil configurations that have small DOI, i.e., ME-VCP-s32, SE-VCP-s35, and

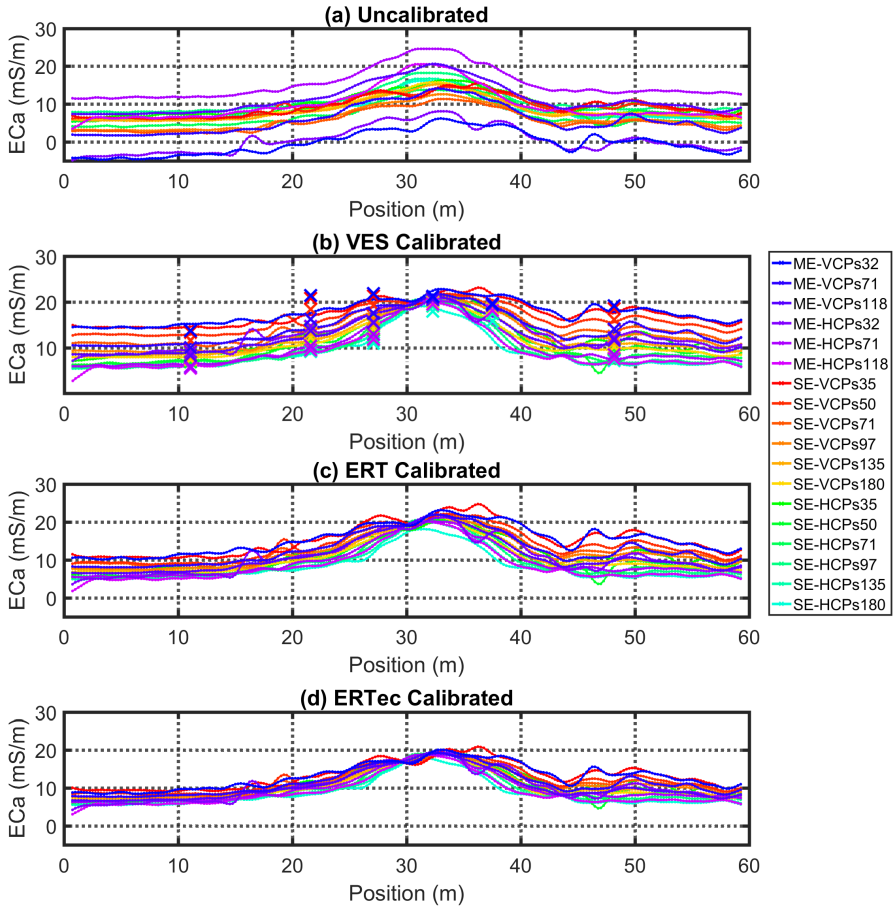

Figure 4.10: (a) Un-calibrated EMI data, calibrated EMI data based on (b) VES calibration, (c) ERT calibration, and (d) ERTec calibration. Colored crosses shown in the subplot (b) are the predicted ECa values obtained from VES measurements.

SE-VCP-s50, the VES curves (red curves in figure 4.11a, g, and h) show large predicted ECa values against smaller measured ECa values. Moreover, the R^2 values of these three coil configurations are smaller than all the other VES curves indicating the reduced linear-regression fittings. The smallest R^2 was returned by ME-VCP-s32 having the smallest DOI. For the coil configurations with large DOIs, VES curves show good agreements with ERT and ERTec

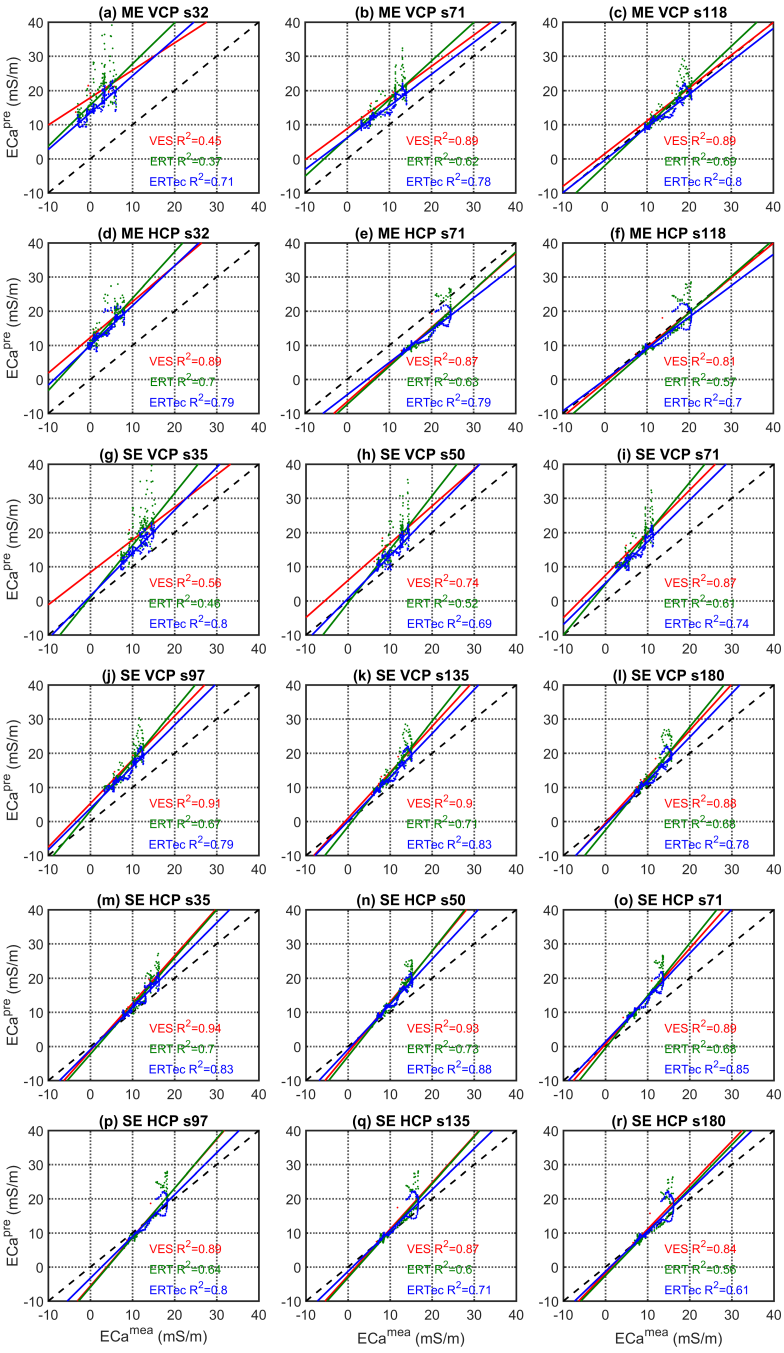

Figure 4.11: Linear regression curves of the calibration using VES (red), ERT (green), and ERTec (blue) based measurements together with the 1:1 reference line (black, dashed) for each coil configuration.

curves, and the increased R^2 values, which are higher than the other two methods, indicate the improved performance for the larger coil separations. The VES based calibration shows merit for calibrating the Tx-Rx configurations with large DOIs while it returned deviations for the small DOI configurations. This indicates that the VES measurements for the shallow depth is possibly biased by external factors such as the fertilization or the electrodes. Because of the time efficiency (about 1 h for six VES measurements in comparison to 3 h for one ERT measurement), the VES based calibration is a promising approach especially for EMI systems with large DOIs (> 0.5 m).

Regarding the ERT calibration approach without any electrode correction (green curves in figure 4.11), small R^2 values were returned for all the configurations in comparison with the ERTec results which are possibly due to the sharp-inversion algorithm. As a consequence, highly scattered points with large ECa values were obtained which are specifically visible for the small DOI (figure 4.11a, b, d, g, and h) resulting an increased difficulty of finding the best linear-regression curve. In contrast, more concentrated ECa points were obtained from ERTec due to the more gentle- and smooth-layered subsurface as shown in figure 4.6. Moreover, because it minimizes the effects of the upper layer observed from VES and ERT data, the linear-regression curves returned improved fittings for the small DOI-configurations like ME-VCP-s32, and SE-VCP-s35.

In general, most of the regression curves are not overlying the 1:1 line clearly showing that a calibration is necessary. Moreover, the VES, ERT and ERTec results show good agreements with each other indicated by similar regression curves. Different calibration methods can be selected depending on different measurement criteria, e.g., the required measurement time, the available equipment, the expected contrasts in the layering of the subsurface, and etc.

4.8 Calibrated Data Comparisons between MECI and the Three Verification Methods

By applying the calibration parameters obtained from the 2- and 3-layer MECI method at two CPs (CP18 and CP33), four independently calibrated data sets of the transect were obtained and are presented in figure 4.12 where each configuration is plotted separately. The

Table 4.2: Multiplicative (MF (-)) and additive (AF (mS/m)) calibration parameters obtained from VES, ERT, ERTec (with electrode correction), and 2-/3-layer MECI method at CP18 and CP33

	MF,AF	MF,AF	MF,AF	MF,AF,	MF,AF	MF,AF
	ME-VCP			ME-HCP		
	s32	s71	s118	s32	s71	s118
VES	0.8, 17.9	0.9, 8.8	1.0, 1.5	1.0, 12.3	1.1, -6.5	1.0, -0.8
ERT	1.2, 15.7,	1.1, 6.1,	1.2, -2.0,	1.4, 10.3,	1.1, -7.3,	1.1, -1.9,
ERTec	1.1, 13.5	0.9, 6.1	1.0, -0.3	1.2, 10.0	0.9, -4.5	0.9, -0.1
MECI18-2	0.9, 12.7	1.0, 6.5	1.0, 0.3	1.2, 15.4	1.0, -5.0	0.9, 0.7
MECI18-3	1.0, 14.7	1.1, 7.5	1.1, 0.5	1.4, 17.9	1.1, -5.0	1.1, 1.0
MECI33-2	0.9, 13.9	1.0, 7.4	1.0, 1.7	1.1, 14.4	1.1, -4.0	1.1, 2.8
MECI33-3	1.0, 14.5	1.1, 7.5	1.1, 1.3	1.1, 15.0	1.2, -5.0	1.1, 2.0
	SE-VCP					
	s35	s50	s71	s97	s135	s180
VES	1.0, 8.3	1.1, 6.0	1.2, 7.5	1.3, 5.3	1.3, 0.9	1.4, -0.4
ERT	1.5, 1.0	1.6, -0.6	1.5, 4.9	1.5, 3.1	1.5, -1.5	1.5, -2.5
ERTec	1.3, 1.4	1.3, 0.7	1.2, 5.2	1.2, 3.9	1.3, 0.1	1.3, -0.9
MECI18-2	1.0, 1.0	1.1, 0.8	1.2, 4.3	1.3, 3.2	1.3, 0.0	1.3, -0.5
MECI18-3	1.1, 1.2	1.3, 1.0	1.4, 5.0	1.5, 3.8	1.5, 0.2	1.5, -0.4
MECI33-2	1.1, 1.5	1.2, 1.4	1.4, 5.5	1.4, 5.0	1.4, 1.6	1.4, 1.4
MECI33-3	1.2, 1.5	1.3, 1.2	1.4, 5.5	1.5, 4.9	1.5, 1.1	1.4, 0.8
	SE-HCP					
	s35	s50	s71	s97	s135	s180
VES	1.4, -1.3	1.5, -1.9	1.4, 0.6	1.4, -5.6	1.4, -2.6	1.3, -1.8
ERT	1.4, -2.3	1.5, -2.9	1.5, -0.5	1.5, -5.9	1.4, -3.1	1.3, -2.5
ERTec	1.2, -1.0	1.3, -0.9	1.3, 1.4	1.2, -3.3	1.2, -1.3	1.2, -1.3
MECI18-2	1.1, 0.9	1.3, 0.7	1.4, 1.9	1.6, -5.2	1.2, -0.1	1.0, 0.7
MECI18-3	1.3, 1.1	1.4, 0.9	1.6, 2.3	1.8, -5.9	1.4, 0.1	1.3, 0.9
MECI33-2	1.4, 1.6	1.5, 1.4	1.5, 3.4	1.6, -2.9	1.4, 2.3	1.3, 2.9
MECI33-3	1.5, 1.4	1.6, 1.0	1.6, 2.9	1.7, -4.1	1.4, 1.4	1.3, 2.5

measured ECa values, the predicted ECa from VES measurement, and the calibrated ECa data using the VES, ERT, and ERTec approaches (as shown in figure 4.10) are also plotted together with the MECI results for comparison. In addition, the calibration parameters of all the seven data sets are presented in table 4.2.

It is observed that calibrated results from all calibration approaches (Figure 4.12, colored solid and dashed curves) returned large ECa values with respect to the uncalibrated measured data (Figure 4.12, black curves) for the configurations with small DOIs. Small ECa deviations

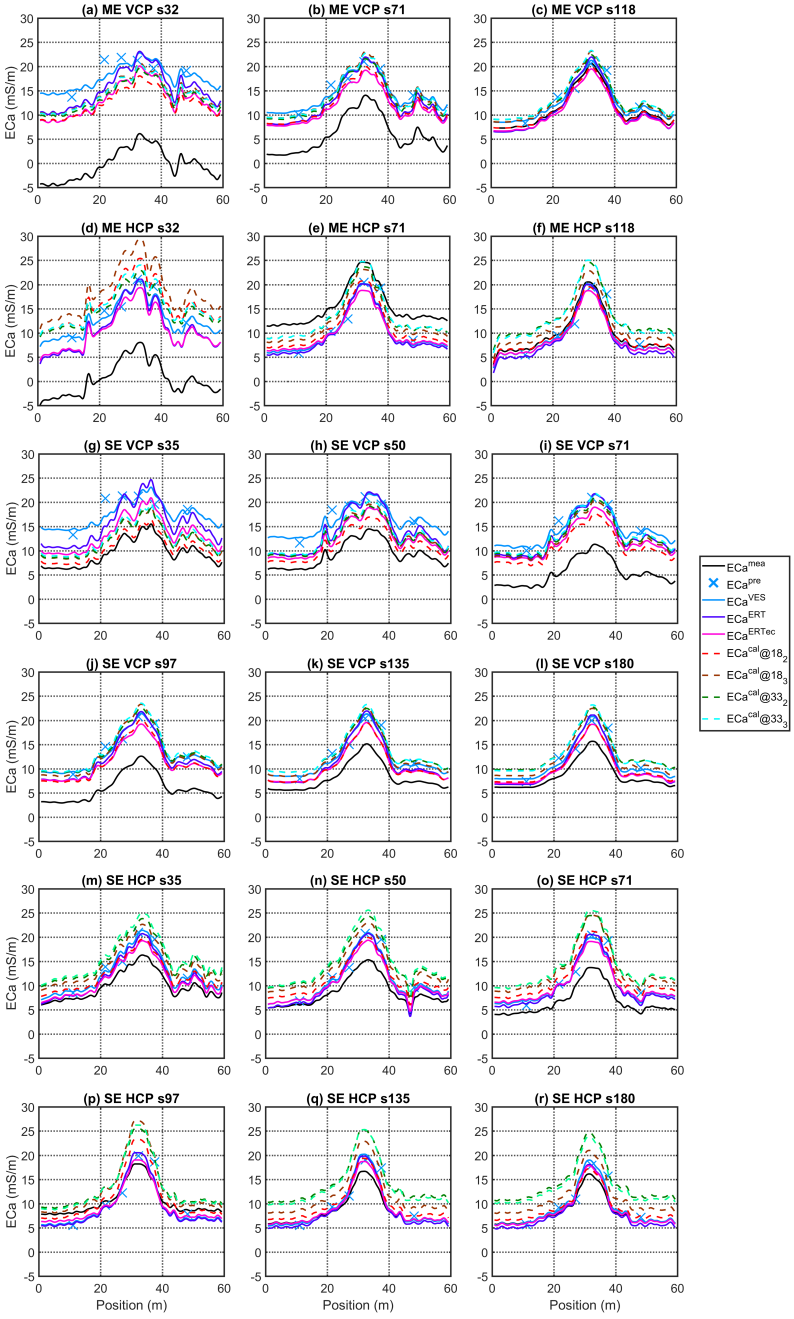

Figure 4.12: EMI data of the transect include the measured (uncalibrated, solid black curves) data, predicted data from VES measurements (blue crosses), calibrated data based on VES method (solid blue curves), ERT method (solid purple curves), ERTec method (solid magenta curves), 2/3-layer MECI method from CP18 (dashed red/yellow curves), and 2/3-layer MECI method from CP33 (dashed green/cyan curves).

Table 4.3: The mean absolute deviations between the mean calibrated ECa from all the calibration methods and the uncalibrated (measured) ECa (black curves in figure 4.12), and the mean value of the standard deviation obtained from all the calibration methods as shown in figure 4.12.

	ME-VCP			ME-HCP		
Tx-Rx Configuration	s32	s71	s118	s32	s71	s118
Deviation (mS/m)	14.7	7.2	0.8	13.7	3.9	0.8
STD (mS/m)	1.8	1.0	1.2	2.9	1.6	2.0
	SE-VCP					
Tx-Rx Configuration	s35	s50	s71	s97	s135	s180
Deviation (mS/m)	3.9	4.0	7.2	6.6	3.6	2.9
STD (mS/m)	2.4	1.6	1.2	1.1	1.1	1.3
	SE-HCP					
Tx-Rx Configuration	s35	s50	s71	s97	s135	s180
Deviation (mS/m)	3.3	3.6	5.0	1.1	2.3	2.2
STD (mS/m)	1.3	1.8	1.9	2.0	2.3	2.5

were observed for large DOI configurations. Similar observations were made by von Hebel (2016), who calibrated the same EMI measurement setups. However, the results investigated in chapter 3 show relatively large variations for the large DOI configurations which is in contrast to the results shown in figure 4.12. These differences are probably due to the different measurement setup used in chapter 3 which influences the shift of the measured ECa values, e.g., the use of a sled instead of a crutch, the different position of the data logger, and the use of the GPS system. Therefore, different measurement setups need to be calibrated separately.

The mean absolute deviations (table 4.3, the row of deviation), which are calculated by subtracting the mean calibrated ECa data from the mean uncalibrated data, returned large deviations varying between 0.8 (at ME-VCP-s118 and ME-HCP s118) and 14.7 mS/m (at ME-VCP-s32). In contrast, the mean standard deviations (table 4.3, the row of STD), which were obtained by averaging over all of the seven sets of calibrated ECa values, returned small values from 1.0 (at ME-VCP-s71) to 2.9 mS/m (at ME-HCP-s32). The comparisons between these two data sets (the STD and the deviation) indicate that the erroneous shifts in the measurement data are more significant than the small variations between each calibration method (also indicated by the similar calibration parameters shown in table 4.2).

When looking at the MECI results, the calibrated ECa values obtained from the 3-layer MECI at CP33 (figure 4.12, dashed cyan curves) show good agreements with the 2-layer MECI

results at the same CP (figure 4.12, dashed green curves), whereas CP18 shows slight deviations of up to about 3 mS/m (figure 4.12, dashed red and brown curves). When comparing the two CPs, good agreements were returned for the DOI configurations such as ME-VCP-s32 to -s118, and SE-VCP-s71 to -s180 showing differences smaller than 1 mS/m. These small differences are also visible from the calibration parameters (table 4.2). However, larger variations were observed for the configurations ME-HCP-s32, SE-VCP-s35, and SE-HCP-s50 to -s180 with differences of up to about 9 mS/m. These deviations indicate different calibration performances at the two different CPs which might be due to different heterogeneities. The observation made in chapter 3 shows that the MECI method performs better at the CP above a relative homogeneous subsurface with less layers and small electrical conductivity variations. To investigate whether this is also the case for the current study, the calibration results obtained from the three verification methods are plotted in figure 4.12 to compare with the MECI results.

In general, the 2-layer MECI at CP18 returned the most similar ECa values compared with all the three verification methods, whereas the 3-layer CP18, and 2-/3-layer CP33 results reveals differences especially for the configurations with large DOIs such as SE-HCP-s71 to -s180. Nevertheless, deviations are observed from the 2-layer CP18 for the configurations ME-VCP-s32, ME-HCP-s32, SE-VCP-s35 and -s50. To investigate whether these variations show a relationship with respect to the DOI of each configuration, the mean values of the absolute misfit between MECI and the three verification approaches are plotted in figure 4.13a to c for VES, ERT, and ERTec, respectively. In addition, cross comparisons presented as the absolute misfits between VES, ERT and ERTec were also obtained (figure 4.13d). Note that the misfits in figure 4.13 are plotted against the DOI index (presented in table 4.1) which is ordered from shallow to deeper depths.

By observing all the misfit curves shown in figure 4.13, three groups of DOI were categorized including indices 1 to 5, 6 to 10, and 11 to 18, respectively. Each of the groups contains different behaviors to the other groups but show common relationships across all the misfit subplots.

Because the misfits of the verification methods (figure 4.13d) returned bigger values for the small DOI group containing indices 1 to 5 than the other groups, the misfit curves of MECI

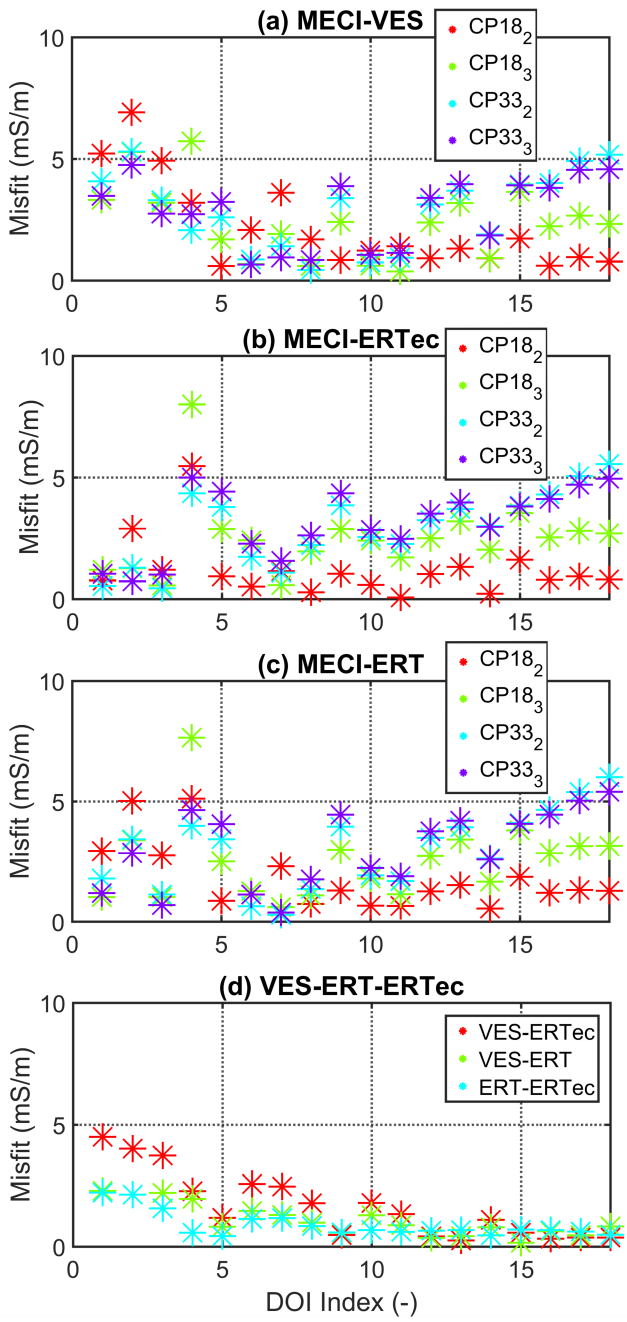

Figure 4.13: Mean values of the absolute ECa differences between (a) MECI and VES, (b) MECI and ERT, and (c) MECI and ERTec methods against the DOI index. In addition, misfits between the three reference calibration methods (VES, ERT and ERTec) are plotted in figure (d). The configuration for each DOI index is presented in table 4.1.

versus different verification methods (figure 4.13a to c) behave differently/randomly, and show relatively large misfit values. This result points again to the deviations of calibrated results for the shallow depth obtained from the three electrode-based measurements as discussed in section 4.7. Among these results, the MECI and ERTec results returned the smallest misfit value indicating the best agreement. In particular, the misfit of the first three DOIs show values below 3 mS/m although DOI-4 returned increased values from 4.5 to 8 mS/m.

As the misfits for the middle DOI group (DOI indices 6 to 10) decreased (figure 4.13d), the deviations between the MECI and each verification method returned smaller values than the group with small DOIs. The misfit curves for this group also show similarities between each other (figure 4.13a to c). This result indicates a stable MECI calibration for the configurations having the DOI value from 0.53 to 0.85 m.

When the DOI index is further increased from 11 to 18, the misfits between the three verification methods show stable and small values below 1 mS/m. Meanwhile, the misfits of 2- and 3-layer MECI at CP33 increase again returning the maximum value of about 5.6 mS/m at DOI-18 (SE-HCP-s180, 3-layer). This can be explained by the reduced sensitivity of the MECI method for the deep depth (>2 m) below the paleo-river channel, where a low conductive layer is located (visible in figures 4.6 and 4.7). In contrast, the 2- and 3-layer MECI at CP18 returned relatively stable misfit curves, among which the most stable result was obtained from the 2-layer CP18 result showing values below 2 mS/m. This small misfit is similar to the observation from figure 4.12 showing the smallest ECa difference between the 2-layer MECI at CP18 and the verification results. Last but not least, the MECI method shows a merit especially for calibrating the configurations with small DOI since no galvanic coupling is needed and therefore no electrode effects can complicate the measurements.

In general, results from CP18 show better agreements with the three verification results than CP33 indicating a better calibration performance from the more homogeneous location. To further validate the result, inversions of the complete transect were performed using different calibrated data from the two CPs.

4.9 Inversion Results of the Transect

4.9.1 2-layer Inversion

The inverted 2-layer electrical conductivity distributions of the transect were obtained using the measured (uncalibrated) ECa (figure 4.14c), the calibrated ECa based on the VES calibration (figure 4.14d), the ERT calibration (figure 4.14e), the ERTec calibration (figure 4.14f), and the 2-layer MECI at CP33 (figure 4.14g), and CP18 (figure 4.14h). During the transect inversion process, the ECa values were obtained by using a non-linear exact ECa conversion (EEC) algorithm (von Hebel, 2016) which resolves more accurate ECa values for the zero elevation EMI data sets in comparison to the LIN-based conversion method (equation 3.6). For comparison purposes, the subsurface images combining the 30 and 60 m data from the ERT inversion (figure 4.5b and b) and the ERTec inversion (figure 4.6a and b) are presented in figure 4.14a and b, respectively.

The inversion result from uncalibrated data (figure 4.14c) shows values approaching 0.1 mS/m (the boundary limit of the inversion) for the homogeneous regions (the first and last 20 m of the transect line) as well as the upper layer of the heterogeneous region (from about 20 to 40 m). This is due to the measured negative ECa values from the small DOI configurations which cannot be modeled. Moreover, the misfit of the inversion (4.14i) shows significant large values of up to 1500% indicating the difficulty in finding a global minimum for uncalibrated data with negative values. Despite this, the paleo-river channel is visible which is probably due to less erroneous shifts for larger DOI configurations. As a result, the inversion using the uncalibrated data is only able to return a qualitative electrical conductivity distribution of the subsurface. For quantitative subsurface investigations, calibration is necessary.

The inverted models from the VES- and ERT-calibrated EMI data (figure 4.14d, and e) returned a highly conductive upper layer with σ values of about 30 mS/m and thicknesses from 0.1 to 0.25 m. For this thin layer the ERTec-calibrated inversion (figure 4.9.1f) returned smaller value (of about 15 mS/m) showing the similar σ range to the MECI results (figure 4.14g and h). This discrepancy between VES/ERT and ERTec/MECI data is because of the large calibrated ECa values from configurations ME-VCP-s32, and SE-VCP-s35/50/71 (as indicated in figure 4.12a, and g to i) in comparison with the corresponding ERTec and

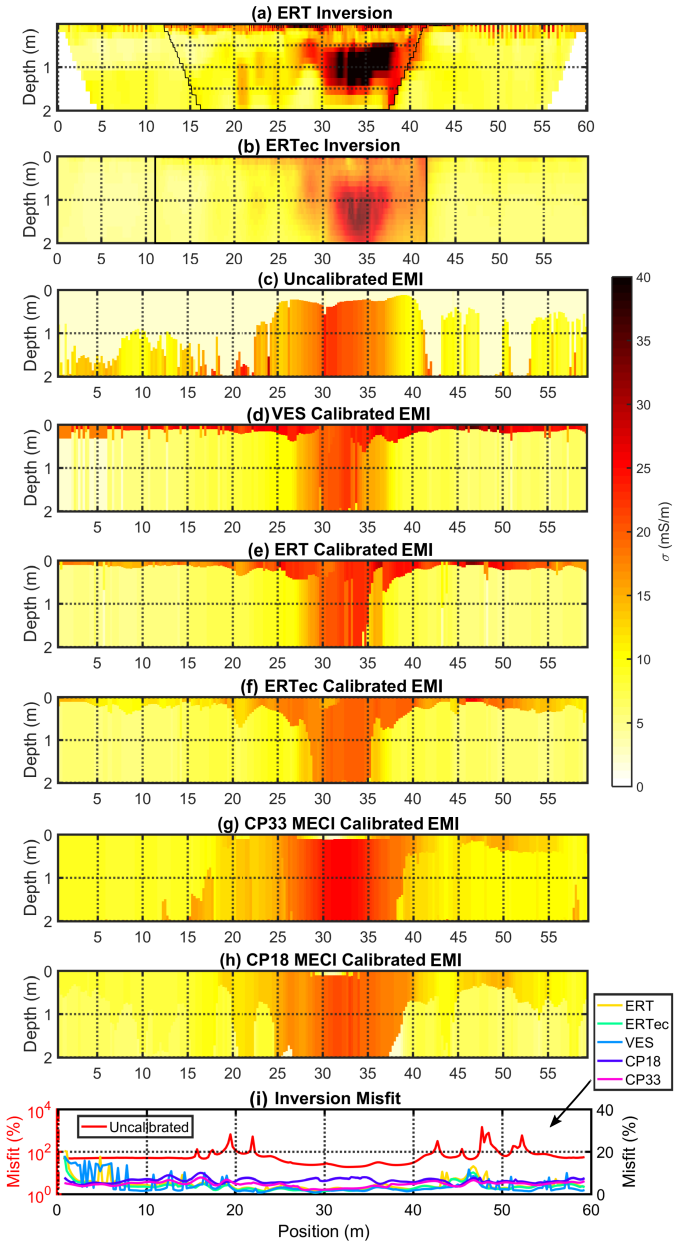

Figure 4.14: Subsurface electrical conductivity distribution models of the transect obtained from (a) ERT inversion (figure 4.5), (b) ERTec inversion (figure 4.6). The 2-layer EMI inversion using (c) the measured (uncalibrated) EMI data, the calibrated EMI data obtained from (d)VES, (e) ERT, (f) ERTec, and the 2-layer MECI method at (g) CP33 and (h) CP18. For comparison purposes, the corresponding inversion misfits (i) are presented for uncalibrated results (left axis) and three calibrated results (right axis). Note that the subplot (a) shows the overlapping image of ERT-30 and ERT-60 (figure 4.5a on top of figure 4.5b), and the subplot (b) shows the overlapping image of ERTec-30 and ERTec-60 (figure 4.6a on top of figure 4.6b).

MECI results. One explanation is that the electrode effects resulted in higher measured ECa values for VES and ERT measurements whereas the ERTec minimized this effect by the corresponding electrode correction. In addition, it is also possible that due to the agricultural activities, e.g., fertilization, plowing, and plant growing, or the overnight raining, the ion concentration and soil moisture of the shallow subsurface were changed, to which the galvanic coupling based ERT approach is more sensitive than the EMI method. However, these possible causes require further and detailed investigations on each influencing factor. Last but not least, similar results were obtained from all the four data sets returning σ values of about 5 to 10 mS/m for the lower layer at the homogeneous regions, and the relative high σ values of about 25 to 30 mS/m at the heterogeneous region (20 to 40 m).

For the VES, ERT and ERTec inverted data, the sloping boundaries of the paleo-river channel are visible from the shallow subsurface (from a depth of about 0.2 to 0.8 m) but are narrowed down as the depth increasing. In general the inverted results from the three verification methods show good agreements with the subsurface models directly inverted from the ERT and ERTec inversion data (figure 4.14a and b), but return less details due to the 2-layer inversion. Furthermore, these boundaries are clearly visible from the MECI CP33 and CP18 inversion, from which the CP18 result returned the best agreement with the subsurface models (figure 4.14a and b) indicating that MECI works better at the calibration position with a relatively homogeneous subsurface which matches to the investigations discussed in chapter 3.

Nevertheless, it is noticed that all the inversion results using the EMI data (figure 4.14d to h) returned a slightly shifted position of the paleo-river channel in comparison with the ERT inversion (figure 4.14a and b). This position shift is approximately 2 m to the left side of the transect. In order to find out the reason, the predicted ECa values from ERTec 30 m and 60 m data for all configurations are plotted in figure 4.15a (the same data as shown in figure 4.10d). The reason to use ERTec here instead of ERT is because the ERTec data returned more smoothed ECa values than ERT data such that the trends with peaks are clearly visible. For comparison, figure 4.15b shows the calibrated ECa values from MECI CP18. Note that this MECI CP18 result is the same as the data shown in figure 4.12, but configurations are plotted together for better illustration.

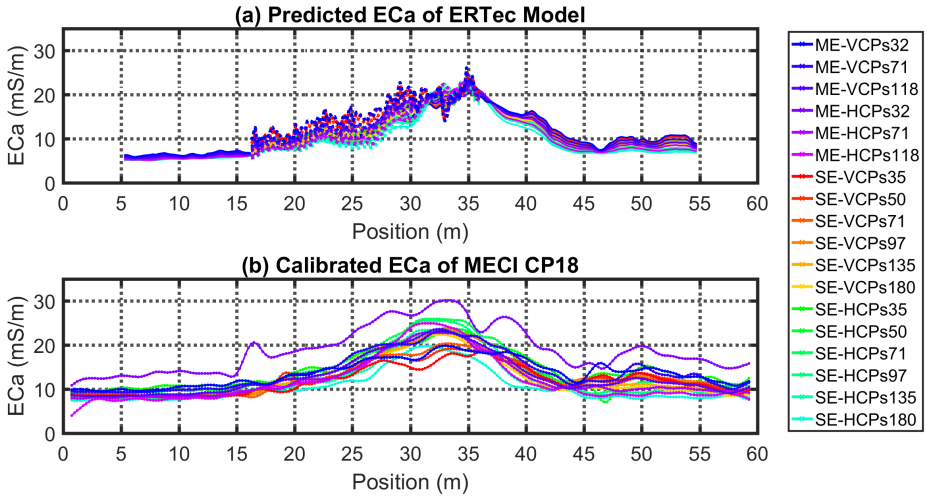

Figure 4.15: (a) Predicted ECa value obtained from 30 m ERTec data (dashed color lines) and 60 m data (solid color lines). Note that the first and last 5 m of both two ERTec data was cut due to the lack of the sensitivity of the ERT measurement. (b) Calibrated ECa value obtained from MECI CP18 data.

The peak values of the predicted ECa from ERTec (figure 4.15a) are clearly visible for all configurations returning a similar peak position at around 35 m. In contrast, the calibrated ECa of the MECI returned different peak values with a range from 31 to 33 m. For those configurations with small DOI such as VCP-s32, s71, HCP-s32, the peak values occur at around 33 m, whereas configurations such as HCP-s71 to s180 show positions at around 31 m. To further investigate the relationship between shifted locations of EMI data and the DOI (based on table 4.1), figure 4.16 is showing peak positions of all configurations. This clearly shows a decreasing trend of the peak position with increasing DOI. Note that two peaks were observed from DOI-2 at position 33.5 and 36.25 m, respectively, returning a small ECa difference of 0.55 mS/m. Because the position 33.5 m is close to the peak positions of the neighboring DOI indexes, it is selected resulting in a smooth curve. The peak position in figure 4.16 varies by the maximum value of about 2 m and shows a strong correlation between the measured position and the DOI.

Because the GPS is mounted in the middle of the EMI measurement setup, each configuration has a different relative distance to the midpoint resulting in a position shift of up to about 0.8 m (SE-s180). Nevertheless, the decreasing trends are still visible after correcting

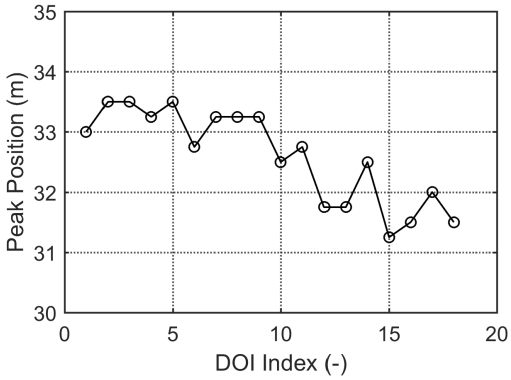

Figure 4.16: Locations of the peak ECa values obtained from MECI CP18 data for 18 EMI configurations. Each configuration is presented as the DOI index (shown in table 4.1) with the order of increasing DOI.

these position shifts. These results indicate that the DOI related position shifts might be due to either the measurement setup or the electrical distribution of the subsurface, and requires further investigation.

According to the discussion of the shifted data positions between ERT and EMI inverted models, it is clear that the accuracy of the ERT-based calibration is related to the accuracy of the georeferencing. Moreover, this discussion points to the feasibility of MECI because the calibration parameters from MECI are independent of the EMI transect measurement.

4.10 3-layer Inversion

Although the misfits plots shown in figure 4.13 indicate larger misfits values of 3-layer than 2-layer MECI when comparing with the VES and ERTec results, it is still interesting to analyze the 3-layer inversion results of the transect to fully understand the process of the calibration, and to find out possible solutions for improvements. Consequently, the calibrated EMI data obtained from 3-layer MECI at both CP18 and CP33 are inverted for a 3-layer model using a similar inversion procedure as the 2-layer inversion. The MECI based results are plotted together with the 3-layer inverted models from the uncalibrated, VES calibrated, ERT calibrated and ERTec calibrated data sets for comparison purposes (figure 4.17).

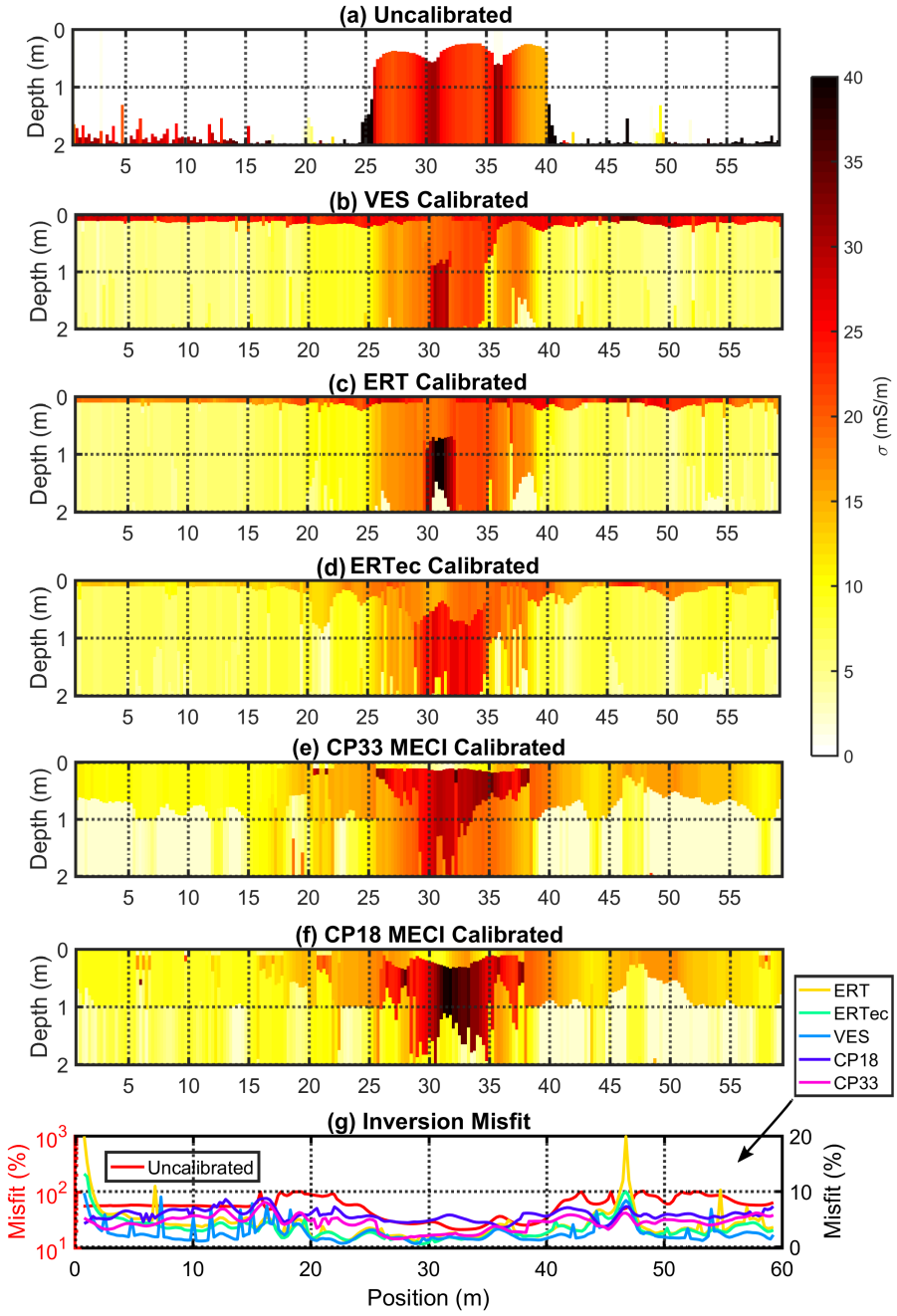

Figure 4.17: Inverted 3-layer subsurface models of the transect using (a) the measured (uncalibrated) EMI data, the calibrated data obtained from (b) VES, (c) ERT, (d) ERTec, and the 3-layer MECI methods at (e) CP33 and (f) CP18, as well as the corresponding (g) inversion misfits presented in percentage.

As expected, the uncalibrated data returned erroneous inverted models (figure 4.17a), whereas inversion results using VES, ERT, ERTec calibrated EMI data (figure 4.17b to d) returned similar but more detailed results with respect to the corresponding 2-layer models (figure 4.14d to f). For the MECI results, similar observations are returned for the heterogeneous area (from 20 to 40 m of the transect) showing more detailed electrical conductivity distributions. Relatively homogeneous regions were obtained for the first 20 m of the transect from both two CPs (figure 4.17e and f) returning σ from 5 to 10 mS/m, whereas, an upper layer with the thickness of about 1 m depth was returned showing σ of about 18 mS/m for the last 20 m of the transect. For the lower layer at the corresponding areas, both MECI based results returned the small electrical conductivity values below 5 mS/m. For these clearly layered soil structures the results are different compared to the 2-layer inversion results (figure 4.14g and h) which show more homogeneous results but with higher electrical conductivity values.

One possible reason for the differences between 2- and 3-layer MECI inversion results is that the information provided by the ECa value, i.e., the calibrated EMI data from 3-layer MECI, contains non-uniqueness for a 3-layer inversion, such that the inversion is trapped within a local minimum value. This information might also be due to the local-minimum during the calibration procedure using the data obtained from the multi-elevation. Under a noisy measurement environment, the data collected from the muti-elevation measurement, especially from small DOIs with reduced sensitivities to the deeper depth, may not provide enough information for the 3-layer MECI to reach the global minimum. To improve the results, one possible solution is to add an derivative-based inversion algorithm such as Gauss-Newton method to define more precise boundary conditions before for the SCE inversion. Both synthetic and experimental investigations are still necessary in the further study.

4.11 Conclusion

As extended field verifications, the current chapter presented experimental investigations using the multi-elevation calibration and inversion (MECI) approach to calibrate two EMI operated-sleds including DGPS for large-scale measurements. Three electrode-based calibration methods, i.e., VES, ERT, and ERTec, were implemented in order to verify the MECI

Table 4.4: Overview of calibration methods

Method	Calibration Misfit (%) (figure 4.8)	Calibration Fitting (R^2) (figure 4.11)	Transect Inversion Misfit (%) (figure 4.14, 4.17)	Number of Measurement Points	Measurement Duration (hour)	Inversion Algorithm
VES	-	0.83	4±4	6 locations	1.5	3-layer SCE
ERT_{30}	-	0.62	2-layer: 4±3 3-layer: 4±3	120 electrodes	3	Robust L1-Norm
$ERTec_{30}$	-	0.77	2-layer: 4±2 3-layer: 3±2	120 electrodes	3	Smooth-constraint, electrode correction
$MECI\text{-}CP18_2$	3	-	6±1	7 elevations	1	2-layer SCE
$MECI\text{-}CP18_3$	3	-	6±1	7 elevations	1	3-layer SCE
$MECI\text{-}CP33_2$	2	-	5±1	7 elevations	1	2-layer SCE
$MECI\text{-}CP33_3$	2	-	4±1	7 elevations	1	3-layer SCE

method. An overview of all the calibration methods is shown in table 4.4, summarizing the calibration fittings, inversion misfits, number of measurement points for calibrating measured EMI data, measurement durations, and the inversion algorithm used.

In general, the calibrated results returned larger ECa deviations for the Tx-Rx configuration with small DOIs in comparison with small deviations for the large DOI configurations. When comparing these deviations with the results shown in chapter 3 using different measurement setups, an opposite trend is returned indicating that different measurement setups for the same EMI device can lead to different ECa shifts. Therefore, calibrations need to be performed separately for each measurement setup.

All the calibration results show reasonably good agreements with each other, and indicated that the calibration is necessary. The VES based calibration shows merit for calibrating the Tx-Rx configurations with large DOIs while it returned deviations for the small DOI configurations. ERT-based measurements return a high-resolution subsurface inversion result but are more elaborate. The time needed for the MECI method was about 1 h per calibration position, and is similar to the VES method but less than the ERT method (about 2 to 3 h). Different calibration methods can be selected depending on different measurement criteria.

The MECI calibration performed at the homogeneous position CP18 of the transect shows the most similar inverted subsurface in comparison with the three verification results, whereas the results from the heterogeneous position CP33, i.e., the position above the paleo-river channel, return higher conductivity values over the whole transect. These results are consistent with chapter 3. This shows that a homogeneous low conductive subsurface seems

more appropriate for MECI based calibration of the EMI measurement setup used in this study.

The shifted positions between ERT and EMI measurement tracks of the transect indicate that a position compensation needs to be applied according to the DOI of each EMI configuration. Moreover, this also shows the merit of using MECI from which the calibration parameters are obtained independent to the EMI transect measurements such that the accuracy of the transect position track has no influence on the calibration.

Instead of using the plastic boxes to elevate the EMI measurement setup, a suitable calibration setup will be developed in the future that allows faster and more accurate EMI elevation measurements. Overall, experimental results in this chapter indicate that MECI is a promising non-destructive approach as a replacement for the conventional electrode-based calibration.

5. Conclusions and Outlook

EMI systems have been increasingly used during the last decades for subsurface electrical conductivity surveys, while literature studies have shown the challenges of such systems to acquire quantitative data. This thesis was set out to improve the performance of electromagnetic induction (EMI) systems towards providing quantitative and stable data for geophysical subsurface investigations. To answer the two questions raised in chapter 1 which are (1) "What prevents the EMI system from producing temperature independent measurements, and how to correct the corresponding drifts?", and (2) "Are EMI systems able to obtain quantitative measurement data values without using additional instruments?", detailed investigations of EMI were carried out including theoretical analyses, developments of drift correction and calibration methods, corresponding synthetic model simulations, and experimental verifications.

5.1 Obtaining Temperature Independent Measurement Data

In order to obtain stable measurement results without drifts due to ambient temperature changes, chapter 2 was set out to explore a custom-made EMI system from the circuit design point of view and to analyze the thermal effects of its internal electronics. Consequently, a novel temperature correction method was developed and was verified by testing in different measurement environments.

5.1.1 Temperature Drift Correction Method

The temperature induced drifts are related to the thermal status of the internal electronics. However, different electronics react differently to the ambient temperature resulting in a complex drift behavior of the output signal. To monitor the drifts coming from the central circuit of the EMI system, i.e., the coil and its surrounding electronics, a transfer function analyzer (TFA) was developed which measures the transient responses of the circuit by sending series of short-period DC signals. Consequently, the transient signals were processed into ECa values, which represent the thermal drifts coming from the central circuit, and were subtracted from the measured ECa values.

To avoid disturbances between the TFA and transmitter signals, the TFA and ECa measurements were performed separately in between with each other. During one TFA measurement, one-hundred transient signals were obtained within 1 s and were averaged to increase the signal-to-noise ratio. In addition, ambient temperature sensors (ATS) were used to estimate the thermal status of the electronics in the read-out circuit such as amplifiers which react fast to the ambient temperature. Consequently, the complete temperature correction method contains the TFA and ATS.

5.1.2 Verifications

As a preliminary investigation, the TFA was applied to the receiver unit while keeping the transmitter under a temperature stable condition. Experimental verifications were carried out including a manually temperature controlled measurement and two case studies representing two different ambient environments. In addition to the TFA-ATS method, the temperature correction using either TFA or ATS was also performed for comparison purposes. With temperature changes of up to about 12 °C, the ECa value without any correction returned the RMSE value of up to 80 mS/m. The TFA-only and ATS-only methods also returned large RMSE values of up to 24.9 and 10.2 mS/m, respectively, indicating that the combination of TFA and ATS is necessary for the correction. As expected, the TFA-ATS method returned small RMSE values of up to 2.3 mS/m. This small RMSE value from the TFA-ATS method indicates a good performance, and is close to the designed system accuracy of about 1 mS/m. Nevertheless, the TFA-ATS method returned different regression coefficients for the two ATS

from different measurements. This indicates that the ATS needs to be calibrated prior to each EMI survey, which might be time-consuming and elaborate. Further study is needed to understand this behavior. A promising direction is to add a TFA to the transmitter unit because it also showed a temperature dependency during the experimental investigations.

5.1.3 Highlights

Temperature stabilized measurements are realized by implementing the TFA into the EMI receiver circuit together with the ambient temperature sensors. Regarding this novel temperature correction approach, some features are summarized below:

1. The thermal effect of each receiver unit can be monitored individually providing phase corrections for each system circuit.

2. The thermal energy remaining in the inner system due to historical heating/cooling procedures can be traced by TFA whereas temperature sensors only measure the instantaneous ambient temperature.

3. Coils can be used close to their resonance frequency at which the coil has the largest sensitivity of both electromagnetic induction and phase drifts, whereas the latter can be fully compensated by the TFA.

Both manually temperature controlled and realistic experimental analyses indicate that the proposed correction method is a promising tool to trace and correct the phase drifts originated by the thermal changes of the internal electrical components due to the ambient conditions. The method can be used to correct the phase drifts of a multi-receiver unit where each receiver unit is monitored individually.

5.2 Obtaining Quantitative ECa Values without Using Additional Instruments

In order to achieve a calibration without the help of any other instrument, sufficient information need to be gathered to find out the constant shifts which bias the EMI measurement

data. Consequently, the idea of measuring at multiple elevations above the ground surface was implemented and was verified by simulations and experimental investigations.

5.2.1 Multi-elevation Calibration and Inversion (MECI) Method

Chapter 3 presented a novel multi-elevation calibration and inversion (MECI) approach for calibrating commercial EMI systems. This method uses EMI data obtained at multiple elevations above the ground surface such that no additional instrument is required to calibrate the EMI data. The MECI method returns multiplicative and additive calibration factors for the measured ECa for each Tx-Rx configuration as well as a 2-/3-layer subsurface model of the corresponding calibration position.

This method is based on a 1D electromagnetic forward modeling as well as the shuffled complex evolution (SCE) inversion algorithm to achieve the objective of calibrating the system together with the inversion of the soil subsurface. With the help of the Jacobian sensitivity matrix, the minimum number of elevations was determined in order to optimize the measurement time and effort. Moreover, no regularization or weighting was applied during the inversion of electrical conductivities and layer thicknesses, which is particularly useful for agricultural sites where a shallow plowing layer is present resulting in a clear and sharp layer interface.

5.2.2 Synthetic and Experimental Verifications for a Hand-held EMI Instrument

First, MECI was tested using simulations for both noise-free and noisy conditions. The results from homogeneous, 2-layer, and 3-layer subsurface models together with artificial calibration parameters returned good reconstructions of the input models indicating the capability of this algorithm.

Then, the experimental test was performed on a 30 m long transect of a bare-soil test field which has an average electrical conductivity range from 5 to 30 mS/m. The differences between the calibrated and uncalibrated ECa data returned the values from 2 to 10 mS/m indicating that the calibration is necessary in order to obtain quantitative measurement data.

Such shifts were also observed from a vertical electrical sounding (VES) based calibration method which was implemented as a verification result. The MECI calibrated results from five individual calibration positions returned similar values with the maximum mean standard deviation of 0.37 mS/m indicating the stability of the this approach. The MECI method was further validated after the inversion of a test transect showing a similar electrical distribution with the results from VES based data. Moreover, a shallow plow layer could be resolved from MECI data probably due to the higher sensitivity for the shallow subsurface.

5.2.3 MECI for Sled-based EMI Field Applications

Based on the findings from chapter 3, further investigations have been carried out in chapter 4 to evaluate the capability of calibrating the EMI measurement setup that is designed for large-scale surveys. Instead of the bare-soil test field, which was used for the preliminary verifications in chapter 3, field application measurements were performed on an agricultural field whose soil property is dominated by sand and gravel sediments with electrical conductivity values from 5 to 40 mS/m. The differences of the calibration results obtained from chapter 4 in comparison with chapter 3 indicate that different EMI measurement setups lead to different calibration parameters even though the same EMI instrument is used. Therefore each EMI measurement setup needs to be calibrated individually.

The detailed comparisons between the MECI and three electrode-based methods, i.e., the VES, electrical resistivity tomography (ERT), and ERT with electrode correction, showed good agreements returning the mean standard deviations within 3 mS/m. When comparing with the more significant mean absolute deviations of up to 15 mS/m for the uncalibrated data, this small deviation (3 mS/m) indicates good performances of all the calibration methods, and especially, validates the capability of the MECI method. The VES and MECI methods are time efficient. The VES measurement took about 1.5 hours for measuring at six calibration locations, and the MECI measurement took about 1 hour for measuring at one location using two EMI instruments with two orientations for each. The VES calibration shows merit for calibrating the EMI system with large DOI while the MECI is more sensitive for the small DOI. The ERT based methods show detailed information of the subsurface, but are more time consuming taking about 3 hours for one measurement. Among the ERT methods, the one without electrode-correction returned a sharp-layered subsurface

while the ERTec revealed smoothed-layered subsurface due to different inversion algorithms and settings. Those comparisons between each calibration indicate that different calibration methods should be selected or combined depending on the different calibration requirements or the different characteristics of the subsurface. In addition, the clearly inverted paleo-river channel located under the measured transect shows the potential of using EMI together with the MECI method for quantitative underground river path reconstructions.

5.2.4 Highlights

The question "Are EMI systems able to obtain quantitative measurement data values without using additional instruments?" can be answered positively after evaluating the MECI method both theoretically and experimentally. Some highlights of this MECI approach in comparison with the conventional methods were drawn and are presented below:

1. The MECI method does not depend on additional instruments which is different from all other calibration methods presented for the portable rigid-boom single-frequency multi-separation EMI systems.

2. One single calibration position can be used for MECI indicating the merit in time efficiency which varies from 15 minutes (for the single hand-held EMI instrument with two orientations, chapter 3) to 1 hour (for the two sled-based EMI setups with two orientations for each, chapter 4) whereas the conventional electrode based methods usually take longer.

3. The complete calibration process takes full advantage of the non-invasive characteristic of the EMI technique which retains the completeness of the measurement fields.

4. When performing the calibration above a relative homogeneous subsurface with less layering contrasts, the MECI method is recommended, which returned improved calibration results than the other methods.

5.3 Outlook

The major objectives addressed at the beginning of this thesis have been accomplished accordingly. Nevertheless, some limitations were discovered during the investigations. For future developments, possible directions are summarized in this section.

The accomplishments of the presented TFA and MECI investigations enable building up a novel EMI system which provides quantitative ECa measurements by the temperature correction and the calibration of constant shifts. Because the investigations of the TFA from chapter 2 indicate possible temperature drifts from the transmitter unit, it is necessary to apply the TFA to the transmitter unit in order to improve the system stability for future EMI system developments.

Moreover, in comparison to the conventional rigid-boom EMI system, using TFA circuits to monitor transmitters/receivers separately for each unit enables building up a more flexible EMI system, e.g., a system with multiple sealed tubes which increase the transportation efficiency but have different thermal conditions. Because literature studies have shown a limited number of rigid-boom frequency domain EMI systems that provide quantitative measurement data with accuracies of about 1 mS/m, the future development of this novel EMI system shows significant potential for quantitative geophysical and agricultural applications. Last but not least, developing a 3D forward modeling algorithm (with preliminary results shown in appendix C) is a promising direction to improve the performance of subsurface reconstructions using EMI systems. It also provides potentials for further EMI system developments which might enhance the field of applications for EMI.

A. Temperature Drifts of the Amplifier

A test measurement was performed to investigate the phase drifts coming from the temperature change of the amplifiers. The Rx coil was disconnected during the measurement such that thermal effects from the coil can be avoided. Consequently, the transmitter signal was sent directly to the read-out terminal of the receiver unit using a transmitting cable. An external resistor was placed on top of the two amplifiers in the read-out circuit. The temperature of the two amplifiers was heated up by controlling the current of the external resistor.

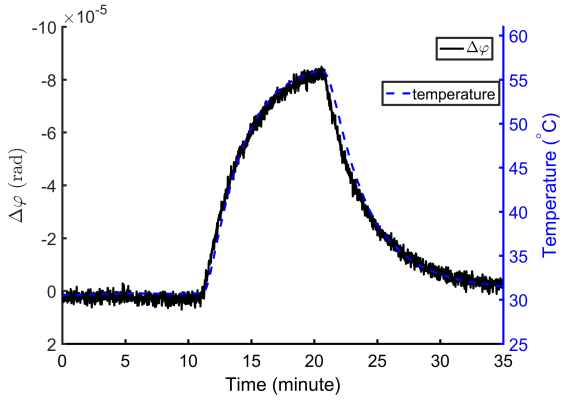

Figure A.1: The relative phase drift when heating the amplifiers in the Rx unit only. Note that the Rx coil has been removed during this measurement to avoid additional electromagnetic induction effect from the coil.

It is observed that the phase response follows the temperature instantaneously and returned a phase drift of up to about 8.2×10^{-5} rad (figure A.1) when the temperature reached

to about 55 °C. Note that these phase values are static numbers which do not include any EM effect. To get an idea of how big this phase drift can influence the ECa value, the corresponding equivalent ECa was calculated based on the system having the transmitter frequency of 15 kHz, and the Tx-Rx separation of 0.8 m. Consequently, the value of about 4.8 mS/m is returned at the phase of 8.2×10^{-5} rad. These results demonstrate that the amplifiers in the read-out circuit are one of the drift sources that can be corrected by using ambient temperature sensors.

B. Gauss-Newton Method

The current appendix introduces a calibration and inversion approach using the Gauss-Newton method which solves for the non-linear least-square problem by applying Tikhonov regularizations. In the following sections, methodology of the Gauss-Newton based approach is presented together with the analytical analyses of both noise-free and noisy synthetic simulations of 1-/2-/3-layer subsurface models.

B.1 Methodology

The Gauss-Newton based calibration and inversion method starts with defining the unknown parameter matrix as

$$\mathbf{p} = \left[\sigma_1, \cdots, \sigma_n, \mathrm{AF}_1, \cdots, \mathrm{AF}_m\right], \tag{B.1}$$

where σ is the electrical conductivity, n is the number of the soil layer, AF is the additive factor which shifts the measurement data, and m is the number of the Tx-Rx configuration. In this study, the inverted model is a 20-layer (n = 20) subsurface with a depth of up to 4 m. The thickness of each layer is pre-defined, and is increased by a factor of 1.2 times the neighboring upper layer. Note that, in comparison with the shuffle complex evolution (SCE) based method presented in chapter 3, this calibration and inversion approach does not invert for either the thickness or the multiplicative factor (MF). Therefore, the modeled ECa function is written as

$$f(\mathbf{p}) = \mathrm{ECa} + \mathrm{AF}, \tag{B.2}$$

where ECa is obtained based on equation 3.6. By defining the iteration number as i, the function of the ith iteration becomes

$$f(\mathbf{p}_i) = \mathbf{J}_i \cdot \Delta\mathbf{p} + f(\mathbf{p}_{i-1}), \tag{B.3}$$

where $\Delta p_i = (p_i - p_{i-1})$, and $f(p_{i-1})$ is obtained recursively starting with the initial value p_0. $\mathbf{J}_i$ is the Jacobian sensitivity matrix of the ith iteration by applying Δp_i to equation 3.12 and 3.15 in chapter 3, and is given by

$$\mathbf{J}_i = \begin{bmatrix} \mathbf{J}_{i,\sigma} & \mathbf{J}_{i,\mathrm{AF}} \end{bmatrix}. \tag{B.4}$$

where $\mathbf{J}_{i,\sigma}$, and $\mathbf{J}_{i,\mathrm{AF}}$ are the sensitivity matrices for the input variable σ, and AF, respectively.

The inversion minimizes the misfit between the measured and modeled ECa values using the least-square objective function given by

$$\min(||f(\mathbf{p}_i) - \mathrm{ECa}^{\mathrm{mea}}||^2 + ||L \cdot \lambda \cdot p_i||^2). \tag{B.5}$$

Note that multiple elevations are included with the number of q in order to gain enough information for solving σ for each layer as well as AF for each Tx-Rx configuration. L is a discrete regularization matrix based on a second-order Laplacian operator which minimizes between the norm of the residual and the norm of the second derivative of σ (Borchers et al., 1997), and is shown as

$$\mathbf{L} = \begin{bmatrix} 1 & -2 & 1 & & & & & 0 \\ & 1 & -2 & 1 & & & & \\ & & & \ldots & & & & \\ & & & & 1 & -2 & 1 & 0 \end{bmatrix}. \tag{B.6}$$

Note that no regularization is applied to the variable AF because each AF is independent, therefore the last $(m \times q)$ by m sub-matrix of $\mathbf{L}$ is an empty matrix. λ is the regularization

factor with the value of 0.01 based on the L-curved optimization (Borchers et al., 1997; Santos et al., 2010). By approximating the equation B.5 to zero, and by adding an additional regularization matrix $\mathbf{E}$ to the iteration step ($\Delta\mathbf{p}$), the objective function is equivalent to

$$(\mathbf{J}_i^T\mathbf{J}_i + \lambda^2\mathbf{L}^T\mathbf{L} + \mu^2\mathbf{E}^T\mathbf{E})\,\Delta\mathbf{p} = \mathbf{J}_i^T[f(\mathbf{p}_i) - \mathrm{ECa}^{\mathrm{mea}}] - \lambda^2\mathbf{L}^T\mathbf{L}\mathbf{p}_i. \tag{B.7}$$

In the current study, $\mathbf{E}$ is a unit diagonal matrix with a regularization factor μ of 0.01. Consequently, the iteration step $\Delta\mathbf{p}$ can be obtained from equation B.7, and then is added to the next iteration until the inversion convergence is reached.

B.2 Noise-free Model Simulation

Three synthetic simulations including 1-, 2-, and 3-layer subsurface models were built to verify the Gauss-Newton based calibration and inversion approach. Parameters for the three true models are shown in table B.1, and are the same as the simulations in section 3.5 (Chapter 3). Meanwhile, artificial $\mathrm{AF}^{\mathrm{syn}}$ for each Tx-Rx configuration is also the same as the previous investigations and is shown in table 3.2.

Table B.1: Parameters of the synthetic models

Model	σ (mS/m)	thickness (m)
1-layer	20	-
2-layer	20, 40	0.3
3-layer	10, 20, 50	0.3, 0.5

Inverted results of three synthetic models are presented in figure B.1. The L2-norm misfit between the $f(\mathbf{p}_i)$ and $\mathrm{ECa}^{\mathrm{mea}}$ (equation 3.11) for the 1-layer model returned the value of 6.5×10^{-7} while results from the 2- and 3-layer models returned the L2-norm misfits of 1.5×10^{-4}, and 1.3×10^{-4}, respectively. Note that the true models are clearly layered subsurfaces with strong layer boundaries, whereas the Gauss-Newton based method returned smoothed layering for the 2- and 3-layer models. However, it is noticed that the inverted σ value of the 1-layer inverted model returned a value of 18.2 mS/m which is shifted from the true value which is 20 mS/m. It is probably because the Gauss-Newton method solves for the smooth-constrained input variables such as the electrical conductivity between each layer, and therefore might not able to find the true value for the independent variables such as the additive factor.

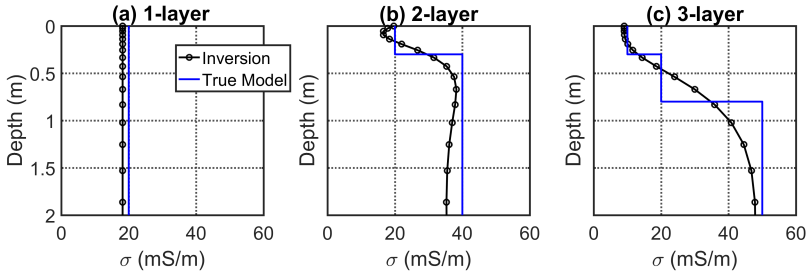

Figure B.1: Inversion results for (a) homogeneous, (b) two-layer and (c) three-layer subsurface models using Gauss-Newton inversion algorithm (black lines with circles) and their corresponding true models (blue lines).

B.3 Noisy Model Simulation

By adding the random normally distributed noise with a magnitude of 0.1 mS/m to the ECa^{mea} value of each Tx-Rx configuration, the inverted results of the three synthetic models were obtained and are shown in figure B.2. Grey dashed curves show the inverted results of 20 independent simulations for each synthetic model from which the mean values shown in red were obtained. In general, the mean results of three models show good agreements with the synthetic models, and returned the mean absolute shift of 0.9, 1.5, and 1.3 mS/m between inverted and synthetic ECa values for 1-, 2-, and 3-layer models, respectively. Respecting to the 'blocky' synthetic models, the smooth-constrained Gauss-Newton method shows promising results which can be applied for the field applications.

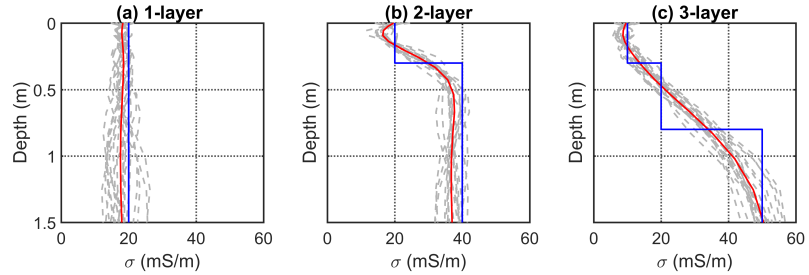

Figure B.2: Inversion results for the subsurface models with 0.1 mS/m noise added to the apparent electrical conductivity values. The grey dashed lines show the inversion results of twenty simulations, and the red solid lines represent their mean values.

B.4 Experimental Investigations

An experimental measurement was performed on the test field (Klein Altendorf, Germany) in February, 2016. The multi-elevation measurement was performed using a CMD-SE EMI system with HCP configurations for eight elevations which are 0, 0.05, 0.2, 0.4, 0.6, 0.8, 1.0, and 1.2 m. Meanwhile, the vertical electrical sounding (VES) measurement on the same location was carried out as the verification method.

Figure B.3 presents the inverted subsurface models obtained from the Gauss-Newton method and the VES inversion algorithm implemented by von Hebel (2016). Similar results were returned indicating the applicability of the presented Gauss-Newton based inversion approach. Nevertheless deviations are observed for both the shallow and deep layers which need further investigation and optimization.

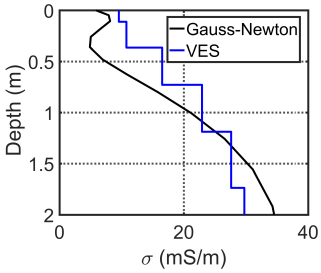

Figure B.3: Inverted subsurface model using Gauss-Newton based method (black), and VES based inversion approach (blue, von Hebel, 2016).

The measured (ECa^{mea}, un-calibrated), calibrated (ECa^{cal}, based on the Gauss-Newton method), and the reference (ECa^{VES}, obtained from VES measurement) ECa values for all six configurations are presented against to the corresponding measurement elevations in figure B.4. Note that the ECa^{VES} values were obtained by input the inverted subsurface model (figure B.3) to the forward modeling for each Tx-Rx configuration and elevation.

From the results, it is observed that ECa^{cal} values for all six Tx-Rx configurations are approaching ECa^{VES} values. Good agreements have been returned between ECa^{cal} and ECa^{VES} for the higher elevations (from 0.6 to 1.2 m), whereas misfits for the small elevations were observed. It is probably due to the multiplicative factors which were indicated during previous experiments (chapter 3) but cannot be solved by the Gauss-Newton method. Nevertheless,

the small mean absolute shift (MAS) between ECa^{cal} and ECa^{VES} (presented in figure B.4) with the value between 0.3 and 1 mS/m indicates the promising results as well as the feasibility of further developments.

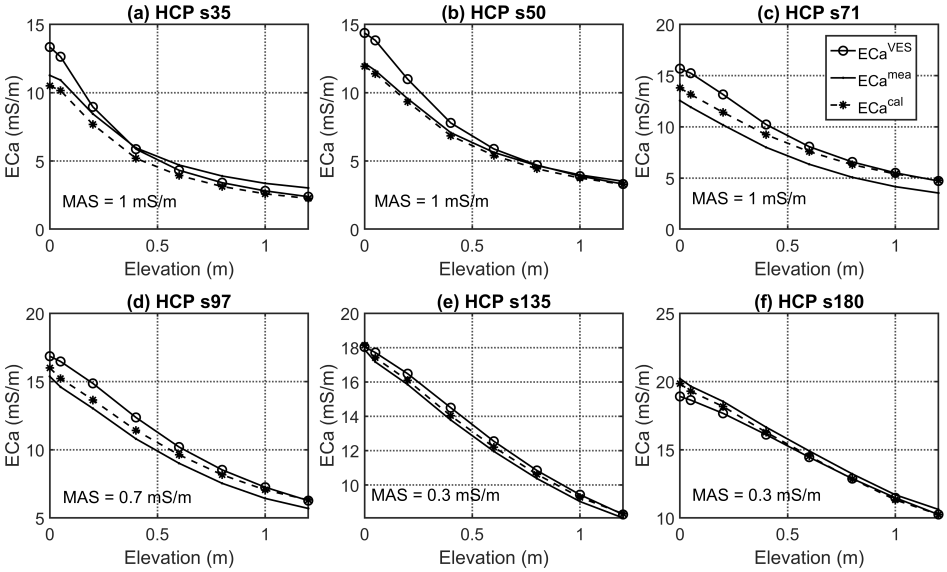

Figure B.4: Measured ECa (ECa^{mea}), and calibrated ECa using Gauss-Newton method (ECa^{cal}) and VES (ECa^{VES}) methods.

C. 3D Forward Modeling

As a preliminary investigation, a transmitter coil was modeled placing horizontally above a homogeneous soil block (figure C.1) using finite-element 3D modeling software (COMSOL Multiphysics, Sweden). The modeled soil block as shown in figure C.1 has the dimension of 0.6 m× 0.6 m×0.3 m with the electrical conductivity of 20 mS/m. An air block was built up with the dimension of 1 m× 1 m×0.6 m covering the transmitter coil and the soil block, while the coil is placed in the central point of the air block. The coil parameters shown in table C.1 are based on the system design from Mester et al. (2014). Consequently, the induced electric fields are plotted as top and front view 2D images in figure C.2a and b, respectively.

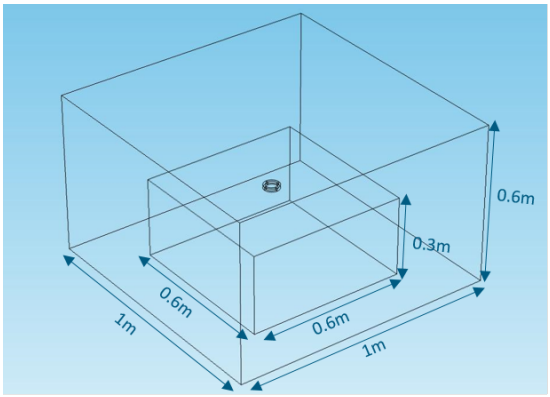

Figure C.1: The 3D model of a transmitter coil placed horizontally above a homogeneous soil block (inner block, dimension of 0.6 m× 0.6 m×0.3 m) with an electrical conductivity of 20 mS/m. An air block (outer block) with zero electrical conductivity is build with dimensions of 1 m× 1 m×0.6 m. This model is modeled in COMSOL Multiphysics (Sweden) modelling software.

Figure C.2 shows the total field, while the primary field can be obtained by simulating

Table C.1: Coil property for the 3D modeling

Coil Property	Value
Wire radius (m)	3.35×10^{-4}
Number of turns (-)	105
Cross-section area of the wire (m^2)	3.5×10^{-7}
Outer radius (mm)	30
Radial coil height (mm)	8
Coil impedance (Ω)	$42.2 \angle 1.6$
Excitation frequency (kHz)	10
Voltage (V)	1
Current (A)	0.024

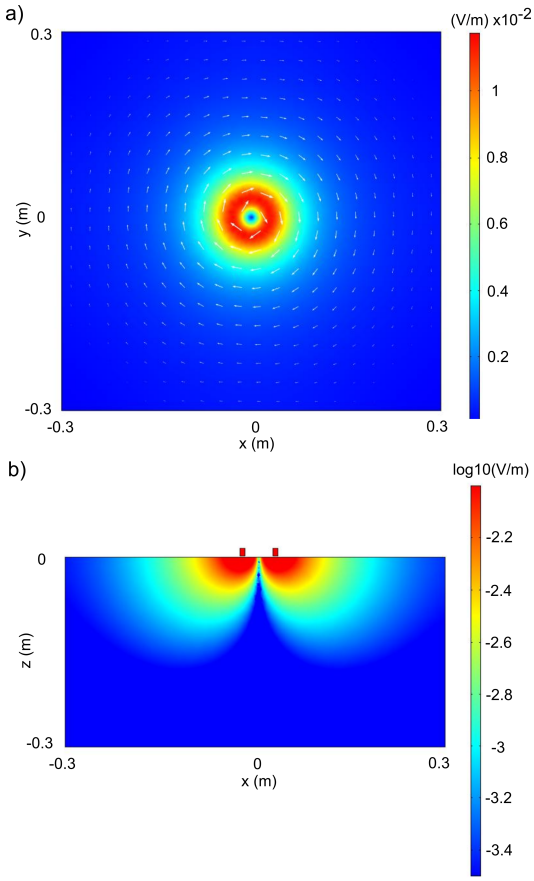

Figure C.2: 2D images in top view (a) as well as front view (b) of the induced electrical fields obtained from the 3D modeling in figure C.1.

the same model but setting soil block to zero electrical conductivity. Consequently, the secondary field can be obtained according to equation 3.5, and then the term $\mathrm{Im}(H_s^*/H_p^*)$ (figure C.3, red curve) for calculating the ECa value (equation 3.6) were obtained. In order to compare with the full-solution result, the corresponding simulation described in section 3.1 was performed and is plotted as the black curve in figure C.3.

It is observed that misfits (figure C.3, blue curves) between the 3D and 1D synthetic model are significant although promising visualization results of the electromagnetic fields have been returned (figure C.2). Nevertheless, analytical investigations such as parameter studies of the mesh size and boundary conditions are necessary.

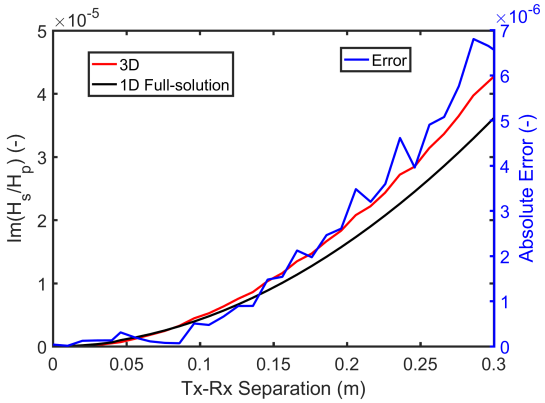

Figure C.3: 1D (black) and 3D (red) responses of the term $\mathrm{Im}(H_s^*/H_p^*)$ with the absolute error (blue).

List of Figures

List of Tables

Bibliography

Abdu, H., D. A. Robinson, and S. B. Jones (2007). "Comparing bulk soil electrical conductivity determination using the DUALEM-1S and EM38-DD electromagnetic induction instruments". In: *Soil Science Society of America Journal* 71.1, pp. 189–196.

Abdu, H., D. A. Robinson, M. Seyfried, and S. B. Jones (2008). "Geophysical imaging of watershed subsurface patterns and prediction of soil texture and water holding capacity". In: *Water resources research* 44.4.

Adamchuk, V. I., J. W. Hummel, M. T. Morgan, and S. K. Upadhyaya (2004). "On-the-go soil sensors for precision agriculture". In: *Computers and electronics in agriculture* 44.1, pp. 71–91.

Altdorff, D., M. Bechtold, J. van der Kruk, H. Vereecken, and J. A. Huisman (2016). "Mapping peat layer properties with multi-coil offset electromagnetic induction and laser scanning elevation data". In: *Geoderma* 261, pp. 178–189.

Altdorff, D., C. von Hebel, N. Borchard, J. van der Kruk, H. R. Bogena, H. Vereecken, and J. A. Huisman (2017). "Potential of catchment-wide soil water content prediction using electromagnetic induction in a forest ecosystem". In: *Environmental Earth Sciences* 76.3, p. 111. ISSN: 1866-6299. DOI: 10.1007/s12665-016-6361-3.

Altdorff, D., L. Galagedara, M. Nadeem, M. Cheema, and A. Unc (2018). "Effect of agronomic treatments on the accuracy of soil moisture mapping by electromagnetic induction". In: *Catena* 164, pp. 96–106.

Amezketa, E. (2006). "An integrated methodology for assessing soil salinization, a precondition for land desertification". In: *Journal of Arid Environments* 67.

Bogena, H. R., C. Montzka, J. A. Huisman, A. Graf, M. Schmidt, M. Stockinger, C. von Hebel, H. J. Hendricks-Franssen, J. van der Kruk, W. Tappe, et al. (2018). "The TERENO-Rur Hydrological Observatory: A Multiscale Multi-Compartment Research Platform for the Advancement of Hydrological Science". In: *Vadose Zone Journal* 17.1.

Borchers, B., T. Uram, and J. M. H. Hendrickx (1997). "Tikhonov regularization of electrical conductivity depth profiles in field soils". In: *Soil Science Society of America Journal* 61.4, pp. 1004–1009.

Bring, J. (1994). "How to standardize regression coefficients". In: *The American Statistician* 48.3, pp. 209–213.

Brogi, C., J. A. Huisman, S. Pätzold, C. von Hebel, L. Weihermüller, M. S. Kaufmann, J. van der Kruk, and H. Vereecken (2019). "Large-scale soil mapping using multi-configuration EMI and supervised image classification". In: *Geoderma* 335, pp. 133–148.

Busch, S., J. van der Kruk, and H. Vereecken (2014). "Improved characterization of fine-texture soils using on-ground GPR full-waveform inversion". In: *IEEE Transactions on Geoscience and Remote Sensing* 52.7, pp. 3947–3958.

Busch, S., L. Weihermüller, J. A. Huisman, C. M. Steelman, A. L. Endres, H. Vereecken, and J. van der Kruk (2013). "Coupled hydrogeophysical inversion of time-lapse surface GPR data to estimate hydraulic properties of a layered subsurface". In: *Water Resources Research* 49.12, pp. 8480–8494.

Butler, D. K. (2005). *Near-surface geophysics*.

Corwin, D. and S. Lesch (2005). "Apparent soil electrical conductivity measurements in agriculture". In: *Computers and electronics in agriculture* 46.1-3, pp. 11–43.

Corwin, D. L. and S. M. Lesch (2003). "Application of soil electrical conductivity to precision agriculture". In: *Agronomy journal* 95.3, pp. 455–471.

Corwin, D. L. and J. D. Rhoades (1982). "An Improved Technique for Determining Soil Electrical Conductivity-Depth Relations from Above-ground Electromagnetic Measurements 1". In: *Soil Science Society of America Journal* 46.3, pp. 517–520.

De Smedt, P., T. Saey, A. Lehouck, B. Stichelbaut, E. Meerschman, M. M. Islam, E. Van De Vijver, and M. Van Meirvenne (2013). "Exploring the potential of multi-receiver EMI survey for geoarchaeological prospection: A 90 ha dataset". In: *Geoderma* 199, pp. 30–36.

Deszcz-Pan, M., D. V. Fitterman, and V. F. Labson (1998). "Reduction of inversion errors in helicopter EM data using auxiliary information". In: *Exploration Geophysics* 29.1/2, pp. 142–146.

Doolittle, J. A. and E. C. Brevik (2014). "The use of electromagnetic induction techniques in soils studies". In: *Geoderma* 223, pp. 33–45.

Duan, Q., V. K. Gupta, and S. Sorooshian (1993). "Shuffled complex evolution approach for effective and efficient global minimization". In: *Journal of optimization theory and applications* 76.3, pp. 501–521.

Duan, Q., S. Sorooshian, and V. K. Gupta (1994). "Optimal use of the SCE-UA global optimization method for calibrating watershed models". In: *Journal of hydrology* 158.3-4, pp. 265–284.

Fitterman, D. V. and M. Deszcz-Pan (1998). "Helicopter EM mapping of saltwater intrusion in Everglades National Park, Florida". In: *Exploration Geophysics* 29.1/2, pp. 240–243.

Frederiksen, R. R., A. V. Christiansen, S. Christensen, and K. R. Rasmussen (2017). "A direct comparison of EMI data and borehole data on a 1000 ha data set". In: *Geoderma* 303, pp. 188–195.

Frischknecht, F. C., V. F. Labson, B. R. Spies, and W. L. Anderson (1991). "Profiling methods using small sources". In: *Electromagnetic methods in applied geophysics* 2.part A, pp. 105–270.

Gebbers, R., E. Lück, M. Dabas, and H. Domsch (2009). "Comparison of Instruments for Geoelectrical Soil Mapping at the Field Scale". In: *Near Surface Geophysics* 7, pp. 179–190.

Guillemoteau, J., E. Lück, and J. Tronicke (2017). "1D inversion of direct current data acquired with a rolling electrode system". In: *Journal of Applied Geophysics* 146, pp. 167–177.

Guillemoteau, J., F.-X. Simon, E. Lück, and J. Tronicke (2016). "1D sequential inversion of portable multi-configuration electromagnetic induction data". In: *Near Surface Geophysics* 14.5, pp. 423–432.

Günther, T., C. Rücker, and K. Spitzer (2006). "Three-dimensional modelling and inversion of DC resistivity data incorporating topography—II. Inversion". In: *Geophysical Journal International* 166.2, pp. 506–517.

Hendrickx, J. M. H., B. Borchers, D. L. Corwin, S. M. Lesch, A. C. Hilgendorf, and J. Schlue (2002). "Inversion of soil conductivity profiles from electromagnetic induction measurements". In: *Soil Science Society of America Journal* 66.3, pp. 673–685.

Holden, P. A. and N. Fierer (2005). "Microbial processes in the vadose zone". In: *Vadose Zone Journal* 4.1, pp. 1–21.

Huang, J., T. Koganti, F. A. M. Santos, and J. Triantafilis (2017). "Mapping soil salinity and a fresh-water intrusion in three-dimensions using a quasi-3d joint-inversion of DUALEM-421S and EM34 data". In: *Science of the Total Environment* 577, pp. 395–404.

Huisman, J. A., S. S. Hubbard, J. D. Redman, and A. P. Annan (2003). "Measuring soil water content with ground penetrating radar". In: *Vadose zone journal* 2.4, pp. 476–491.

Huisman, J. A., E. Zimmermann, O. Esser, F.-H. Haegel, A. Treichel, and H. Vereecken (2016). "Evaluation of a novel correction procedure to remove electrode impedance effects from broadband SIP measurements". In: *Journal of Applied Geophysics* 135, pp. 466–473.

Hunkeler, P. A., S. Hendricks, M. Hoppmann, S. Paul, and R. Gerdes (2015). "Towards an estimation of sub-sea-ice platelet-layer volume with multi-frequency electromagnetic induction sounding". In: *Annals of Glaciology* 56.69, pp. 137–146.

Iwanowitsch, M. (2018). "Investigating soil water dynamics using repeated quantitative rigid boom mulit-coil EMI measurements and inversions". Masterarbeit, RWTH Aachen, 2018. Jülich: RWTH Aachen University. eprint: `http://hdl.handle.net/2128/20266`.

Jadoon, K. Z., D. Moghadas, A. Jadoon, T. M. Missimer, S. K. Al-Mashharawi, and M. F. McCabe (2015). "Estimation of soil salinity in a drip irrigation system by using joint inversion of multicoil electromagnetic induction measurements". In: *Water Resources Research* 51.5, pp. 3490–3504.

Klostermann, J. (1992). *Das Quartär der Niederrheinischen Bucht: Ablagerungen der letzten Eiszeit am Niederrhein*. Geologisches Landesamt Nordrhein-Westfalen.

Klotzsche, A., J. van der Kruk, N. Linde, J. Doetsch, and H. Vereecken (2013). "3-D characterization of high-permeability zones in a gravel aquifer using 2-D crosshole GPR full-waveform inversion and waveguide detection". In: *Geophysical Journal International* 195.2, pp. 932–944.

Klotzsche, A., J. van der Kruk, G. A. Meles, J. Doetsch, H. Maurer, and N. Linde (2010). "Full-waveform inversion of cross-hole ground-penetrating radar data to characterize a gravel aquifer close to the Thur River, Switzerland". In: *Near surface geophysics* 8.6, pp. 635–649.

Lavoué, F., J. van der Kruk, J. Rings, F. André, D. Moghadas, J. A. Huisman, S. Lambot, L. Weihermüller, J. Vanderborght, and H. Vereecken (2010). "Electromagnetic induction calibration using apparent electrical conductivity modelling based on electrical resistivity tomography". In: *Near surface geophysics* 8.6, pp. 553–561.

Léger, E., A. Saintenoy, and Y. Coquet (2014). "Hydrodynamic parameters of a sandy soil determined by ground-penetrating radar inside a single ring infiltrometer". In: *Water Resources Research* 50.7, pp. 5459–5474.

Léger, E., A. Saintenoy, P. Tucholka, and Y. Coquet (2016). "Hydrodynamic Parameters of a Sandy Soil Determined by Ground-Penetrating Radar Monitoring of Porchet Infiltrations". In: *IEEE Journal of Selected Topics in Applied Earth Observations and Remote Sensing* 9.1, pp. 188–200.

Lesch, S. M., D. J. Strauss, and J. D. Rhoades (1995). "Spatial prediction of soil salinty using electromagnetic induction techniques, 2. An efficient spatial sampling algorithm suitable for multiple linear regression model identification and estimation". In: *Water Resources Research* 31.

Lesch, S., D. Corwin, and D. Robinson (2005). "Apparent soil electrical conductivity mapping as an agricultural management tool in arid zone soils". In: *Computers and Electronics in Agriculture* 46.

Liu, T., A. Klotzsche, M. Pondkule, H. Vereecken, Y. Su, and J. van der Kruk (2018). "Radius Estimation of Subsurface Sylindrical Object from GPR Data Using Full-waveform Inversion". In: *GEOPHYSICS*, pp. 1–48.

Lück, E., R. Gebbers, J. Ruehlmann, and U. Spangenberg (2009). "Electrical conductivity mapping for precision farming". In: *Near Surf. Geophys* 7.1, pp. 15–25.

Manfreda, S. and I. Rodríguez-Iturbe (2006). "On the spatial and temporal sampling of soil moisture fields". In: *Water resources research* 42.5.

Mangel, A. R., S. M. J. Moysey, and J. van der Kruk (2017). "Resolving Infiltration-Induced Water Content Profiles by Inversion of Dispersive Ground-Penetrating Radar Data". In: *Vadose Zone Journal* 16.10.

McNeill, J. D. (1980). "Electromagnetic Terrain Conductivity Measurement at Low Induction Numbers". In: *Technical Note TN-6*.

Mester, A., E. Zimmermann, J. van der Kruk, H. Vereecken, and S. van Waasen (2014). "Development and drift-analysis of a modular electromagnetic induction system for shallow ground conductivity measurements". In: *Measurement Science and Technology* 25.5, p. 055801.

Mester, A. (2015). "Quantitative Two-Layer Inversion and Customizable Sensor-Array Instrument for Electromagnetic Induction based Soil Conductivity Estimation". RWTH Aachen University, Diss., 2014. Jülich: RWTH Aachen University, viii, 119 pp. ISBN: 978-3-95806-035-7.

Mester, A., J. van der Kruk, E. Zimmermann, and H. Vereecken (2011). "Quantitative two-layer conductivity inversion of multi-configuration electromagnetic induction measurements". In: *Vadose Zone Journal* 10.4, pp. 1319–1330.

Metternicht, G. I. and J. A. Zinck (2003). "Remote sensing of soil salinity: potentials and constraints". In: *Remote sensing of Environment* 85.1, pp. 1–20.

Minsley, B. J., M. A. Kass, G. Hodges, and B. D. Smith (2014). "Multielevation calibration of frequency-domain electromagnetic data". In: *Geophysics* 79.5, E201–E216.

Minsley, B. J., B. D. Smith, R. Hammack, J. I. Sams, and G. Veloski (2012). "Calibration and filtering strategies for frequency domain electromagnetic data". In: *Journal of Applied Geophysics* 80, pp. 56–66.

Moghadas, D., F. Andre, J. H. Bradford, J. van der Kruk, H. Vereecken, and S. Lambot (2012). "Electromagnetic induction antenna modelling using a linear system of complex antenna transfer functions". In: *Near Surface Geophysics* 10, pp. 237–247.

Nimmo, J. R. (2009). "Vadose water". In: *Encyclopedia of Inland Waters* 1, pp. 766–777.

Nüsch, A.-K., P. Dietrich, U. Werban, T. Behrens, and N. Prakongkep (2010). "Acquisition and reliability of geophysical data in soil science". In: *19th World Congress of Soil Science*, pp. 21–24.

Ochs, J., T. Hiller, and N. Klitzsch (2019). "Combining ERT, NMR and matric potential measurements for characterizing the vadose zone". In: *Conference: EGU General Assembly 2019, Vienna. Austria*.

Patzold, S., F. M. Mertens, L. Bornemann, B. Koleczek, J. Franke, H. Feilhauer, and G. Welp (2008). "Soil heterogeneity at the field scale: a challenge for precision crop protection". In: *Precision Agriculture* 9.6, pp. 367–390. ISSN: 1573-1618. DOI: 10.1007/s11119-008-9077-x.

Pellerin, L. and P. E. Wannamaker (2005). "Multi-dimensional electromagnetic modeling and inversion with application to near-surface earth investigations". In: *Computers and electronics in agriculture* 46.1-3, pp. 71–102.

Raiche, A. P. (1988). "Inversion of controlled-source electromagnetic data". In: *Electromagnetic Methods in Applied Geophysics: Theory* 1, p. 469.

Reedy, R. C. and B. R. Scanlon (2003). "Soil water content monitoring using electromagnetic induction". In: *Journal of Geotechnical and Geoenvironmental Engineering* 129.11, pp. 1028–1039.

Reynolds, J. M. (2011). *An introduction to applied and environmental geophysics*. John Wiley & Sons.

Robinson, D. A., A. Binley, N. Crook, F. D. Day-Lewis, T. P. A. Ferré, V. J. S. Grauch, R. Knight, M. Knoll, V. Lakshmi, R. Miller, et al. (2008). "Advancing process-based watershed hydrological research using near-surface geophysics: A vision for, and review of, electrical and magnetic geophysical methods". In: *Hydrological Processes: An International Journal* 22.18, pp. 3604–3635.

Robinson, D. A., S. B. Jones, J. M. Wraith, D. Or, and S. P. Friedman (2003). "A review of advances in dielectric and electrical conductivity measurement in soils using time domain reflectometry". In: *Vadose Zone Journal* 2.4, pp. 444–475.

Robinson, D. A., I. Lebron, B. Kocar, K. Phan, M. Sampson, N. Crook, and S. Fendorf (2009). "Time-lapse geophysical imaging of soil moisture dynamics in tropical deltaic soils: An aid to interpreting hydrological and geochemical processes". In: *Water Resources Research* 45.4.

Robinson, D. A., I. Lebron, S. M. Lesch, and P. Shouse (2004). "Minimizing drift in electrical conductivity measurements in high temperature environments using the EM-38". In: *Soil Science Society of America Journal* 68.2, pp. 339–345.

Rücker, C., T. Günther, and F. M. Wagner (2017). "pyGIMLi: An open-source library for modelling and inversion in geophysics". In: *Computers & Geosciences* 109, pp. 106–123.

Rudolph, S., J. van der Kruk, C. von Hebel, M. Ali, M. Herbst, C. Montzka, S. Pätzold, D. Robinson, H. Vereecken, and L. Weihermüller (2015). "Linking satellite derived LAI patterns with subsoil heterogeneity using large-scale ground-based electromagnetic induction measurements". In: *Geoderma* 241-242, pp. 262 –271. ISSN: 0016-7061. DOI: https://doi.org/10.1016/j.geoderma.2014.11.015.

Saey, T., P. De Smedt, S. Delefortrie, E. Van De Vijver, and M. Van Meirvenne (2015). "Comparing one-and two-dimensional EMI conductivity inverse modeling procedures for characterizing a two-layered soil". In: *Geoderma* 241, pp. 12–23.

Samouëlian, A., I. Cousin, A. Tabbagh, A. Bruand, and G. Richard (2005). "Electrical resistivity survey in soil science: a review". In: *Soil and Tillage research* 83.2, pp. 173–193.

Santos, F. A. M., J. Triantafilis, R. S. Taylor, S. Holladay, and K. E. Bruzgulis (2010). "Inversion of Conductivity Profiles from EM Using Full Solution and a 1-D Laterally Constrained Algorithm". In: *Journal of Environmental and Engineering Geophysics* 15.3, pp. 163–174. DOI: 10.2113/JEEG15.3.163.

Sasaki, Y., J.-S. Son, C. Kim, and J.-H. Kim (2008). "Resistivity and offset error estimations for the small-loop electromagnetic method". In: *Geophysics* 73.3, F91–F95.

Schamper, C., E. Auken, and K. Sørensen (2014). "Coil response inversion for very early time modelling of helicopter-borne time-domain electromagnetic data and mapping of near-surface geological layers". In: *Geophysical Prospecting* 62.3, pp. 658–674.

Simmer, C., I. Thiele-Eich, M. Masbou, W. Amelung, H. Bogena, S. Crewell, B. Diekkrüger, F. Ewert, H.-J. Hendricks Franssen, J. A. Huisman, et al. (2015). "Monitoring and modeling the terrestrial system from pores to catchments: the transregional collaborative research center on patterns in the soil–vegetation–atmosphere system". In: *Bulletin of the American Meteorological Society* 96.10, pp. 1765–1787.

Spies, B. R. (1989). "Depth of investigation in electromagnetic sounding methods". In: *Geophysics* 54.7, pp. 872–888.

Spies, B. R. and F. C. Frischknecht (1991). "Electromagnetic sounding". In: *Electromagnetic methods in applied geophysics* 2.Part A, pp. 285–426.

Stockmann, U., J. Huang, B. Minasny, and J. Triantafilis (2017). "Utilizing a DUALEM-421 and inversion modelling to map baseline soil salinity along toposequences in the Hunter Valley Wine district". In: *Soil Use and Management* 33.3, pp. 413–424.

Sudduth, K. A., S. T. Drummond, and N. R. Kitchen (2001). "Accuracy issues in electromagnetic induction sensing of soil electrical conductivity for precision agriculture". In: *Computers and Electronics in Agriculture* 31.3, pp. 239 –264. ISSN: 0168-1699. DOI: https://doi.org/10.1016/S0168-1699(00)00185-X.

Tan, X., A. Mester, C. von Hebel, E. Zimmermann, H. Vereecken, S. van Waasen, and J. van der Kruk (2019). "Simultaneous calibration and inversion algorithm for multiconfiguration electromagnetic induction data acquired at multiple elevationsCalibration inversion for rigid-boom EMI". In: *Geophysics* 84.1, EN1–EN14. DOI: 10.1190/geo2018-0264.1.

Thiesson, J., P. Kessouri, C. Schamper, and A. Tabbagh (2014). "Calibration of frequency-domain electromagnetic devices used in near-surface surveying". In: *Near Surface Geophysics* 12.4, pp. 481–491.

Triantafilis, J., A. I. Huckel, and I. Odeh (2001). "Comparison of statistical prediction methods for estimating field-scale clay content using different combinations of ancillary variables". In: *Soil Science* 166.6, pp. 415–427.

Triantafilis, J., G. M. Laslett, and A. B. McBratney (2000). "Calibrating an electromagnetic induction instrument to measure salinity in soil under irrigated cotton". In: *Soil Science Society of America Journal* 64.3, pp. 1009–1017.

Triantafilis, J. and F. A. M. Santos (2010). "Resolving the spatial distribution of the true electrical conductivity with depth using EM38 and EM31 signal data and a laterally constrained inversion model". In: *Soil Research* 48.5, pp. 434–446.

Triantafilis, J. and S. M. Lesch (2005). "Mapping clay content variation using electromagnetic induction techniques". In: *Computers and Electronics in Agriculture* 46.1-3, pp. 203–237.

van der Kruk, J., J. A. C. Meekes, P. M. van den Berg, and J. T. Fokkema (2000). "An apparent-resistivity concept for low-frequency electromagnetic sounding techniques". In: *Geophysical Prospecting* 48.6, pp. 1033–1052.

Vanderborght, J., J. A. Huisman, J. van der Kruk, and H. Vereecken (2013). "Geophysical methods for field-scale imaging of root zone properties and processes". In: *Soil–water–root processes: Advances in tomography and imaging* soilwaterrootpr, pp. 247–282.

Vereecken, H., J. A. Huisman, H. Bogena, J. Vanderborght, J. A. Vrugt, and J. W. Hopmans (2008). "On the value of soil moisture measurements in vadose zone hydrology: A review". In: *Water resources research* 44.4.

Vereecken, H., J. A. Huisman, Y. Pachepsky, C. Montzka, J van der Kruk, H. Bogena, L Weihermüller, M. Herbst, G. Martinez, and J. Vanderborght (2014). "On the spatio-

temporal dynamics of soil moisture at the field scale". In: *Journal of Hydrology* 516, pp. 76–96.

von Hebel, C., M. Matveeva, E. Verweij, P. Rademske, M. S. Kaufmann, C. Brogi, H. Vereecken, U. Rascher, and J. van der Kruk (2018). "Understanding soil and plant interaction by combining ground-based quantitative electromagnetic induction and airborne hyperspectral data". In: *Geophysical Research Letters* 45.15, pp. 7571–7579.

von Hebel, C., S. Rudolph, A. Mester, J. A. Huisman, P. Kumbhar, H. Vereecken, and J. van der Kruk (2014). "Three-dimensional imaging of subsurface structural patterns using quantitative large-scale multiconfiguration electromagnetic induction data". In: *Water Resources Research* 50.3, pp. 2732–2748.

von Hebel, C. (2016). "Calibration and large-scale inversion of multi-configuration electromagnetic induction data for vadose zone characterization". Dissertation, RWTH Aachen University, 2016. Jülich: RWTH Aachen University, pp. ix, 123. ISBN: 978-3-95806-210-8.

Wagner, W., G. Blöschl, P. Pampaloni, J.-C. Calvet, B. Bizzarri, J.-P. Wigneron, and Y. Kerr (2007). "Operational readiness of microwave remote sensing of soil moisture for hydrologic applications". In: *Hydrology Research* 38.1, pp. 1–20.

Ward, S. H., G. W. Hohmann, and M. Nabighian (1988). "Electromagnetic theory for geophysical applications". In: *Electromagnetic methods in applied geophysics*. Vol. 1. 3, pp. 131–311.

Weihermueller, L., J. A. Huisman, N. Hermes, S. Pickel, and H. Vereecken (2013). "A new TDR multiplexing system for reliable electrical conductivity and soil water content measurements". In: *Vadose Zone Journal* 12.2.

Weihermüller, L., J. A. Huisman, S. Lambot, M. Herbst, and H. Vereecken (2007). "Mapping the spatial variation of soil water content at the field scale with different ground penetrating radar techniques". In: *Journal of Hydrology* 340.3-4, pp. 205–216.

Won, I. J., A. Oren, and F. Funak (2003). "GEM-2A: A programmable broadband helicopter-towed electromagnetic sensorGEM-2A HEM Sensor". In: *Geophysics* 68.6, pp. 1888–1895.

Wraith, J. M., D. A. Robinson, S. B. Jones, and D. S. Long (2005). "Spatially characterizing apparent electrical conductivity and water content of surface soils with time domain reflectometry". In: *Computers and Electronics in Agriculture* 46.1-3, pp. 239–261.

Zimmermann, E., A. Kemna, J. Berwix, W. Glaas, H. M. Münch, and J. A. Huisman (2008a). "A high-accuracy impedance spectrometer for measuring sediments with low polarizability". In: *Measurement Science and Technology* 19.10, p. 105603.

Zimmermann, E., A. Kemna, J. Berwix, W. Glaas, and H. Vereecken (2008b). "EIT measurement system with high phase accuracy for the imaging of spectral induced polarization properties of soils and sediments". In: *Measurement Science and Technology* 19.9, p. 094010.

Acknowledgements

The presented thesis is developed and accomplished in the Central Institute of Engineering, Electronics and Analytics, Electronic Systems (ZEA-2) in cooperation with the Institute of Bio- and Geosciences, Agrosphere (IGB-3) of Research Center Juelich. I thank ZEA-2 and IBG-3 for all the support I got during my doctoral research period. I also thank the support from the German Research Foundation (Transregional Collaborative Research Center 32 — Patterns in Soil-Vegetation-Atmosphere Systems: Monitoring, Modeling and Data Assimilation), "Terrestrial Environmental Observatories" (TERENO), and Advanced Remote Sensing — Ground-Truth Demo and Test Facilities (ACROSS).

I would like to express my great gratitude to my scientific advisor, Dr. Achim Mester, who is always kind and patient to guide me out from confusions and helped me a lot for solving questions. He is so general offering his help which leads me through all the difficulties during my thesis work.

I also would like to thank my doctoral supervisor, Prof. Dr. Jan van der Kruk for his enthusiasm during each discussion, for his fruity ideas pop-up which broke the barriers standing ahead of my research, and for his precise attitude of scientific from which I should never stop learning.

I thank my team leader Dr. Egon Zimmermann in ZEA-2, who is always humor and inspiring. He never knows how much his positive and easy-going attitudes have influenced my work and life. I also thank our team members Walter Glaas, Markus Dick, and Michael Ramm, who helped me a lot during the TFA development process. It is a great experience to work in this lovely team.

I also thank the head of ZEA-2 Prof. Dr. Stefan van Waasen who offered me this great opportunity to do my doctoral research in ZEA-2 and brings me such a great chance to work with all my colleagues.

I thank Dr. Christian von Hebel for his patient and detailed feedbacks on paper

manuscripts, presentations, and posters. I thank for all his interesting ideas and helpful suggestions regarding the EMI calibration methods.

I thank Johanna Ochs and Dr. Norbert Klitzsch for providing the ERT inversion data with electrode corrections which have been implemented in chapter 4 as one of the verification methods.

I thank Manuela Kaufmann, Cosimo Brogi, Pascha Mozaffari, Igor Dal Bo, Luka Kurnjek, Michael Iwanowitsch, Carlos Manuel, and Ocampo Ortiz for helping out EMI field measurements.

I thank Pavithra Muralidharan. We went through a hard time during our thesis writing together. Those are the moments that I will never forget.

Finally, I would like to thank my dear mother Li, my dear father Xiaowei and my beloved husband Zhengyang. Without their support and encouragement, I would never think of doing my doctoral study. Things could not happen without you standing behind me.

Band / Volume 48
Investigation of ternary nitride semiconductor alloys by scanning tunneling microscopy
V. Portz (2017), 140 pp
ISBN: 978-3-95806-232-0

Band / Volume 49
Redox processes and ionic transport in resistive switching binary metal oxides
K. Skaja (2017), VII, 203 pp
ISBN: 978-3-95806-236-8

Band / Volume 50
Investigation of switching mechanism in Ta_2O_5-based ReRAM devices
K. Wonjoo (2017), iii, 138 pp
ISBN: 978-3-95806-261-0

Band / Volume 51
Development of ReRAM-based Devices for Logic- and Computation-in-Memory Applications
T. Breuer (2017), x, 179 pp
ISBN: 978-3-95806-270-2

Band / Volume 52
Resistive switching memory devices from atomic layer deposited binary and ternary oxide thin films
N. Aslam (2017), X, 172 pp
ISBN: 978-3-95806-274-0

Band / Volume 53
Operando X-ray photoemission electron microscopy (XPEEM) investigations of resistive switching metal-insulator-metal devices
C. J. Schmitz (2017), IX, 153 pp
ISBN: 978-3-95806-283-2

Band / Volume 54
Optimization of powder and ceramic processing, electrical characterization and defect chemistry in the system $Yb_xCa_{1-x}MnO_3$
M. Rahmani (2018), XIV, 164 pp
ISBN: 978-3-95806-323-5

Band / Volume 55
Organic-Metal Hybrid Interfaces at the Mesoscopic Scale
G. Zamborlini (2018), xi, 133 pp
ISBN: 978-3-95806-328-0

Band / Volume 56
Configurable frequency synthesizer for large scale physics experiments
N. Parkalian (2019), xxi, 114 pp
ISBN: 978-3-95806-393-8

Band / Volume 57
Resistive switching phenomena in stacks of binary transition metal oxides grown by atomic layer deposition
H. Zhang (2019), ix, 196 pp
ISBN: 978-3-95806-399-0

Band / Volume 58
Element-Selective Investigation of Femtosecond Spin Dynamics in Ni_xPd_{1-x} Magnetic Alloys using Extreme Ultraviolet Radiation
S. Gang (2019), 93, xx pp
ISBN: 978-3-95806-411-9

Band / Volume 59
Defect engineering in oxide thin films
F. V. E. Hensling (2019), 10, 164 pp
ISBN: 978-3-95806-424-9

Band / Volume 60
Chemical control of the electrical surface properties of *n*-doped transition metal oxides
M. Andrä (2019), X, 150, XXXVIII pp
ISBN: 978-3-95806-448-5

Band / Volume 61
Digital Signal Processing and Mixed Signal Control of Receiver Circuitry for Large-Scale Particle Detectors
P. Muralidharan (2020), xv, 109 pp
ISBN: 978-3-95806-489-8

Band / Volume 62
Development of Electromagnetic Induction Measurement and Inversion Methods for Soil Electrical Conductivity Investigations
X. Tan (2020), ix, 124 pp
ISBN: 978-3-95806-490-4

Weitere ***Schriften des Verlags im Forschungszentrum Jülich*** unter
http://wwwzb1.fz-juelich.de/verlagextern1/index.asp

Information
Band / Volume 62
ISBN 978-3-95806-490-4

Mitglied der Helmholtz-Gemeinschaft

JÜLICH
Forschungszentrum